2006

Health Monitoring of LAV Planet Gear Bushings using Signature Analysis Techniques

Victoria L. Parnell

Health Monitoring of LAV Planet Gear Bushings using Signature Analysis Techniques

By

Victoria L. Parnell

A Thesis Submitted
In Partial Fulfillment
Of the Requirements for a

MASTER OF SCIENCE
IN
MECHANICAL ENGINEERING

Approved by:

Dr. Mark H. Kempski
Department of Mechanical Engineering

Dr. Kevin B. Kochersberger
Department of Mechanical Engineering

Dr. Stephen Boedo
Department of Mechanical Engineering

Dr. Edward C. Hensel
Department Head of Mechanical Engineering

DEPARTMENT OF MECHANICAL ENGINEERING
ROCHESTER INSTITUTE OF TECHNOLOGY

March 2006

Permission Granted

Health Monitoring of LAV Planet Gear Bushings using Signature Analysis Techniques

I, Victoria Parnell, hereby grant permission to the Wallace Library of the Rochester Institute of Technology to reproduce my thesis in whole or in part. Any reproduction will not be for commercial use or profit.

Date:_____ Signature of Author: Victoria Parnell

Abstract

The Center for Integrated Manufacturing Studies (CIMS) is studying the improvement of military Light Armored Vehicles (LAVs) for the United States Department of Defense. A focus of this study is the Marine Corps LAVs that are experiencing failures in the planetary assembly which serves as the vehicle's final drive system. The primary failure source is the bushings that provide the interface between the planet gears and their respective pins.

Currently, to detect a bushing failure, vehicle occupants must exit the LAV and place their hand on the wheel hub cover to check for excessive heat. If the hub "feels too hot," travel must stop so the planetary assembly can cool down. These overheating wheel hubs can lead to catastrophic failure of the planetary assembly. Therefore, CIMS is working to analyze these bushing failures and develop a method that will allow occupants to detect potential bushing failures from inside the moving vehicle.

In the past, the relationship of pin-bushing interface temperature and wear showed that temperature does not indicate bushing failure soon enough for practical implementation. It was the intention of this current wear study to evaluate bushing failures using vibration signatures as part of an effort to develop failure prognostic tools for (future) in-service use.

This thesis was conducted as a feasibility assessment study to evaluate bushing failure from a vibration and signal processing standpoint. Accelerometers were used to collect vibration data from the bushings. Collected vibration signatures were analyzed and examined as bushing wear progressed to determine whether or not remaining bushing life could be predicted using vibration signatures.

Vibration data was analyzed from an energy standpoint; that is, the band power was calculated for several frequency bands of interest. Band power was plotted versus bushing wear to reveal any potential relationship between the two. Test results showed that a direct, linear relationship exists between bushing wear and band power in the 2000 to 2100 Hz frequency range.

The results of this thesis suggest that vibration data can be used to identify the severity bushing wear. Since this investigation was conducted as a feasibility assessment, additional work is required before this wear detection method can be implemented on an actual LAV. It is recommended that similar bushing wear-vibration studies be conducted where bushings are tested on the Mustang dynamometer (at CIMS) and then on an actual LAV.

Acknowledgements

First, I wish to thank my primary thesis advisor, Dr. Kempski. Without his help, this project would not have been completed. Dr. Kempski's suggestions, guidance, and patience throughout this process are much appreciated. Additionally, I would like to thank my "secondary" thesis advisor, Dr. Kochersberger. His background in vibration signature analysis was instrumental in the success of this thesis.

I would like to thank Nabil Nasr and the Center for Integrated Manufacturing Studies (CIMS) for funding this project. I appreciate the support I have received from the members of the Structures and Materials group at CIMS, especially Dr. Michael Haselkorn.

Most of all, I wish to thank my family and friends, especially: Cory who convinced me to pursue this degree, my parents for their unyielding support, guidance, and generosity, and mostly, my fiancé Jason, for his unconditional love, encouragement, and selflessness throughout this project as well as my college career.

Table of Contents

List of Figures

List of Tables

1.0 Introduction

The Center for Integrated Manufacturing Studies (CIMS) is a leading center for applied research in remanufacturing. A focus at CIMS is the modernization of large systems and equipment. One project in particular involves the improvement of military Light Armored Vehicles (LAVs) for the United States Department of Defense. Currently, the Marine Corps LAVs are experiencing failures in the planetary assembly which serves as the vehicle's final drive system. This system exists in each wheel hub and provides the high torque required to move the vehicle (see Section 2.0 for details). Power is transmitted from the transfer case, to four differentials, and finally to eight planetary assemblies [22]. Each planetary assembly consists of a sun gear that drives four planet gears, all of which is held together by an encompassing ring gear. The primary failure source is the bushing that provides the interface between the planet gears and their respective pins.

1.1 Problem Description

The military has been experiencing unexpected failures with the LAV-25. The source of these failures is a pin-gear interface bushing that exists inside the wheel hub of the vehicle. Currently, to detect a bushing failure vehicle occupants literally have to exit the LAV and place their hand on the wheel hub cover to check for excessive heat. If the hub "feels too hot," travel must stop to allow the planetary drive system time to cool down. Clearly this is not a safe maneuver to perform; and furthermore, the hubs will not be checked in the midst of battlefield operations. Neglecting these overheating wheel hubs can lead to catastrophic failure of the planetary assembly. Therefore, CIMS is working to analyze these bushing

failures and develop a method that will allow occupants to detect potential bushing failures from inside the moving vehicle.

In the past, the relationship of pin-bushing interface temperature and wear has been studied at CIMS (see Section 2.2.1 for temperature testing details) [23]. Unfortunately, experimentation conducted during this study showed that temperature does not indicate bushing failure soon enough for practical implementation [23]. It is the intention of this current wear study to evaluate bushing failures using vibration signatures as part of an effort to develop failure prognostic tools for (future) in-service use.

This thesis will be conducted as a feasibility assessment study. The planet gear bushing failures described above will be evaluated from a vibration and signal processing standpoint. Accelerometers will be placed on a test rig referred to as the 'bushing tester' to collect vibration data. First, typical signals from the bushing tester will be characterized via a series of baseline tests. The baseline testing will also include a preliminary comparison of vibration data from new bushings to that of worn bushings. Once the test apparatus has been characterized, planet gear bushings will be run from healthy condition to failure. Collected vibration signatures will be analyzed and examined for differences between a "healthy" bushing versus a "diseased" bushing to determine whether or not remaining bushing life can be predicted using vibration signatures. If it is found that remaining bushing life can be predicted from this data, vibration signal results will be compared to previous results obtained from monitoring pin-bushing interface temperature, and recommendations for future work will be made. Additionally, it should be kept in mind that a relatively simple data

analysis technique is desired to relate bushing wear and vibration signatures. This will simplify the future task of implementing real-time analysis on board the LAV and alleviate the need for an experienced analyst to interpret the results. Finally, it should be noted that this study is conducted as a first-generation analysis of bushing wear using vibration signatures. In the event that results from this study show a strong relationship between bushing wear and vibration signatures, it is not expected that the idea can be immediately implemented on the LAV-25. Instead, it is understood that a second- and perhaps third-generation series of testing will be necessary before this wear monitoring technique can be realized on any U.S. Marine Corps vehicle.

2.0 Background

2.1 Light Armored Vehicle - 25 (LAV-25)

The Family of Light Armored Vehicles (FOLAV) is a self-contained unit that provides a mobile combat system to the Marine Air-Ground Task Force (MAGTF). The FOLAV consists of seven LAV configurations and one intelligence system on an LAV chassis [22]. The vehicle of concern is the LAV-25, an all-terrain military vehicle that can be fully amphibious in three minutes or less (see Figure 1 for photograph) [21]. It is a $900,000 machine used by the U.S. Marine Corps to provide "strategic mobility to reach and engage the threat, tactical mobility for effective use of fire power, fire power to defeat soft and armored targets, and battlefield survivability to carry out combat missions" [21]. It is powered by a 275 hp diesel engine and is supported by eight wheels with independent suspension [21]. The vehicle is in full-time four-wheel drive (rear wheels) with the capability of eight-wheel drive [21]. Inside each wheel is a planetary assembly (Figure 2) that serves as the final speed reduction and transmits power to the wheels. The maximum speed of this vehicle is 62 mph [21].

When completely loaded for combat, the LAV-25 weighs 28,400 lb [32]. It is approximately 21 feet long, 8 feet wide, and 8 feet high [32]. It is capable of transporting three crewmembers and six troops [32].

Figure 1. Photograph of LAV-25

2.1.1. Planetary System

The planetary system exists in each wheel hub on the LAV-25 and acts as the final drive reduction. Input comes directly from a driveshaft that transmits power through the system. A carrier plate with four pins supports four planet gears that rotate around the sun gear. An outer, stationary ring gear supports the system. A photograph of the planetary system is shown below in Figure 2.

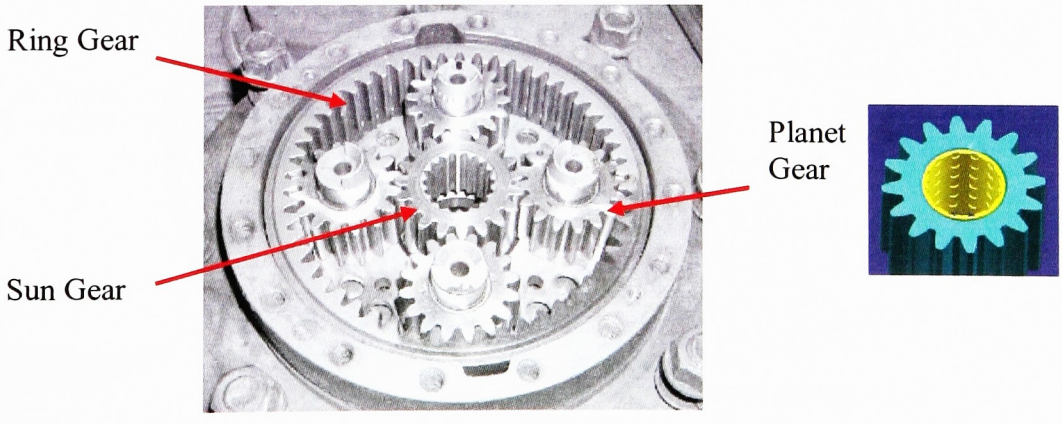

Figure 2. LAV Planetary Assembly (left), Planet Gear and Bushing (right)

A cover is bolted to the carrier plate to prevent particle contamination and so that the hub can be partially filled with gear oil for lubrication of the mechanical parts. Quaker State SAE 80W-90 high performance gear oil (MIL-L-2105) is used to lubricate the planetary assembly. The planet gears are splashed with oil as the wheel rotates. Additionally, ports are set up through the system such that oil is wicked into the pin-bushing interface via a centrifugal force that results from the wheel's rotational motion.

The sun gear fits over the spline of the driveshaft and therefore rotates as the driveshaft does. Torque from the driveshaft is transmitted to the four planet gears via the sun gear (Figure 3). This causes the planet gears to rotate and travel around the inside of the stationary ring gear along the red-dashed path in Figure 3. This motion of the planet gears forces the pins and therefore carrier plate to follow the same path. Since the carrier plate is connected directly to the wheel hub, the wheel rotates with the carrier plate.

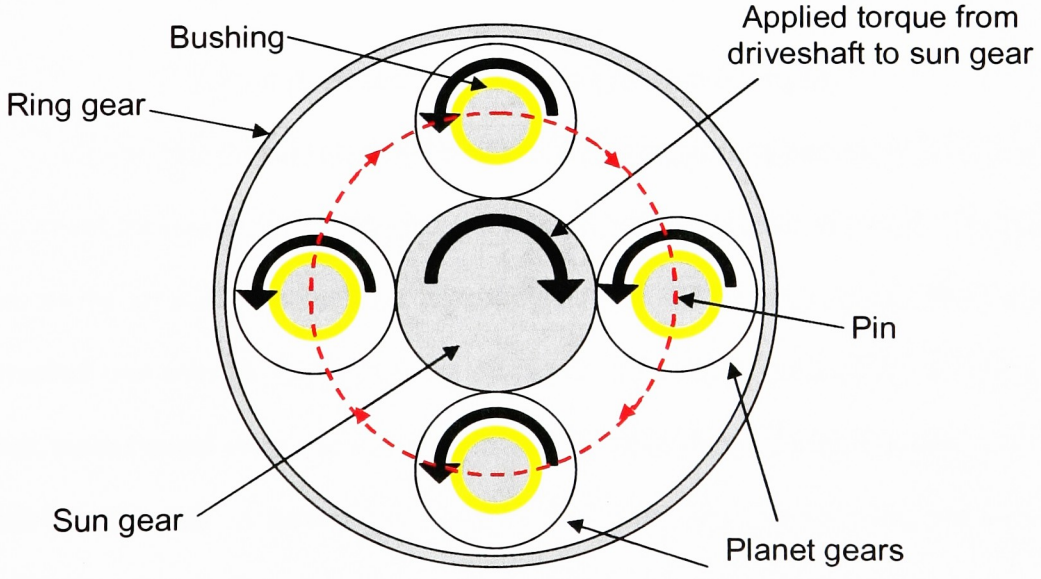

Figure 3. Planetary Assembly Operation Diagram [27]

Torque transmitted from the driveshaft ultimately creates a load on the planet gears (see Figure 4 for free body diagram). Each planet gear experiences three main forces: an input force from the sun gear (IF_S) and reaction forces from the ring gear (RF_R) and pin (RF_P). These forces cause the planet gear to travel around the inside of the ring gear as described above. Treating the planet gear and bushing as a single component, this motion introduces a frictional torque at the pin-bushing interface (FT_{P-B}).

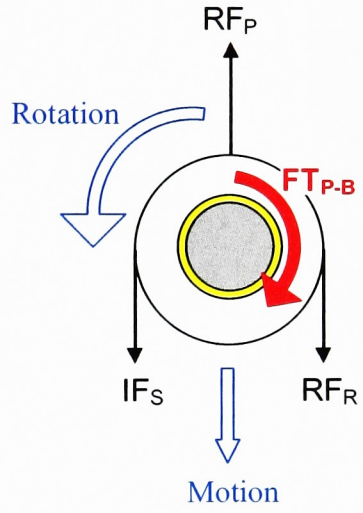

Figure 4. Free Body Diagram of Planet Gear [14]

The motion of the planet gears around the inside of the ring gear pushes the pins in a circular motion around the inside of the ring gear and therefore causes the wheel to roll. The bushing experiences the greatest reaction force from the pin (over 8,000 lb, see Appendix A) when the driveshaft transmits the largest amount of torque. This occurs during LAV acceleration. However, more typical loads that are experienced by the bushings during extended LAV use are much less than this. A spreadsheet of LAV road speeds and corresponding pin forces is shown in Appendix A. This sheet was compiled by engineers at CIMS and was used to determine appropriate speeds and loads for experimental testing. Details are discussed in Section 4.1.

2.1.1.1 Garlock DX Bushings. As previously mentioned, the focus of this thesis is the Garlock DX bushings that serve as the interface between the LAV wheel hub planet gears and their respective pins. These bushings are constructed of three layers: a polymer lining, a bronze sinter layer, and a steel backing (see Figure 5 below) [13]. More specifically, the polymer lining is acetal copolymer, a PTFE (polytetrafluoroethylene) based material. The main problem investigated in this study is the wear of the acetal lining during operation.

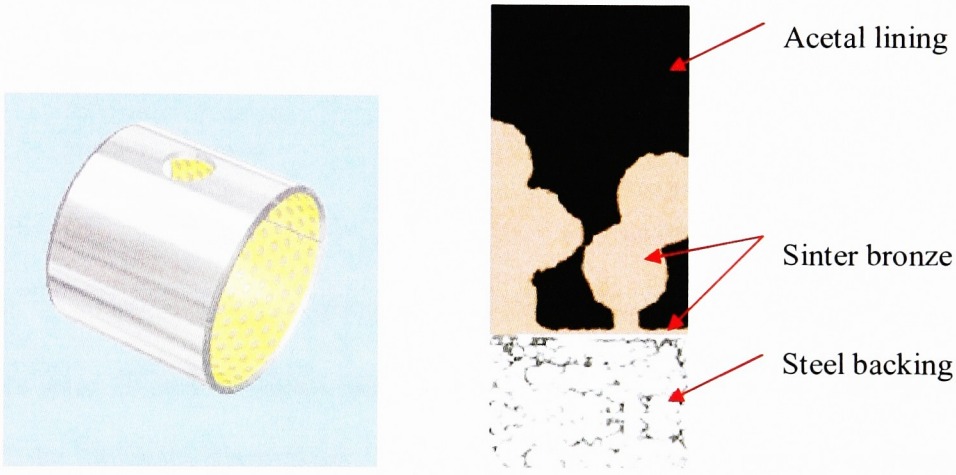

Figure 5. Garlock DX Bushing and Microsetion [13]

An interesting feature of the DX bushings is a uniform pattern of depressions in the acetal lining. These pits serve as miniature lubrication reservoirs [13]. The bearings perform best when lubricated with grease and, although not highly recommended, they can even operate in the absence of lubrication [13]. In this particular application, SAE 80W-90 high performance gear oil is used as the lubricating agent, which is an acceptable alternative to grease [13]. The bushings are intended for high load and low speed applications [13]. Important to note is the specified operating temperature, which ranges from -40°C to 130°C (-40°F to 266°F). In this study tests will be maintained at 250°F. The desired shaft surface finish (less than or equal to 0.4 micrometers) was also noted so that appropriate shafts could

be machined for testing [13]. Table 1 below contains additional details regarding DX bushing properties.

Bearing Properties	Unit	Value
Grease lubrication		
Maximum sliding speed U	m/s	2,5
Maximum PU factor	N/mm² * m/s = W/mm²	2,8
Coefficient of friction f	–	0,06 – 0,12
General		
Maximum temperature Tmax	°C	+130
Minimum temperature Tmin	°C	-40
Maximum load P static	N/mm²	140
Maximum load P dynamic	N/mm²	70
Shaft surface finish Ra	µm	≤0,4
Shaft hardness	HB	> 200
Shaft hardness for longer service life	HB	> 350

Table 1. Garlock DX Bushing Properties [13]

The bushings are press-fit into the planet gears such that the acetal is in contact with the pin (see Appendix L for clearance discussion). After exposure to certain operating conditions, the acetal lining of the planet gear bushings begins to degrade and wear, as shown in Figures 6a and 6b. This wear results in metal-to-metal contact (pin surface to bronze layer of bushing), which increases the amount of friction and generates heat. The additional heat results in secondary failures within the planetary system affecting components such as seals, sleeve bushings, and bearings.

Figure 6a. New (Unwrapped) Bushing

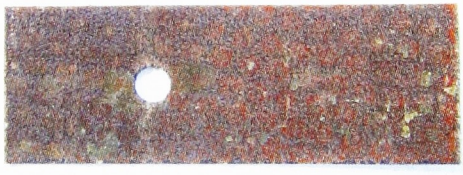

Figure 6b. Worn (Unwrapped) Bushing

2.2 Previous Testing

Prior to this study, CIMS has undergone extensive testing with DX bushings to gain an increased understanding of their wear characteristics [23]. For example, temperature has been examined with regard to its relation to wear. Also, the performance of alternative bushing materials and bushing lubricants has been tested.

2.2.1 Temperature Testing

To evaluate the correlation between temperature and bushing wear, several tests were conducted in which the DX bushings were worn to failure [23]. This was done using two pieces of equipment. The first, referred to as the bushing tester (BT), was custom developed at CIMS to test one bushing at a time. This test rig uses a motor to rotate a pin inside of the bushing that is under a direct radial load. A thermocouple mounted at the pin-bushing interface serves as the temperature indicator. The details of this test rig are discussed in Section 4.0. The second machine used to examine bushing wear is a 300 hp Mustang dynamometer. The dynamometer has the capacity to operate two planetary assemblies simultaneously, for a total of eight bushings. Here, thermocouples are routed through the vent lines of the planetary assemblies to collect temperature data. The dynamometer is a great real-world test bench since it uses the actual planetary assemblies from the LAV-25. Clearly, the dynamometer and BT have different loading and rotational methods. However, these differences were examined mathematically to allow CIMS staff to correlate the loads and wear times of data from either test rig [27, 28]. Results from both the BT and the dynamometer showed that an increase in operating temperature is indicative of wear. Figures 7a, 7b, and 8 show representative temperature and wear data from a typical BT test [29].

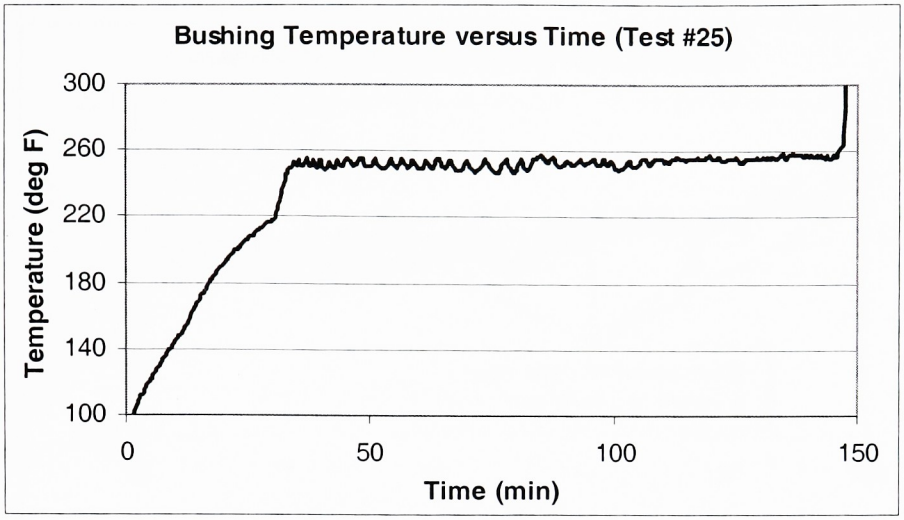

Figure 7a. Bushing Temperature versus Time [29]

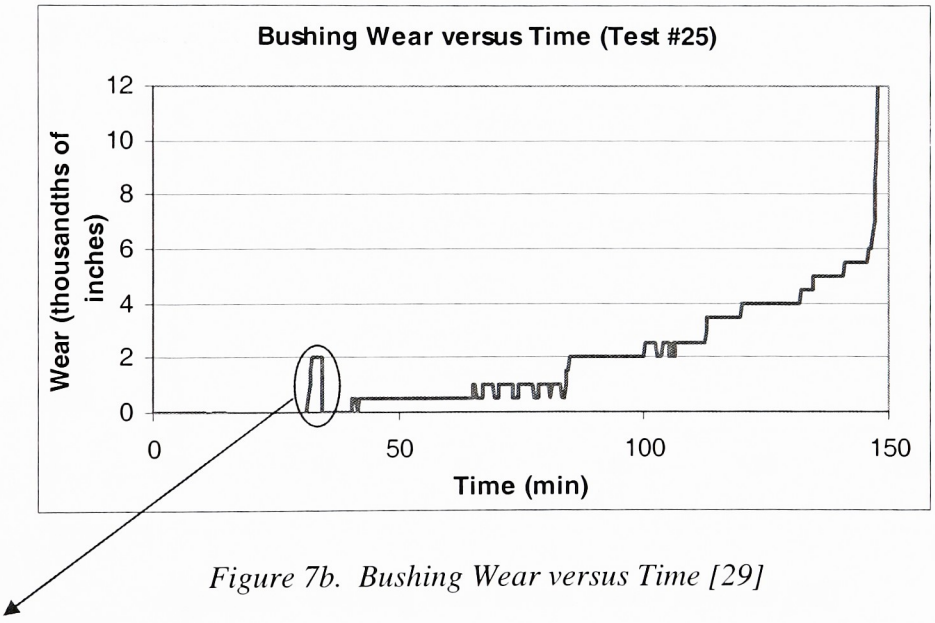

Figure 7b. Bushing Wear versus Time [29]

Note: At approximately 30 minutes, the load is increased from the break-in value (50 lb) to the full value (1000 lb) which results in a false wear reading. The digital indicator is re-zeroed after the full load is applied.

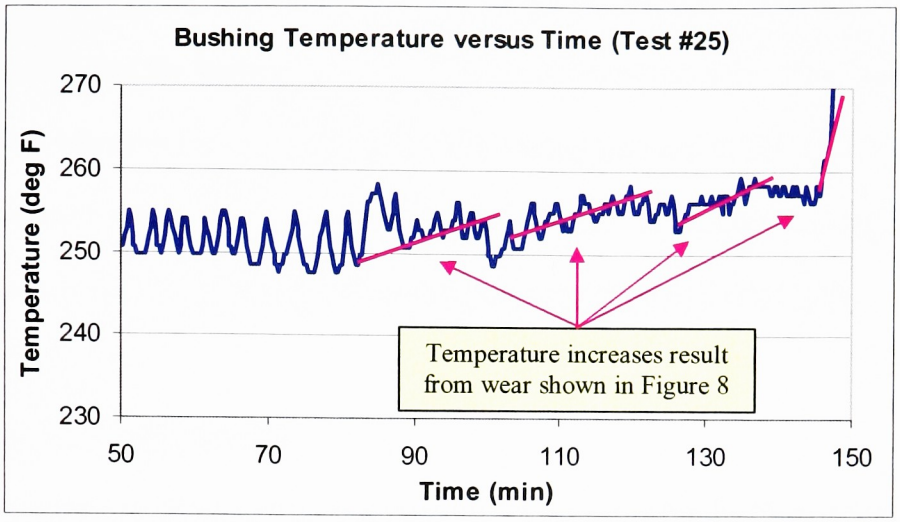

Figure 8a. Bushing Temperature versus Time – Zoomed [29]

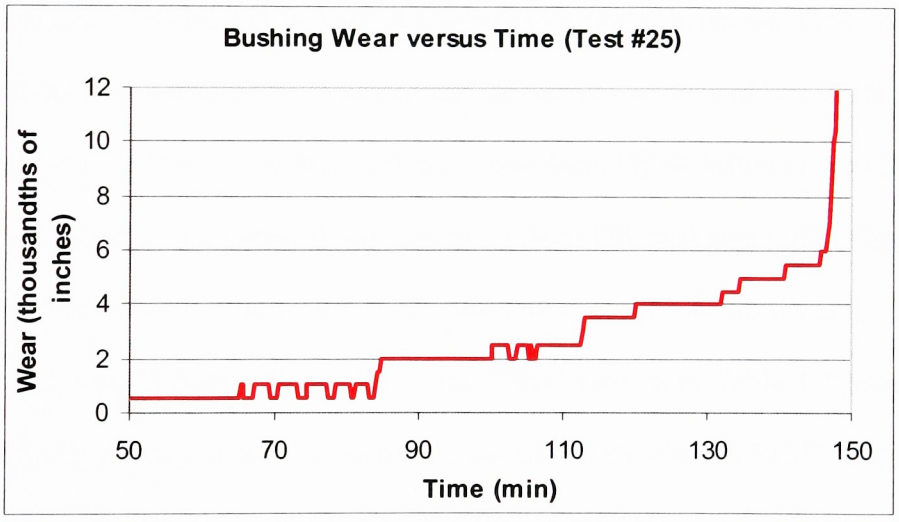

Figure 8b. Bushing Wear versus Time - Zoomed [29]

As shown in Figures 7a and 7b, a temperature increase (approximately 5°F) is observed between roughly 80 and 100 minutes that resulted from the wear between approximately 65 and 85 minutes. Several other temperature increases that result from bushing wear are highlighted in Figure 7a. Finally, a sharp temperature increase is shown as the wear jumps from 0.006'' to 0.012'' just before the test is shut down. Unfortunately, these slight

temperature increases are difficult to detect and tend to manifest themselves too late in the wear process, such that the bushing is well beyond the point of recovery. Therefore, it was conjectured that vibration signatures might be used to diagnose and indicate bushing wear at times earlier in the bushing life cycle. Showing that vibration signatures may indicate wear at an earlier stage than bushing temperature data is the major goal of this thesis.

2.2.2 Alternate Bushing Material

James Hildek examined alternate bushing materials in his study for the Center for Integrated Manufacturing Studies [14]. Here, Hildek used the BT to test several custom bushings fabricated from polyetheretherketone (PEEK) at various load and temperature scenarios and compared these results to those from typical Garlock DX Acetal bushings [14]. A cut-off time of 5000 minutes was chosen as "eternal life" so that the study could be finished in a timely manner [14]. Hildek found that bushings made from PEEK lasted at least four times longer than the typical acetal lining of the current Garlock DX bushings [14]. This is evidenced in Table 2 below, where each PEEK test lasted over 83 hours while the longest Acetal test lasted only 21 hours. (Note that in the "Test" column of Table 2, "Acetal" refers to the Garlock DX bushings that are currently in use on LAVs while "PEEK" refers to the custom made PEEK bushings. Additionally, the "I" and "II" designations refer to Scenarios I and II, respectively. In Hildek's study, Scenario I consisted of high load (1000lb) and low speed (540 RPM) while Scenario II consisted of low load (500 lb) and high speed (1716 RPM). Finally, "A," "B," and "C" refer to different test trials within the same Scenario).

Test	Shutoff Time (hrs.)	Shutoff Time (min)	Avg. Gear Temp (F)
Acetal IA	21.393	1283.567	262.192
Acetal IB	5.792	347.533	270.226
Acetal IC	13.754	825.267	263.603
Acetal IIA	7.030	421.783	255.316
Acetal IIB	6.817	409.017	262.496
Acetal IIC	2.617	157.017	268.113
PEEK IA	83.838	5030.267	252.258
PEEK IB	83.371	5002.267	259.774
PEEK IC	83.838	5030.250	254.387
PEEK IIA	83.334	5000.017	271.737
PEEK IIB	84.338	5060.283	267.165
PEEK IIC	83.334	5000.033	265.149

Table 2. Length of Tests from Hildek's Work [14]

Unfortunately, the U.S. Marine Corps was not interested in making any material changes, only in predicting the wear of their current bushings. Since the examination of an alternate bushing material is beyond the scope of this project, details of Hildek's work will not be discussed further.

In addition to Hildek's alternative bushing study, CIMS evaluated two different bushing types that Garlock produced. Garlock HX bushings were tested; their design is similar to the Garlock DX bushings, with the exception of the inner layer. HX bushings have an inner layer (with dimples) that is comprised of PEEK and PTFE with added "fillers" [13]. The HX bushings were tested since they have good wear resistance and can withstand higher temperatures (250°C+) [13]. Garlock DP4 bushings were also tested. They have the same steel backing and bronze sinter layer as the DX and HX bushings do, but the plastic lining is not the same. It is a smooth (no dimples) layer comprised of PTFE, CaF_2, and added "fillers" [13]. This bushing was selected for trial since it is stated as having "excellent lubricated wear resistance" [13]. "Load step-up" tests were conducted [7, 10] where a Garlock bushing was examined in the BT at various loads. The load applied to the bushing started at 200lb

and was ramped up to 1000lb at 200lb increments. At each load increment, the test was allowed to reach a steady-state temperature before the next load was applied. Four "load step-up" tests were conducted for each bushing type (twelve tests total). The steady state temperature at each load increment was averaged for all four tests and plotted versus load (Figure 9). Results showed that at a particular load, BT tests with DP4 bushings had a higher operating temperature than those with DX bushings.

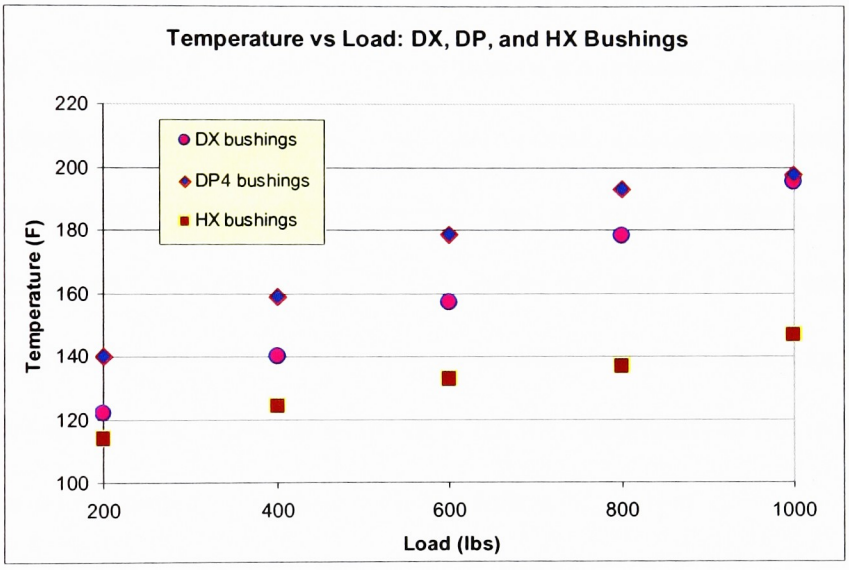

Figure 9. Effect of Bushing Type (DX, DP4, and HX) on Temperature [10]

Since the DP4 bushings resulted in a higher operating temperature, switching from DX to DP4 bushings was not considered a viable option. The HX bushings, however, had a lower operating temperature (at a particular load) compared to the DX bushings. Previous DX bushing temperature testing at CIMS [23] showed that lower operating temperatures reduced the rate of bushing wear and therefore increased bushing life. Unfortunately, USMC procurement constraints prevent changing to the HX bushing. Therefore, CIMS did not continue the research by completing run-to-failure tests on the HX bushings. CIMS did,

however, test HX, DX, and DP4 bushings at 1000 lb with no added heat for 5000 minutes (3.47 days) [10]. Test details are shown in Table 3.

Bushing Type	Oil Type	Test length (minutes)	Average temp (°F)	Bushing wear (inches)
HX	petroleum	5000	136	0.0000
	synthetic	5000	142	0.0005
DX	petroleum	5000	165	0.0010
	synthetic	5000	196	0.0005
DP	petroleum	5000	242	0.0005
	synthetic	5000	182	0.0000

Table 3. 5000 Minute Tests Comparing Oil Type and Bushing Type [10]

The data in Table 3 suggests that bushing type influences temperature. As shown, the HX, DX, and DP bushings resulted in relatively low, intermediate, and high operating temperatures, respectively. Bushing type, however, does not appear to have a strong influence on the amount of bushing wear as evidenced by the data in Table 3 which shows that wear of the HX, DX, and DP bushings was within 0.0010 inches. This data, however, could be misleading since the bushings were not given the opportunity to run to failure. The effect of oil type on bushing life is discussed in the following section.

2.2.3 Alternate Lubricant

A synthetic lubricant (75W-90 Mobil 1 Synthetic Gear Lubricant) was examined and compared to the typical petroleum lubricant to determine which lubricant resulted in the lowest operating temperature [8, 10]. Similar to the alternate bushing testing, four "load step-up" tests were conducted for both synthetic and petroleum oil (eight tests total). The steady state temperature at each load increment was averaged for all four tests and plotted versus load (Figure 10).

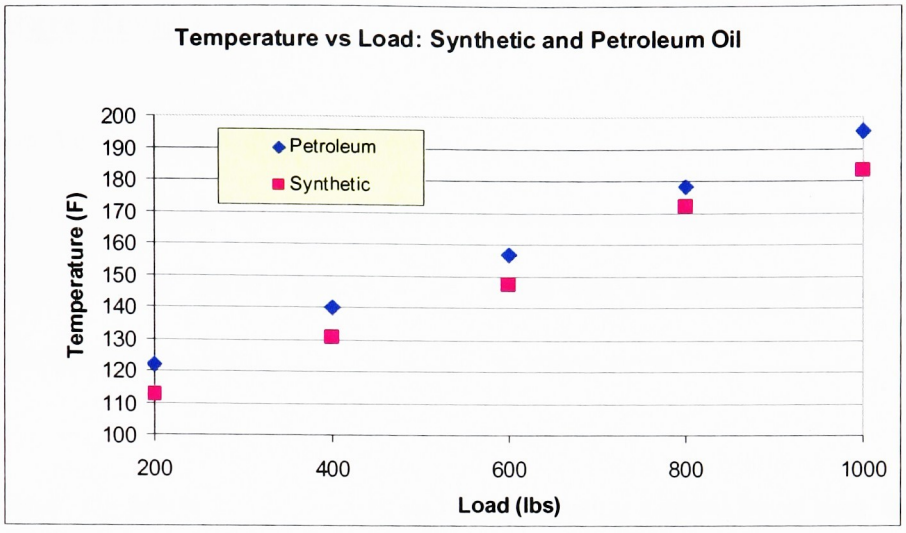

Figure 10. Effect of Lubrication Type on Temperature [10]

Results showed that at a particular load, BT tests with synthetic oil had a slightly lower operating temperature than those with petroleum oil (Figure 10). However, the difference was not substantial enough to warrant additional testing. Here, the USMC makes it a priority to keep the number of different maintenance supplies to a minimum, thereby reducing the number of items that are brought along on a mission and simplifying supply storage. The current petroleum oil is used as a lubricant for several other gearboxes on the FOLAV as well as on other USMC vehicles; therefore, changing the petroleum lubricant to synthetic oil would create an additional item to stock. Again, procurement constraints prevented the USMC from replacing the petroleum oil with synthetic oil. Therefore, CIMS did not pursue bushing wear tests using synthetic oil. However, CIMS conducted the same 5000 minute, 1000 lb tests to compare synthetic and petroleum oil as they did to compare DX and HX bushings (Table 3) [10]. The results suggest that oil type and bushing type do not have a substantial impact on the amount of bushing wear. Furthermore, the data implies that oil type does not have a consistent effect on operating temperature.

3.0 Literature Review

3.1 Vibration Analysis Techniques Overview

Vibration signature analysis is commonly used to monitor and diagnose the wear of mechanical components. Several studies based on this idea are introduced here, and their results are discussed and compared in the following subsections.

F. K. Choy *et al.* [5] predicted gear transmission faults using a spiral bevel gear fatigue test fixture at the NASA Lewis Research Center. The test was stopped several times to examine the gears for damage before the test was shut down due to a broken tooth. Vibration data was collected from an accelerometer mounted on the housing of the pinion shaft bearing, and data was analyzed using frequency analysis, time domain analysis, and joint time-frequency analysis (JTFA) [5]. In a follow-up study, Choy *et al.* [7] developed an analytical model to simulate the effects of surface pitting and wear on a gear tooth. This model was evaluated based on experimental results from the same test rig used in [5] and the test was conducted in the same manner as in [5]. Vibration data was analyzed using the Wigner-Ville Distribution (WVD) and frequency spectrum analysis techniques. A third study by Choy *et al.* [6] utilized the same test rig at the NASA Lewis Research Center to test gears from a rotor-craft gear transmission system. Here, the Wigner-Ville Distribution and wavelet transform joint-time-frequency analysis techniques were used to examine vibration signatures.

Peng and Kessissoglou [25] used wear debris and vibration data to examine the wear of a worm gearbox. (Wear debris results will not be discussed since it is beyond the scope of this thesis). A worm gearbox was operated under three different situations: "(a) lack of proper

lubrication, (b) normal operation, and (c) with the presence of contaminant particles added to the lubricating oil [25]." A resistive load was applied to the output shaft by forcing a paddle (attached to the shaft) through water [25]. Vibration data was collected from several locations including the drive-end of the motor and both ends of the worm gear shaft [25].

Cavacece and Introini [4] examined ball bearing damage using auto-power and cross-power spectrum analysis. The ball bearings are part of the transmission system from an EH101 helicopter [4]. Sensors were installed on a transmission box that connects the main transmission shaft to the tail rotor of the helicopter [4]. These sensors acquire acceleration data as the transmission box is tested on a gear fatigue test stand [4].

Liberatore and Carman [20] used vibration signatures to examine the structural 'damage' of a simply supported beam. A piezoelectric actuator excited the beam and a piezoelectric sensor monitored these excitations [20]. Structural 'damage' was simulated during experimentation by placing a four- and two-gram (2% and 1% of the structure's total mass, respectively) mass on the beam at different locations [20]. Data was analyzed using a Power Spectral Density (PSD) technique where the energy of narrow frequency bands is calculated.

3.1.1 Time-domain Analysis.

Choy *et al.* [5] employed a time synchronous averaging technique (to analyze gear wear) in which "the digitized time domain vibration signal is averaged over a large number of cycles, synchronous with the running speed of a particular machine element," [5]. The averaging technique used by Choy *et al.* reduces background noise so that defects can be realized using

statistical methods such as NA4* and NB4* (see Appendix B for explanation of these statistics) [5]. Unfortunately, this method is not always accurate when applied to damaged machinery due to shifting amplitude and frequency characteristics that are manifested in the time signal [5]. According to the authors [5], the NA4* and NB4* statistical analyses were successful at indicating pitting damage, although each statistic failed to clearly indicate tooth fracture. In Choy *et al.* [6], the raw time signal was one of three methods used to analyze the vibration data obtained from a rotorcraft gear transmission system. Here, the time signal showed a significant change in phase and amplitude as gear-tooth wear progressed. Finally, Peng and Kessissoglou [25] suggest that the time-domain can be useful in identifying rubbing wear in worm gears, which often manifests itself as a truncated wave in the time-domain.

Another interesting method of time-domain vibration signature analysis is Kurtosis. Typically, Kurtosis is used to assess whether or not a vibration signal indicates white noise [17]. However, metal-to-metal contact of mechanical components tends to generate vibration signatures with high Kurtosis [17]. Kacprzynski [17] employed this idea to identify defects in a CV joint using the time-domain vibration signature.

3.1.2 Frequency-domain Analysis.

In [5] the discrete Fast Fourier Transform (FFT) is applied to a synchronous averaged data set to obtain a frequency spectrum. The FFT technique is useful in "identifying vibrations due to various mechanical elements in the system at their operating frequencies," [5]. The amplitude spectrum can also be useful for identifying uncharacteristic signals of the system

that may result from wear or gear faults [5]. The FFT technique is not intended for complex systems since increased quantity of spectral lines can make it difficult to observe spectrum changes [5]. Additionally, Choy *et al.* [5] add that it can be difficult to detect faults such as fatigue cracks early in a life-test as these defects typically manifest themselves in low amplitude, broad frequency sidebands that are often masked by background noise. In another study by Choy *et al.* [7] that tested gear wear using vibration signatures, the authors mention that frequency analysis exhibits gear wear via an increase in sideband frequency amplitude. Frequency analysis results, however, did not provide enough information to determine the exact time location at which specific frequency components occurred (based on 360° revolution of the pinion); WVD analysis was necessary to obtain the time location information [7]. In a third study by Choy *et al.* [6], the frequency spectrum showed no notable difference in signal phase and amplitude as gear tooth wear progressed [6]. This was said to be due to the inherent spectral averaging characteristics [6]. Unfortunately, the exact method used by Choy *et al.* [6] to convert the data from the time domain to the frequency domain is not discussed. A form of frequency-domain analysis was also used in Cavacece and Introini [4]. Here, the authors employed auto-power and cross-power spectra to analyze the ball bearing damage of a helicopter transmission system. Maximum values of the auto-power spectrum are taken at 380 Hz (the ball bearings inner race frequency) and show an increase in amplitude as the test progresses (Figure 11) [4]. This increase in spectral amplitude is indicative of an increase in floor noise, which, in turn, signifies mechanical failure [4]. Similarly, maximum values of the cross-power spectrum show nonstationary behavior when plotted versus time (Figure 12), but the auto-power spectrum provides a clearer indication of failure according to these authors [4].

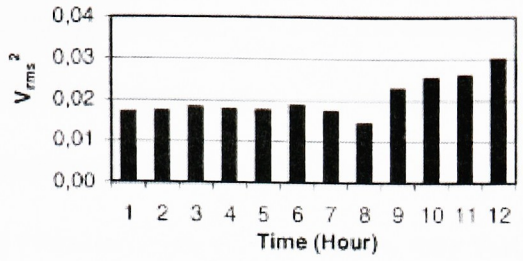

Figure 11. "Max Value of APS around 380 Hz" [4]

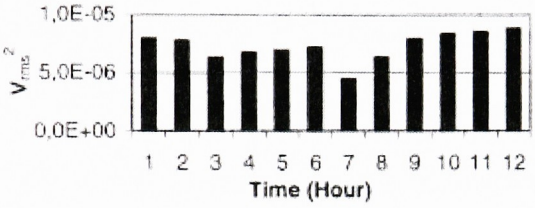

Figure 12. "Max Value of CPS around 380 Hz" [4]

Another work by Liberatore and Carman [20] utilized frequency-domain techniques to examine the structural damage of a simply supported beam using two piezoelectric devices. Here, data was analyzed via power spectral density and mode shapes where the energy of narrow bandwidths around resonant frequencies was calculated and monitored [20]. Comparing the energy of the undamaged structure to that of the damaged structure allowed for the creation of an index that was used to infer damage in the structure. The index, however, was limited in its ability to detect damage since it did not reveal the locale of the damage [20]. Instead, a damage location function was defined using structural mode shapes. (Since the location of the wear is known in the present bushing wear study, analysis via structural mode shapes is not needed). The authors [20] add that analysis via power spectral density appears to have increased sensitivity compared to strain energy analysis, natural frequency shifts, and mode shape analysis. For example, results produced by Liberatore and

Carman [20] show that the change in energy between the damaged and undamaged beam scenario was over 84% while the frequency shift between the two cases was only 1.6%. In another study, Peng and Kessissoglou [25] used vibration analysis to examine the wear of a worm gearbox. Regarding vibration analysis, the authors state that wear mechanisms such as sliding and rubbing of gears can manifest themselves through increasing vibration amplitudes and increasing energy content in a narrow-band frequency region [25]. Gear wear can also be indicated by an offset of the spectrum. Finally, the authors give a prediction of what to expect when examining the vibration signatures of gears. First, gears tend to go through a break-in period that shows high vibration amplitudes for the first few hours of testing. Once the gears have broken-in, the signature amplitudes decrease. As wear progresses, frequency amplitudes increase and eventually sideband frequencies develop, indicating gear wear. Results of the worm gearbox testing showed that vibration signatures were successful in identifying gear wear [25].

3.1.3 Joint Time Frequency Analysis.

In Choy *et al.* [5], the Wigner-Ville Distribution (WVD) was used as one of three analysis techniques to examine transmission gear wear. The WVD is a joint time-frequency analysis technique that presents an instantaneous frequency spectrum [5]. As the object of interest rotates one revolution, the vibration signature will change. If the vibration is repeated each rotation, the frequency spectrum resulting from a Fourier Transform will be uniform [5]. However, the WVD has the capability of illustrating the frequency distribution around the instantaneous frequency [5]. Results of the gear failure testing indicated that the WVD

produced the most accurate indication of the severity and location of the pitting and gear tooth fracture. However, a vibration database is necessary to understand the WVD results.

The Wigner-Ville Distrubution and wavelet transform joint-time-frequency analyses were used in a study by Choy *et al.* [6] that examined vibration signatures from damaged gear transmission systems. These authors concluded that the wavelet transform was a promising method of analysis since it resulted in a more direct quantification of gear tooth damage than did WVD [6]. In Choy *et al.* [7] where a transmission gear system is analyzed using vibration signatures, the authors conclude that the development of a signature analysis technique to examine the health of the gear system can best be achieved by utilizing both WVD and frequency analysis.

3.1.4 Vibration Analysis Technique Summary.

After examining the studies presented in Section 3.1 [4, 5, 6, 7, 20, 25], it is clear that several vibration data analysis techniques have been proven successful in identifying the wear of various mechanical components. For example, Choy *et al.* showed that gear wear in transmissions can be examined using vibration signatures analyzed via time-domain, frequency-domain, and JTFA techniques [5, 6, 7]. Additionally, Choy *et al.* [5] suggested that a combination of time averaging, frequency analysis, and joint time-frequency methods is the best choice for complete gear-train signature analysis. Liberatore and Carman [20] showed that PSD successfully indicates simulated beam wear while a study completed by Peng and Kessissoglou [25] suggests that narrow frequency bands and frequency-domain shifts can be used to indicate wear of a worm gearbox. Finally, auto-power spectrum

analysis was successfully employed by Cavacece and Introini [4] to diagnose bearing wear in a helicopter transmission system.

3.2 Technique Selected for Current Study

Due to the lack of published data examining bushing wear with vibration signatures, analysis techniques that are known to produce promising results from other mechanical wear applications will be applied in this study. Most notably, frequency-domain analysis techniques will be employed for the current thesis topic. Based on the review of case studies in Section 3.1, it is concluded that Fourier analysis will be used in this study. Yen and Lin [37] categorize vibration signals of faulted systems into two groups: "sustained defects and intermittent defects," and state that Fourier-based analysis is ideal for extracting narrowband signals from sustained defects. Recall Choy *et al.* [5] mentioned that this method is very useful in "identifying vibrations due to various mechanical elements." Additionally, Cavacece and Introini [4] showed that utilizing an auto-power spectrum illustrates the wear in ball bearings while Liberatore and Carman [20] indicated the wear of a simply supported beam using changes in frequency-domain amplitude. Finally, the work done by Peng and Kessissoglou [22] suggests that wear mechanisms such as sliding and rubbing of gears can manifest themselves through increasing vibration amplitudes and increasing energy content in a narrow band frequency region.

Although the Wigner–Ville Distribution technique produced promising results in some of the case studies [5, 6, 7], it was not chosen herein as a method for analysis due the need for a large vibration database to understand results. As previously mentioned, a simple bushing

wear monitoring process is desired as the outcome of the project. Finding a straightforward analysis technique to relate bushing wear and vibration signatures will simplify the future task of implementing real-time analysis on board the LAV and will also alleviate the need for an experienced analyst to interpret the results. Therefore, WVD analysis will only be utilized in the event that Fourier (frequency-domain) analysis is ineffective in identifying a relationship between bushing wear and vibration signatures of the system.

3.2.1 Fourier Analysis

Joseph Fourier stated that a sum of complex exponentials or sinusoids can be used to replicate a discrete periodic signal and a finite distribution of complex exponentials can be used to represent a nonperiodic discrete signal and a finite discrete signal [9]. A Fourier transform is the reproduction of a finite discrete signal using a finite distribution of complex exponentials [9]. The main advantage of such a transformation is that it allows for the identification of every frequency that exists within the (non-aliased) signal of interest [9]. The continuous Fourier Transform (FT) is defined as follows:

$$X(f) = \int_{-\infty}^{\infty} x(t) e^{-j2\pi ft}\, dt \qquad \text{Eq (1)}$$

where *x(t)* is a time-domain continuous signal [31]. When the Fourier transform is applied to a discrete function *x(n)* rather than a continuous function *x(t)*, the result is the Discrete Fourier Transform (DFT):

$$X(k) = \sum_{n=0}^{N-1} x(n) e^{\frac{-j2\pi kn}{N}} \qquad \text{Eq (2)}$$

It should be noted that frequencies resulting from a DFT (and FFT) will actually show up twice. This is because the input data becomes split into "positive" and "negative" frequency

complex components [9]. These data are often plotted in a manner that is symmetric about the Nyquist frequency (Figure 13 [33]).

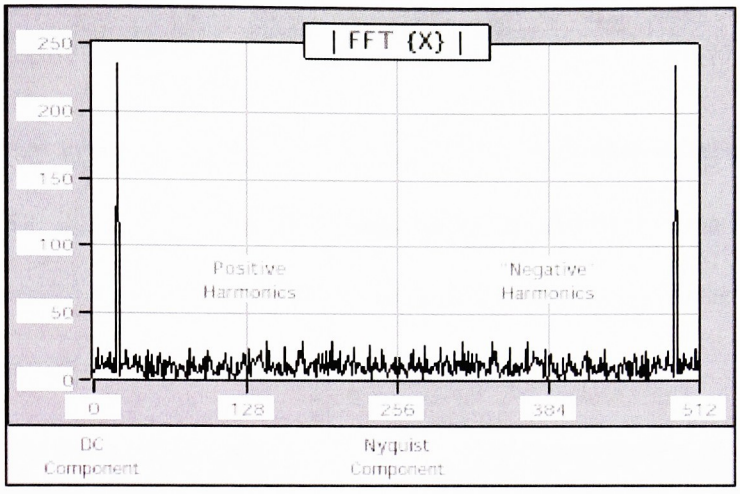

Figure 13. Positive and Negative Frequency Components Resulting from a FFT [33]

As illustrated in Figure 13 [33], the symmetrical components reflected about the Nyquist frequency are the resulting "positive" and "negative" frequency components from a FFT.

As shown in the Eq (2) above, the DFT of a function requires N^2 multiplications to calculate the N values for k. To reduce the number of calculations, the Fast Fourier Transform (FFT) was developed as an efficient method for computing the DFT [9]. This algorithm speeds the DFT calculation by reducing the number of multiplications from N^2 to $\frac{N(\log_2 N)}{2}$ [9]. This is accomplished by using "decimation in time" where a transform of length N written as the sum of two transforms of length N/2 [9]:

$$X(k) = \sum_{n=0}^{\frac{N}{2}-1} x(2n) W_n^{2nk} + W_N^{k} \sum_{n=0}^{\frac{N}{2}-1} x(2n+1) W_n^{2nk} \text{ [9]}, \qquad \text{Eq (3)}$$

where $W \equiv e^{-2\pi i/N}$ and $n = 0, \ldots, N$ [9]. Notice that the original signal, *x(n)*, is split into its even and odd parts [9]. In this study, a LabVIEW Virtual Instrument titled *Auto Power*

Spectrum uses the FFT to compute the single-sided power spectrum of the input signal. First, the double-sided power spectrum is calculated as follows:

$$PowerSpectrum = \frac{FFT(A) \times FFT^*(A)}{N^2}, \qquad \text{Eq (4)}$$

where FFT*(A) is the complex conjugate of FFT(A) [26]. A double-sided power spectrum is shown in Figure 14a. To convert this into a single-sided spectrum (Figure 14b), the "negative" frequencies (right-hand group) are discarded while the "positive" frequencies (left-hand group), except for DC, are multiplied by two [26].

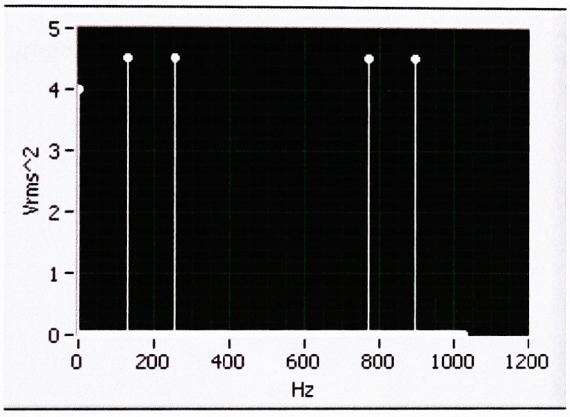

Figure 14a. Double-sided Power Spectrum [26]

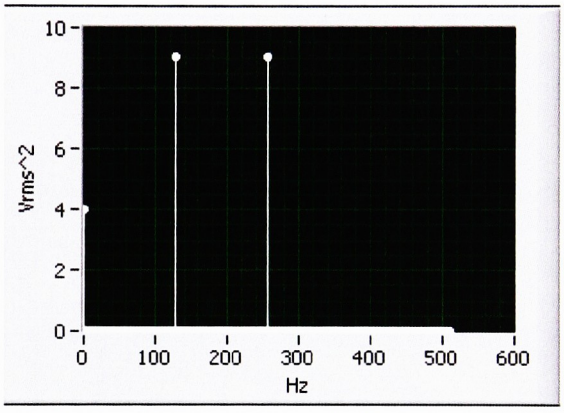

Figure 14b. Single-sided Power Spectrum [26]

Note that the amplitude of the frequencies in Figure 14b are twice that of those in Figure 14a. Also, Figure 14b stops at half the frequency (the Nyquist rate) that Figure 14a does. When computing a power spectrum (single-sided or double-sided), all phase information is lost because the magnitude of the FFT (or DFT) is squared [26]. Therefore, the use of power spectra is limited to applications where phase information is not necessary (calculating the power in a signal, for example) [26]. Additional details regarding the Auto Power Spectrum Virtual Instrument are discussed in Section 6.5.

3.3 Sampling Rate, Aliasing, and the Nyquist Frequency

The Nyquist Theorem states that two samples per waveform of the signal are required to accurately define a sinusoidal signal of interest [1]. According to the sampling theorem, the actual sampling frequency must be greater than the Nyquist sampling rate to accurately replicate the signal [9]. A simple temperature-monitoring example is provided in a document by Agilent Technologies [30]. Here, the temperature of a small part is cycling every second, and the temperature of that part is being logged every second. Therefore, each sample occurs at the same cycle location [30]. The result is collected data that appears as though the temperature never changes (Figure 15) [30].

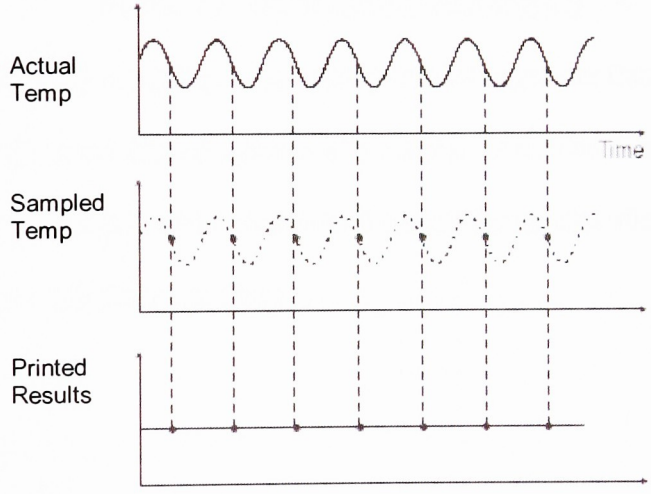

Figure 15. Temperature Data Logging Example [30]

The "aliasing" phenomenon shown in Figure 15 is a form of signal distortion that results from under sampling the signal [30]. Frequency components that are higher than half of the sampling frequency are reflected back over the Nyquist frequency; thus altering the signal [30]. Therefore, false images of the sampled signal are located at frequencies below the Nyquist Frequency [1]. This phenomenon is illustrated in Figure 16 below:

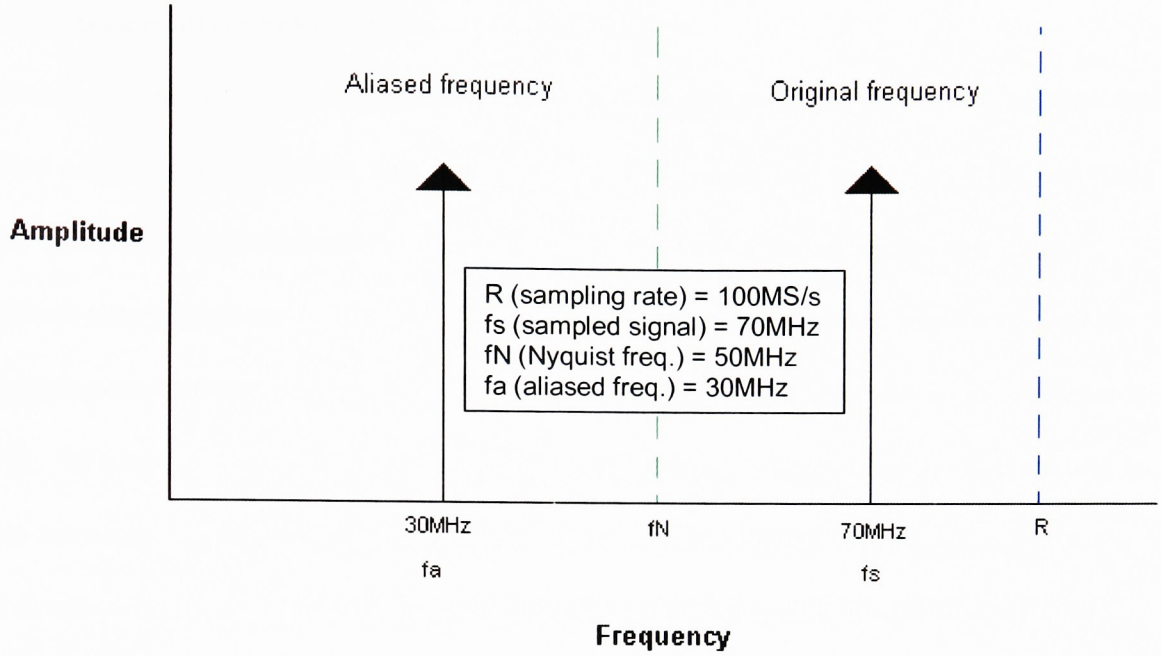

Figure 16. Illustration of Aliasing [1]

Aliasing can be avoided by sampling at an appropriate rate (greater than twice the Nyquist frequency) or by filtering out high frequency signals [1]. In this bushing wear study, data was sampled at an appropriate rate to eliminate the need for an anti-aliasing filter (see Section 6.3 for sample rate determination).

3.4 Accelerometers

Accelerometers sense motion and produce an electrical output proportional to the magnitude of the input. Piezoelectric accelerometers, which are the accelerometer type used in this study, operate based on a simple spring-mass principle. When a force or stress is applied to the accelerometer, quartz or ceramic crystals that are suspended in the accelerometer generate an electrical output. This charge is conditioned into a meaningful voltage that is proportional to acceleration.

3.4.1 Accelerometer Selection

Several different types of accelerometers are commercially available for various applications based on power requirements, robustness, performance range, and sensitivity. This diversity can, quite often, make selecting an appropriate accelerometer for an application more difficult than using one [12]. Frequency response, amplitude range and sensitivity, and the operating environment are the three main areas of concern when selecting an accelerometer [16]. As stated in [16], mounting methods and accelerometer accessories such as cabling are also important to consider as they can adversely affect the expected operating capabilities of an accelerometer. Ming Xu [36] adds that accelerometer size, weight, and cost are quite often primary concerns when choosing and accelerometer. Each of these ideas is discussed in detail in Appendix C.

3.4.2 Accelerometer Cabling

Connectors, cables, and cable terminations directly affect the performance of an accelerometer [16]. Coaxial cables, for example, can introduce erroneous signals through ground loops, electromagnetic interference, or radio frequency interference [16]. All cables should be rigidly fastened to prevent cable damage, sensor damage, and induced signal noise from vibrations [12].

3.4.3 Mass Loading

A system's vibratory signature is distorted when mass is added or removed from the structure [15]. Therefore, it is important to choose an accelerometer whose weight is correctly proportioned to that of the structure of interest [12, 15]. The general rule is that the ratio of

the structure's weight to the accelerometer's weight should not exceed 10:1 [35]. This guideline, however, refers to dynamic mass, and therefore should be used with caution [35].

4.0 Experimental Apparatus

4.1 Design

The experimental apparatus used for testing during this project is referred to as the bushing tester, or BT, and is owned and operated by CIMS. The bushing tester was developed after a need was established to conduct accelerated wear tests of the Garlock DX bushings. The BT expedites bushing wear by simulating the operation of a planet gear bushing in an LAV. Failing a bushing on the BT saves time and is much more economically efficient compared to failing a bushing via actual LAV operation or on the Mustang Dynamometer. Substantial monetary expenditures on items such as fuel, oil, labor, and vehicle maintenance are avoided through use of the BT. Photographs of the test rig are shown in Figures 17a and 17b below.

Figure 17a. Bushing Tester Apparatus, Photo 1

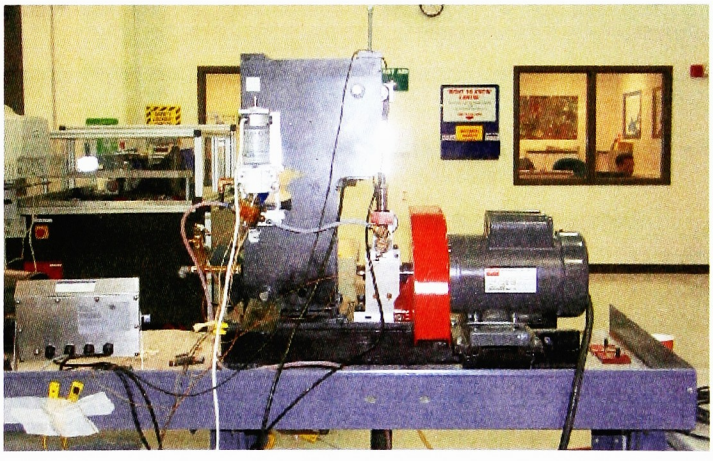

Figure 17b. Bushing Tester Apparatus, Photo 2

The BT is a custom bench-top machine that is controlled using LabVIEW software and National Instruments (Austin, TX) hardware. As shown in Figure 18, a stainless steel casing houses a rectangular block (refered to as the "bushing block") with a Garlock DX planet gear bushing press fit into a cylindrical hole that was machined into the block. A pin is inserted

through the bushing and supported by two radial ball bearings on either side of the housing (Figure 18 below). The bearings support the radial load that is applied to the bushing and allow for smooth pin rotation.

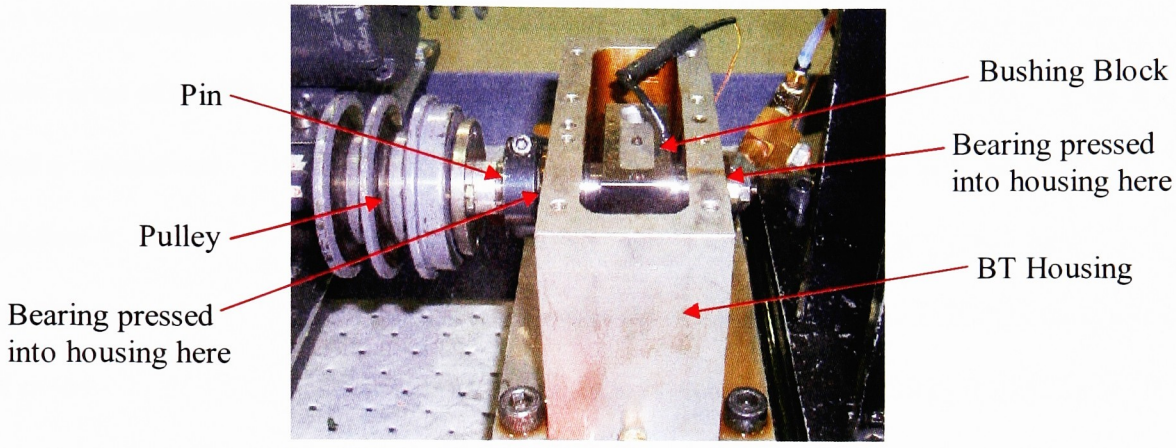

Figure 18. Bushing Block, Pin, and Housing Assembly

The rig operates via a two horsepower, single speed, AC motor used to drive the pin that rotates inside of the bushing. Pulleys and belts are used to provide the coupling between the pin and the motor output shaft. Three different arrangements of pulleys are available for low, medium, and high-speed operation. Testing for this study utilized only the high-speed arrangement. Previous bushing wear tests conducted at various speeds showed that reducing the pin speed only makes the test last longer [23], as might be expected. Changing speed has no other effect on bushing wear [23]; so it was deemed acceptable to only operate at one speed for this study.

A desired outcome of this bushing wear study is to compare the relationship between vibration signatures and bushing wear (gained from the current study) to the relationship between bushing temperature and bushing wear (previously obtained results at CIMS, [23]). In order to keep BT tests produced during this study consistent with BT tests conducted prior

to this study [23], typical speeds and loads that were used in the past will also be used in this study. When the BT was developed, various combinations of commercially available motors and pulleys were examined to find three arrangements that most closely corresponded to LAV road speeds of 17 mph, 35 mph, and 57 mph. These speeds were chosen to examine a wide range of speeds over three different LAV transmission gears so that a variety of speed-load combinations could be tested. To accelerate the wear process, most tests were conducted at a rotational speed equivalent to 57 mph. (All tests in this study will be conducted at 57 mph). A spreadsheet (Appendix A) was developed by CIMS staff engineers to correlate various LAV road speeds to the rotational speed of the planet gears and the load experienced by the pins (opposite of RF_P load in Figure 4), among other things. The spreadsheet evaluates the LAV as if it were operating in four-wheel drive instead of eight-wheel drive, which is only used occasionally. Using this spreadsheet, it was determined that the rotational speed of the planet gear bushings corresponding to a road speed of 57 mph is 1764 RPM. A single speed motor operating at 1725 RPM and two pulleys to connect the motor output shaft and pin was found to simulate the LAV operating at approximately 57 mph. This particular combination resulted in a pin rotational speed of 1750 RPM (slightly less than 57 mph). The spreadsheet (Appendix A) was also used determine the load that should be applied to the bushing. According to Appendix A, a load between 916lb and 959lb corresponds to a rotational speed of 1750 RPM. The load value was rounded up to the nearest 100 lbs (1000lb) by CIMS staff. Therefore, it is common practice at CIMS to operate the BT at 1750 RPM (HS) with a corresponding vertical load of 1000lb applied to the bushing. This speed-load combination is an approximation of the LAV operating at 57 mph. Although a closer approximation would have resulted from slightly decreasing the load, this

was not done in the current study as it would have created differences between the current thesis and previous CIMS test results [23].

4.1.1 Temperature Control

During typical testing, the oil is heated to increase the temperature of the system. This, in turn, decreases the length of time an individual run-to-failure test takes, thus making the process more efficient. The main heat source of the BT system is a hot plate. A secondary, less powerful heater is used to "boost" the oil temperature just before it enters the housing. For this study, the pin-bushing interface temperature will be held at 250°F. It should be noted that even though the system is heated, the temperature is always kept within the range of temperatures that are experienced during actual LAV operation.

Thermocouples are used to monitor temperature in two locations on the BT. This data provides feedback to the LabVIEW program for accurate control of the heating elements. Once the system has reached a steady state operating temperature, the temperature of a typical test will deviate less than 5°F from the mean, neglecting the typical temperature spikes that occur at bushing failure. One thermocouple is located in the oil stream just prior to entering the housing while the other is routed through a small hole in the bushing block and rests virtually at the pin-bushing interface (Figure 19). Data from the second thermocouple was used to develop temperature-wear correlation in previous bushing wear studies at CIMS [23] (see Section 2.2.1).

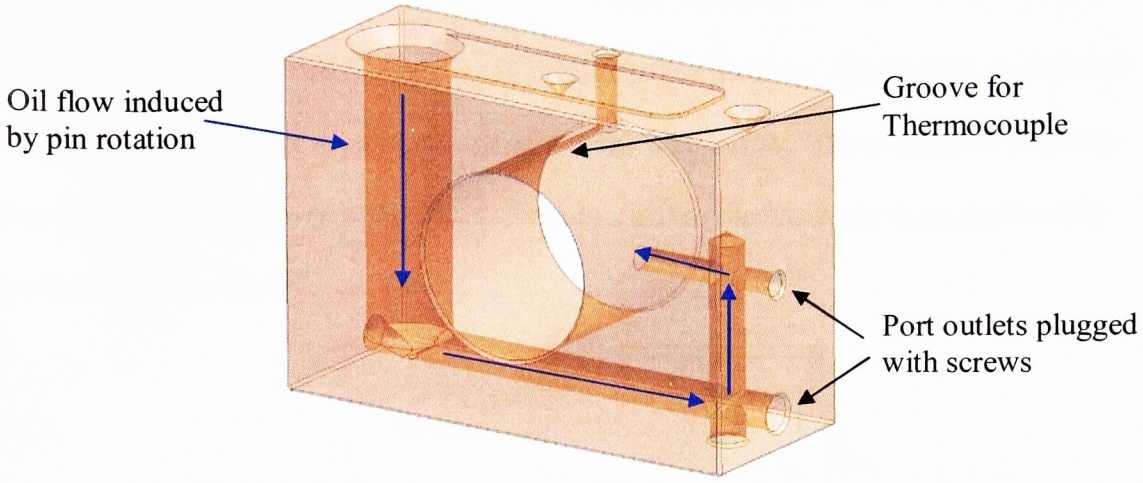

Figure 19. Bushing Block Model

4.1.2 Lubrication

The bushing-pin interface is lubricated with the same oil used in the actual LAV planetary assemblies, Quaker State SAE high performance 80W-90 gear oil. In the BT, oil flows through a closed system via a piston pump at 518 mL/min. It enters the housing and pours over the bushing block. Some of this oil travels through ports in the bushing block that lead to the pin-bushing interface (Figure 19). A hole exists in each bushing and during insertion, this hole is aligned with a corresponding oil port in the bushing block. Oil that is wicked through this port provides an oil film for the pin-bushing interface. Any residual oil in the housing drains back into the reservoir via a pipe at the bottom of the housing. This method of delivering oil to the pin-bushing interface was validated by years of testing at CIMS. In over 140 tests, the pin-bushing interface has consistently received adequate lubrication [23]. Furthermore, it was observed (during previous testing on the BT at CIMS) that when the pump was turned off, the height of oil in the main port through the top of the bushing block (Figure 19) slowly receded as oil was wicked into the pin-bushing interface [11].

4.1.3 Loading

A pneumatic load cell is used to apply a radial force to the bushing. The load is transmitted to the bushing via the lever system illustrated in Figure 20 below. The purpose of the lever system is to accommodate physical space contraints and to mechanically increase the load transmitted from the pneumatic cylinder.

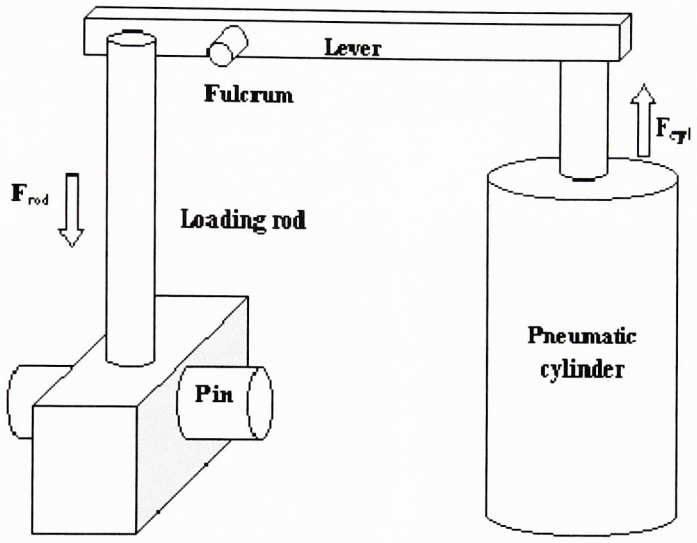

Figure 20. BT Loading Diagram [14]

As shown in Figure 20, the cylinder actuates upwards. This force is translated through the lever system into a downward radial load on the bushing. The horizontal lever arm is connected to the upright via a pivot connection. The upright interfaces with the loading rod via a 1- inch diameter bearing ball. The loading rod rests on a 3/16 - inch diameter ceramic bearing ball that is seated on the top of the bushing block. (Note that the oil feed comes in directly behind the loading rod so that loading does not interfere with oil flow). This bearing is centered in both the width and length of the bushing block, resulting in a point load applied to the top-center of the bushing block. The 1 - inch bearing at the interface of the loading rod and upright and the 3/16 - inch diameter ceramic ball bearing create a precise, vertical point load applied to the exact center of the bushing block. The vertical load applied to the

bushing block is held at 1000 lb during testing with the exception of a break-in period that occurs at the beginning of each test. The break-in period subjects the bushing to a 50 lb vertical load for ten minutes to allow the pin and bushing to "set" before applying the full load.

An anti-rotational feature is also included to prevent undesired motion of the bushing block. A second 3/16 - inch diameter ceramic bearing ball is seated in a dimple on the top of the busing block (see Figures 21a and 21b below).

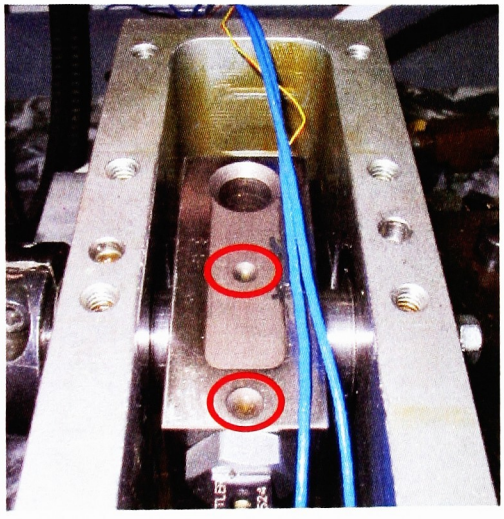

Figure 21a. Dimples in Bushing Block to Accommodate Ceramic Ball Bearings

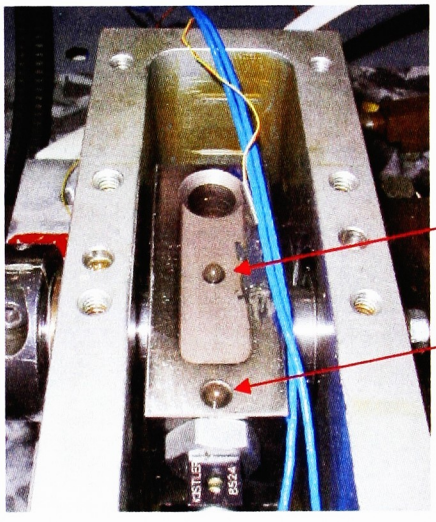

Figure 21b. Ceramic Ball Bearings in Place on Bushing Block

As illustrated, the bearing is centered in the width of the bushing block, but offset in the length of the bushing block. A screw mounted to the housing cover comes in direct contact with this ball bearing to prevent rotation of the bushing block.

4.1.4 Wear

The amount of bushing wear is measured directly using a digital indicator that is attached to the loading rod. The tip of the indicator rests on the (stationary) housing cover. As the bushing wears, the load arm moves downward relative to the housing. Therefore, a quantitative wear value is attainable. A 0.0120'' wear limit is set in the LabVIEW user interface.

4.2 Test Control and Data Acquisition

The graphical coding software LabVIEW (National Instruments, Austin, TX) is used to automatically control the BT system. Parameters such as temperature, load, operating time, operational limits, file name, and others are controlled with the user interface panel depicted below in Figure 22.

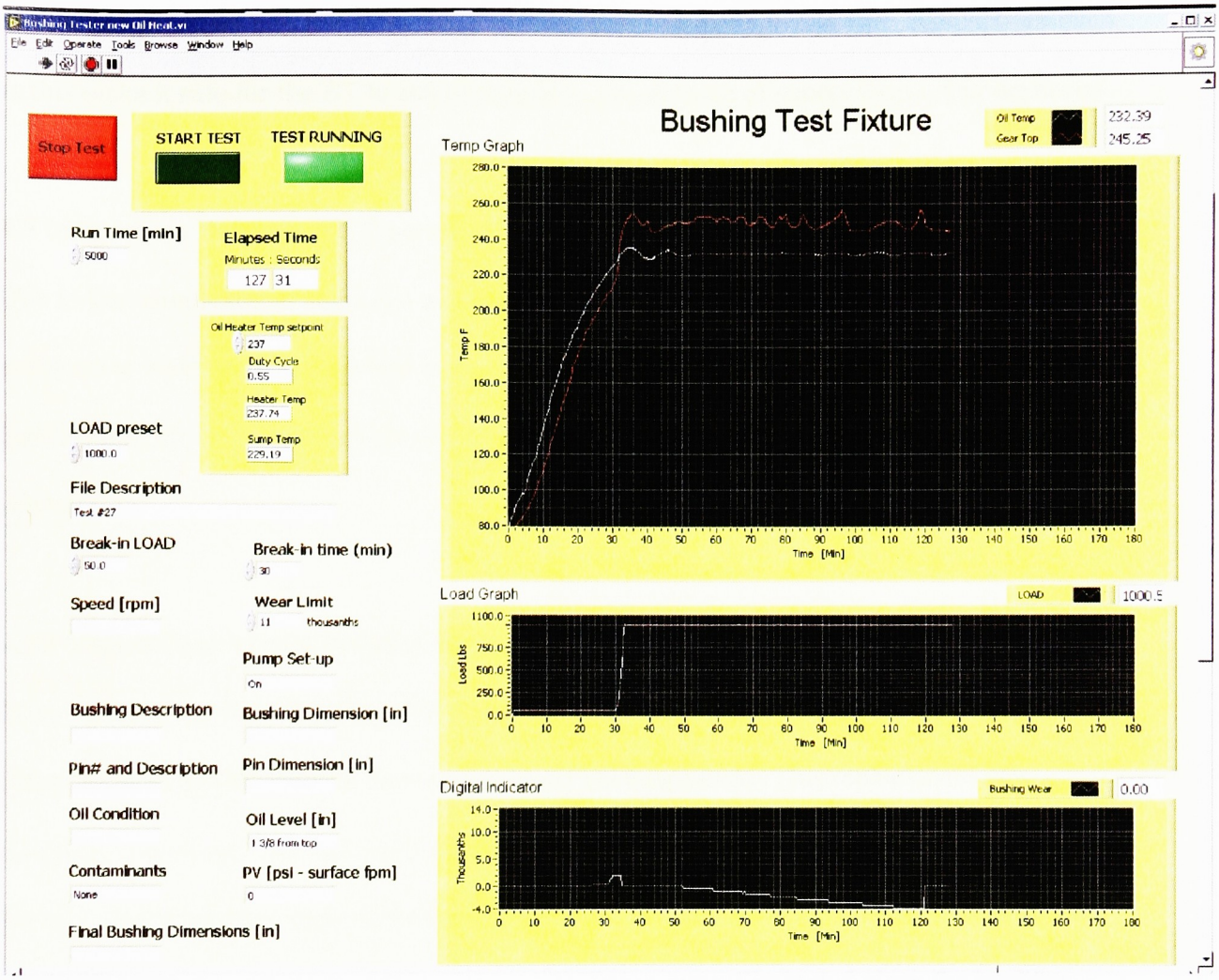

Figure 22. User Interface Panel for Data Acquisition Control

Feedback from the two thermocouples and vertical force from the load cell is used to maintain the system at steady operating conditions during a test. National Instruments data acquisition hardware (PCI-MIO-16E-1 DAQ PC Card) is used to interface with the sensors and software. Data from the thermocouples, load cell, and digital wear indicator is recorded for each test and automatically written to a text file. The LabVIEW program stops the test once the bushing wear limit has been reached. Additionally, several safety limits exist that will result in test shutdown if the limits are surpassed. For example, an over temperature

limit is programmed into the software to prevent machine damage and fire. Restrictions such as this make it safe for the BT to run overnight in the absence of supervision when necessary.

4.3 Differences Between BT Operation and Actual LAV Operation

Due to the complextiy of the LAV planetary assembly, reducing the system to a benchtop accelerated wear machine resulted in some discrepancies between actual and simulated bushing operation. These differences are explained and validated in the following subsections.

4.3.1 Planet Gear versus Bushing Block

Bushing tester rig modifications that occurred in late 2004 replaced the actual planet gear (then in use in the BT) with a custom-machined bushing block. This replacement was essential in ensuring that the load would be applied at the exact center of the bushing. Clearly, this presents a large difference between the actual LAV-25 planetary assembly and the BT simulated assembly. Differences in lubrication were eliminated since the bushing block was carefully designed and machined to "wick" the oil to the pin-bushing interface in a very similar manner as in the actual planetary assembly. Overall, replacing the planet gear with the bushing block was deemed acceptable since the current thesis is a "first-generation" study testing for *qualitative* results.

4.3.2 Planet Gear Rotation versus Pin Rotation

One major difference between the operation of the BT and that of an actual planetary assembly on an LAV is the rotating component. In a planetary assembly, the gear (and

therefore bushing) is rotating around the pin. The BT, however, was designed so that the pin is actually rotating inside of the bushing. This results in localized bushing wear due to the radial load. Figures 23a and 23b below show the difference in wear that results from an LAV-worn bushing and a BT-worn bushing.

Figure 23a. BT-worn Bushing

Figure 23b. LAV-worn Bushing

Creating an accelerated wear machine that rotated the bushing instead of the pin was beyond the scope of this project. The resulting data from the BT is deemed acceptable since this thesis study is conducted as a feasibility assessment rather than a final-phase project. The goal of this thesis is to determine whether or not it might be possible to predict bushing wear in planetary assemblies using vibration signatures. Furthermore, prior BT results were proven valid when BT wear results were successfully correlated to wear results from the dynamometer [27, 28]. The dynamometer tests two planetary assemblies, producing real-life results. Correlation studies at CIMS of the load style and resulting wear pattern between the dynamometer and BT proved that failed bushings on either machine could, in fact, be compared [27, 28].

4.3.3 Load Application

The actual load experienced by a planet gear when in operation is quite complex. As illustrated in Figure 4, the planet gears experience four different loads. It would be very difficult to replicate these loads exactly on the BT; therefore, the loading was simplified. A

single, vertical load is applied to the top of the bushing block during testing on the BT to replicate the reaction force of the pin on the bushing. This, in turn, generates the frictional torque shown in Figure 4. Therefore, the bushing block on the BT does not specifically experience the input force from the sun gear and reaction force from the ring gear. This, however, is considered acceptable for this study since the reaction force from the pin is the same and an accurate frictional torque is induced.

4.3.4 Pin Alteration

The pins used in the BT were machined by a local tooling company and are slightly modified from the pin dimensions used on the LAV. The pins used in the BT are longer than the actual LAV pins to allow room in the housing for the bushing block. The pins used in the BT also have a slightly smaller diameter than the LAV pins; the diameter is less than 0.0020'' smaller than the LAV pins. This is to accommodate the inner diameter of the radial ball bearings that support the pin. Reducing the pin diameter results in a larger pin-bushing clearance on the BT than in LAV operation. Even though this clearance difference would most likely change the vibration signature, the pin alterations are considered acceptable since this study is a feasibility assessment and qualitative rather than quantitative results are desired from this test rig.

4.3.5 Lubrication System

Each LAV wheel hub is filled half way with oil to lubricate the planetary assembly inside. During operation, oil is splashed over the gears as the wheel rotates. Additionally, a system of ports use the centrifugal force created by the spinning wheel to "pump" the oil through

holes in the pins. This lubricates the pin-bushing interface and provides an oil film at this location. Clearly, this intricate lubrication system could not be exactly replicated on the BT. As previously mentioned, oil poured over the bushing block simulates the oil splashed in the wheel hub while a system of ports in the bushing block is used to lubricate the pin-bushing interface. Although this is not exactly comparable to the lubrication system of the LAV, the bushing still receives adequate lubrication, and an oil film still exists between the pin and bushing (see Section 4.1.2). For these reasons, the BT lubrication system is considered an acceptable substitute for the LAV lubrication system.

4.4 Necessary BT Updates

To make the existing BT ready for testing applications specific to this project, a few adjustments were made. These included sensor additions and data acquisiston updates.

4.4.1 Instrumentation Updates

Two accelerometers were added to the machine. They were attached to the outside of the bushing block via a magnetic base as shown below in Figures 24a and 24b.

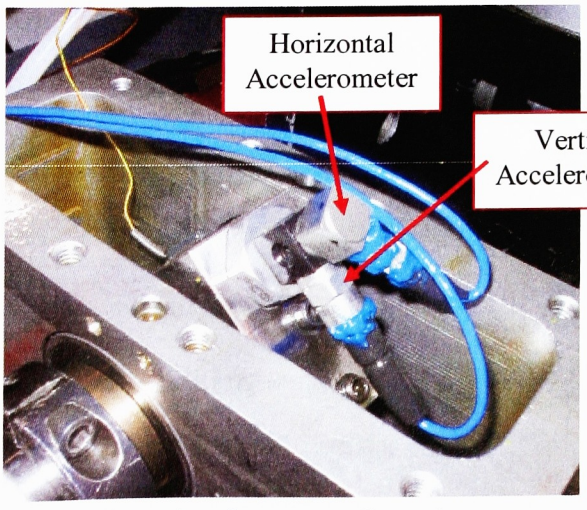

Figure 24a. Accelerometer Location on Bushing Block (block rotated)

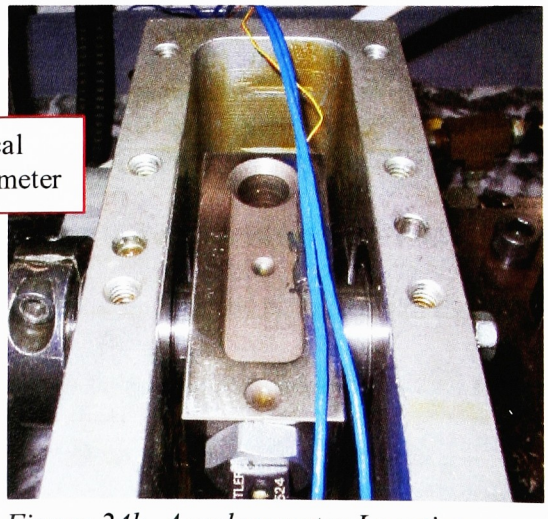

Figure 24b. Accelerometer Location on Bushing Block (as positioned during testing)

As illustrated, the accelerometers are located in the vertical and horizontal directions. (Note that the vertical and horizontal accelerometers are referred to as Accelerometer 1 and Accelerometer 2, respectively). Piezoelectronic accelerometers (Kistler Instrument Corporation, models 8774A50 and 8776A50M6) were chosen for this application. The selection process and accelerometer details are discussed in Section 6.1.1. A thin layer of SAE 80W-90 gear oil was applied underneath the magnet used to mount the accelerometers to the bushing block. As discussed in the literature review [16, 35], this oil film aids in signal transmission from the block to the accelerometers. Additionally, the accelerometer-cable connections were coated with RTV to prevent oil ingress. Coaxial cables were used for this application. They were carefully located in a rather inaccessible position in order to prevent any movement that might cause cable damage and/or induce signal noise as suggested in the literature review [12]. The cables were ported through an existing hole in the BT housing cover and plugged into an eight-channel signal conditioner (PCB Piezotronics, Inc. model 482A20). The signal conditioner is used to amplify the signal (x10) from each accelerometer so that signatures can be recognized by the software.

4.4.2 Test Control and Data Acquisition Updates

The test control and data acquisition system described in Section 4.3 required updating to account for the additional instrumentation. First, a method of collecting the vibration data was developed. It was decided that rather than tamper with the existing LabVIEW VI that is used to control the BT, it would be more efficient to set up another PC and write a separate program. Additionally, devoting one PC to vibration data collection would provide the necessary processing speed for the large data files that would result from the two

accelerometers sampled at 8 kHz. The developed program has a user interface where scan rate, buffer size, and time between sample collections can be controlled (Figure 25). National Instruments DAQ hardware (SCB-68 I/O Connector Block and PCI-MIO-16E-4 DAQ PC Card) is used to acquire the data from the signal conditioner output.

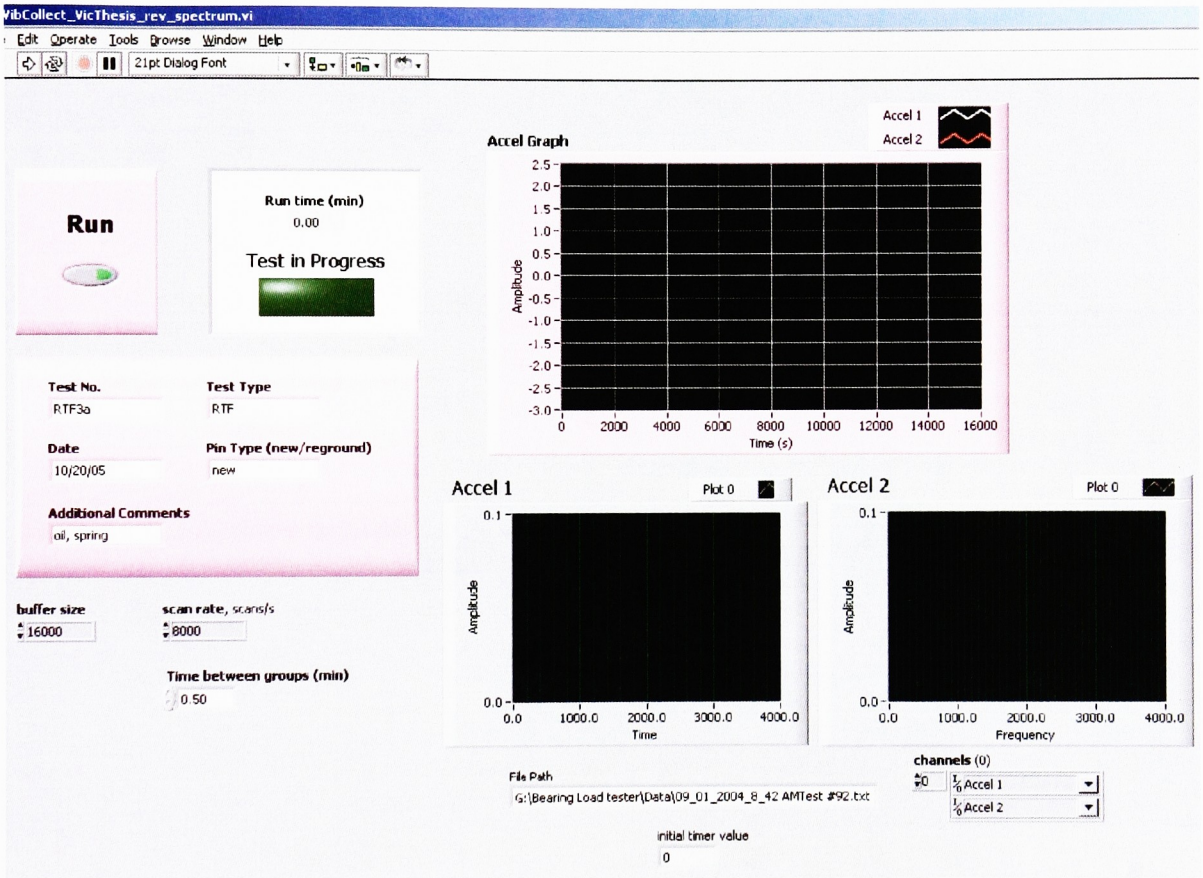

Figure 25. Screenshot of User Interface for Vibration DAQ LabVIEW Program

The two separate LabVIEW programs "communicate" via the motor voltage signal. The original BT LabVIEW program sends a small voltage to the motor. This voltage acts as a switch, allowing the motor to turn on. A channel was set up in the new vibration monitoring LabVIEW program that senses the presence (or lack of) of the voltage sent from the original

LabVIEW program to the motor. The vibration-monitoring program was coded in such a way that prevents it from collecting data until a motor voltage signal is recognized by this channel (indicating that the test is running). Therefore, if a safety limit is tripped in the original BT LabVIEW program (resulting in a test shut-down), the new vibration monitoring LabVIEW program will stop collecting data.

5.0 Test Plan and Procedure

The test plan for this study was divided into two phases: baseline testing, and run to failure (RTF) testing. Baseline tests were conducted to gather an initial understanding of the differences between the vibration signatures produced from new and worn bushings. Data from RTF tests will be compared to the baseline tests. RTF testing begins with a healthy, new DX bushing that is operated in the rig until the acetal interface layer of the bushing has worn. A bushing is considered "worn" once the layer of acetal has worn through revealing the bronze sinter layer (see Figures 6a and 6b). It is anticipated that a vibration signature change will be recognized during RTF testing that can be related to the amount of radial bushing wear. The test matrix used to complete this testing is illustrated below in Table 4:

Test Matrix

NOTE: temperature and load will be held constant at 250°F and 1000lb, respectively

Test Type	Interface bearing	Test No.
[1]Baseline	new garlock DX bushing	1
		2
		3
		4
		5
		6
	worn garlock DX bushing	7
		8
		9
		10
		11
		12
[2]RTF	new garlock DX bushing	13
		14
		15
		16
		17
		18

[1]Baseline tests will run until steady-state temperature is reached, then characterization data will be collected

[2]RTF tests will be run until the bushing has worn completely

Table 4. Test Matrix

5.1 Baseline Testing

A series of baseline tests is used as a preliminary comparison for new versus worn bushing signatures. Worn bushings are those that no longer have an acetal lining (Figures 6a and 6b). These bushings were taken from previous temperature-wear correlation tests that CIMS personnel had conducted on the BT. Twelve tests (six per bushing type) were conducted to compare the baseline vibration signatures of new and (previously) worn bushings.

5.2 Run to Failure Tests

The core experimental phase of this study consisted of ten RTF tests run at an operating temperature of 250°F and a load of 1000 lb. Vibration data was collected as the bushing wear progressed from 0.0000'' to 0.0120''. Radial bushing wear was monitored with the digital indicator noted in Section 4.1.4. Vibration data was sampled synchronous with wear measurement using the LabVIEW program discussed in Section 4.4.2. Since bushing wear is not necessarily linear, vibration data was not collected at regular wear intervals. Instead, data was collected at every change in wear amount, which could quickly jump as much as 0.0040''.

5.3 Test Procedure

All tests were conducted at a 1000 lb operating load and 250°F pin-bushing interface temperature. To comply with the typical test procedure previously used by CIMS [24], the BT was disassembled and reassembled between each test. The test procedure used for this study is outlined below:

- Turn the motor switch off and disassemble the BT as described in [24]; insert the bushing to be tested into the bushing block and the corresponding pin into the pulley
- Reassemble the BT as described in [24] and start the new test:
    - Begin the test with a 10 minute break-in period at 50 lbs
    - Allow the load to ramp up to 1000 lbs after the break-in period
    - Once the system has reached a steady-state temperature, the first vibration dataset should be collected. From this point, collect vibration data synchronously with bushing wear (as specified by the digital wear indicator).

6.0 Experimentation

6.1 Accelerometer Selection

Accelerometers were selected based on the literature review in Section 3.4.1 and Appendix C to acquire vibration signature data from the bushing wear tests. Several parameters were considered. The major limiting factors when choosing accelerometers for this application included accelerometer size and maximum operating temperature. Accelerometer size and operating temperature restrictions were imposed by the BT rig itself (Figures 21a, 21b, 24a, and 24b). In an effort to locate the sensors as closely as possible to the point of interest (the pin-bushing interface), it was decided that the best position for the accelerometers would be to attach them directly to the bushing block (inside of the bushing block housing). Therefore, the limited space in the bushing block housing escalated the importance of size when selecting accelerometers. Additionally, a minimum operating temperature of 240°F was desired during testing in order to keep test lengths to a minimum. Finding an accelerometer both small enough and durable enough for the operating environment proved difficult. However, two Kistler piezoelectric accelerometers were found that met these requirements, model numbers 8774A50 and 8776A50M6 (see Appendix D for specifications [38]). These accelerometers were small enough to fit into the housing and can withstand temperatures up to 250°F. The only difference between the two accelerometers is the electrical connection position; model 8776A50M6 connects via the side of the accelerometer while model 8774A50 connects via the top of the accelerometer. The different connection points were helpful in working around the physical constraints of the BT bushing block housing.

As discussed in the literature review (Section 3.4.1, [12, 16, 36]), accelerometer size and the proposed operating environment are certainly not the only factors to be aware of when selecting accelerometers for an application. Amplitude range and sensitivity, frequency response, and mounting style are also vital selection criteria. The selected Kistler accelerometers have a frequency response of 1 Hz to 10 kHz. As previously mentioned, this value is appropriate since the system is mechanical and will therefore produce relatively low frequency signatures [19]. The amplitude range and sensitivity of the accelerometers is specified as ±50g and 100mV/g, respectively. The amplitude range and sensitivity are typical for a general-purpose accelerometer [36] and are considered acceptable for this study [19]. The Kistler accelerometers selected for testing were capable of being stud-mounted for maximum data transmission accuracy. Unfortunately, this characteristic could not be taken advantage of in this particular application due to spacing considerations within the BT as noted below in Section 6.1.1.

6.1.1 Accelerometer Mounting Technique

In this study, data from two axes was desired. However, the limited space in the BT housing necessitated the use of a mounting block to attach the accelerometers to the bushing block. Based on the literature review in Appendix C, this mounting method is less desirable due to the resultant reduced frequency response of the accelerometer. Unfortunately, it was the only existing option if two accelerometers were to be used. The accelerometers were screwed into appropriate sides of the tapped mounting block (Kistler, Model Number 8524). A mounting magnet (PCB Piezotronics, Inc., Model Number 080A27) was screwed into a third side of the block so that the accelerometers (and mounting block) could be attached (magnetically) to

the bushing block. As recommended in Appendix C, a layer of oil was applied between the bushing block and mounting magnet to facilitate signal transmission.

6.2 Equipment Validation

The Bushing Tester has been used at CIMS for several years and has gone through many phases of improvements. Prior to the start of this study, over one hundred consistent bushing failure tests had been conducted on the BT. These failure tests from the BT were successfully correlated [27, 28] to failure tests conducted on the dynamometer, and results from both the dynamometer and BT were comparable. Since the dynamometer uses actual planetary assemblies and failure data from the BT closely matched that from the dynamometer [27, 28], the BT is considered to be a valid test rig for bushing wear.

As previously mentioned, the two Kistler accelerometers were purchased new, and since they had never been used before, a simple test was carried out to assure their accuracy. A cantilever beam was set up by clamping a thin, steel bar (1.59''x 0.82''x 0.0625'') to a bench top as shown in Figures 26a and 26b.

Figure 26a. Equipment Set-up, Photo 1

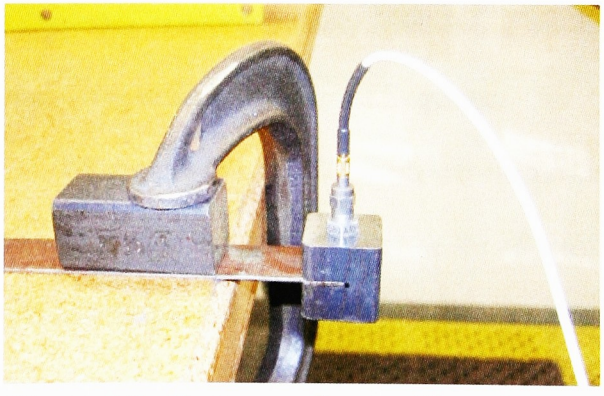

Figure 26b. Equipment Set-up, Photo 2

Accelerometers were mounted to the beam one at a time with a magnetic coupling. An oil film was used between the accelerometer mounting magnet and mass to increase vibration signal transmission accuracy. The accelerometer output was monitored (in real time) with a dynamic signal analyzer (Hewlett Packard, Model Number 35670A). The beam was 'plucked' and the output was observed. The same process was repeated for the second accelerometer as well as two additional accelerometers (PCB Piezotronics, Model Numbers 352C65 and 352C66) that were recently used in an un-related (CIMS) project by the author. Since all four accelerometers produced similar time domain responses and reported the same natural frequency of the assembly (80 Hz), it was concluded that the new Kistler accelerometers were functioning properly.

6.3 Scan Rate and Sample Length Determination

Before testing could begin, an appropriate sampling rate was determined. This was done so by a simple trial-and-error technique. The scan rate was continually increased until there were no observable differences in the resulting power spectrum and time plot. For example, Figure 27 below shows the frequency domain signature of the system when sampled at 20 kHz. As illustrated, the largest significant frequency is approximately 2500 Hz. This minimum frequency was multiplied by two in order to find the Nyquist frequency. As previously mentioned in the literature review, the sample rate should be greater than twice the Nyquist frequency [1]. Therefore 8 kHz was chosen as the sampling rate for all tests. This sampling rate will result in valid data up to a frequency of 4 kHz. In Figure 27, there are extremely low amplitude signatures between 4000 Hz and 4500 Hz. Due to the sampling rate, these signatures could get aliased back to between 0 Hz and 500 Hz. This is not an

issue for data analysis in this study since, as discussed in Section 6.5, the frequency bands of interest are between 900 Hz and 2100 Hz. Furthermore, the small amplitude of the vibration signatures between 4000 Hz and 4500 Hz would result in very low band power (relatively), therefore their aliased effect is considered negligible.

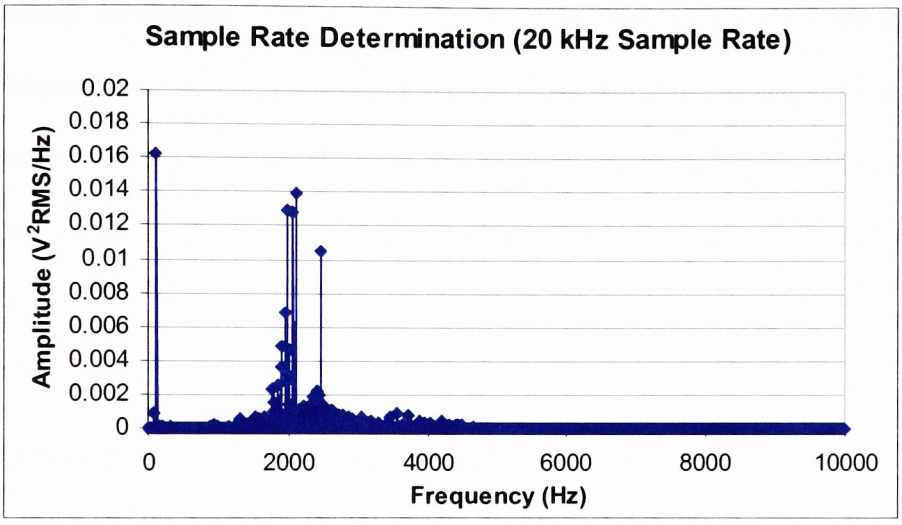

Figure 27. Sample Rate Determination

A sample length of two seconds was chosen. This results in a frequency resolution of 0.5 Hz, which is more than adequate for the purposes of this study [19].

6.4 Test Matrix Adjustment

Preliminary bushing wear testing made it clear that the initial test matrix in Table 4 could not be followed exactly. Baseline testing of worn bushings was unable to be completed (Section 6.4.1), and interesting frequency components were observed from the vertical accelerometer that warranted further testing than that scheduled in the original test matrix (Section 6.4.2).

6.4.1 Omitted Baseline Testing

Baseline testing for healthy gears was completed as planned in Table 4. Unfortunately, baseline data for worn bushings could not be acquired. The metal-to-metal contact generated too much heat, thus tripping the safety limits included in the BT LabVIEW program and stopping the test. In addition to being dangerously high, these temperatures exceeded the operating temperature limits of the accelerometers. Therefore, the baseline testing section was scrapped from the original matrix in Table 4 since, without data from previously worn bushings, the original purpose of baseline testing (discussed in Section 5.1) could not be achieved.

6.4.2 Added Bushing Dimple Geometry Testing

Several frequency components were observed in the frequency spectrum from the vertical accelerometer, which appeared to "characterize" bushing behavior. Since in the vertical direction, these vibration signatures were assumed to be a result of a rotational force that the bushing and block were experiencing. It is believed that these signatures are due to a cyclic change in lubrication at the pin-bushing interface because the block is stationary and the pin is rotating. The possibility that these frequency components were attributed to structural vibrations of the BT was discounted via RTF testing. Representative frequency-domain graphs appear in Figures 28 and 29 which show that once the acetal layer was completely worn from the bushing, the majority of the frequency components in the vertical direction (accel 1) disappeared or showed a dramatic amplitude reduction, indicating that they were, in fact, signatures of the bushing's acetal layer. These observations were mimicked by the horizontal (accel 2) accelerometer data (Appendix E).

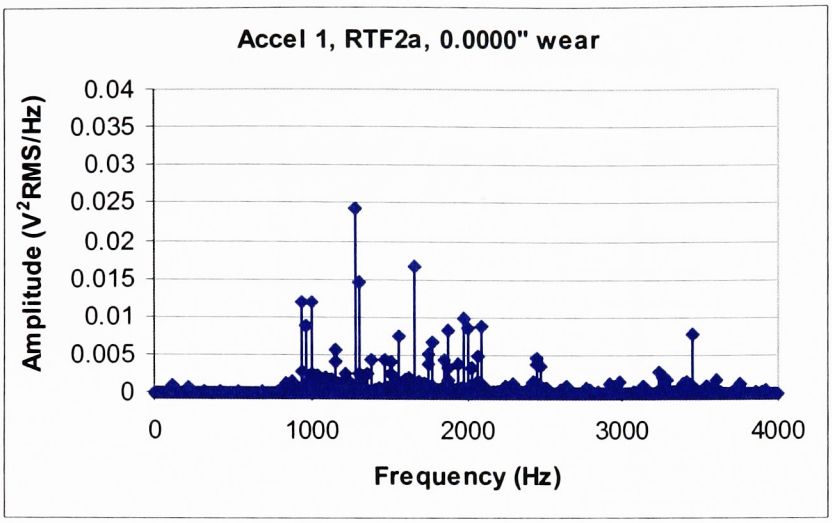

Figure 28. RTF Test 2, Bushing wear = 0.0000'' (most acetal remaining)

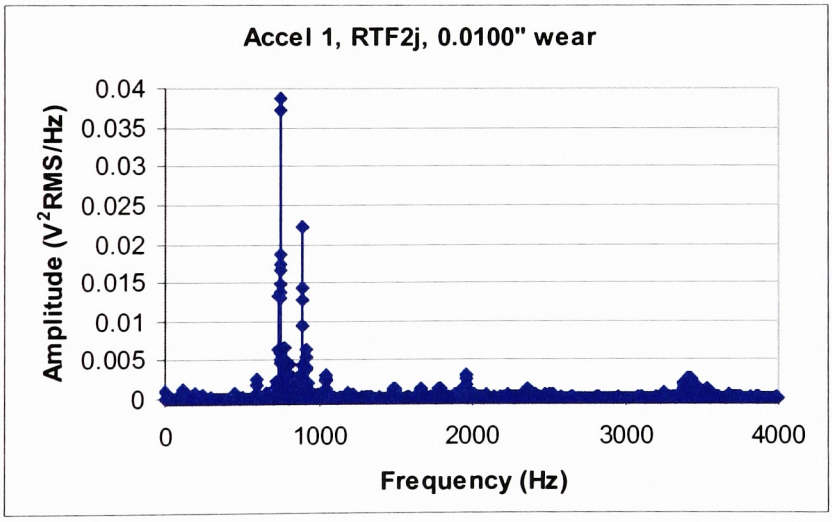

Figure 29. RTF Test 2, Bushing wear = 0.0100'' (little acetal remaining)

To investigate these signatures, additional testing was conducted and the effect of the bushing dimple size on this signature was examined. The new test matrix to accommodate the revised investigation is shown below in Table 5:

Adjusted Test Matrix

*Temperature and load are held constant at 250°F and 1000lb, respectively

Test Type	Details/Description	Test No.
RTF	new DX bushing	1
		2
		3
		4
		5
		6
	DX bushing with enlarged dimples	7
		8
		9
		10
		11
		12

Table 5. Updated Test Matrix

The hypothesis under test is the supposition that as the acetal lining wears, the lubrication dynamics in the pin-bushing interface will change, thereby shifting the frequency signatures of interest. These signatures, in turn, could be used to indicate bushing wear.

6.5 Data Analysis Technique

As previously mentioned, all vibration data analysis in this study was Fast Fourier Transform-based (see Appendix N for representative time plots from RTF Test 2). First, data collected from the accelerometers was processed using the LabVIEW Auto Power Spectrum Virtual Instrument (VI) that is available in the National Instruments (NI) Sound and Vibration Toolkit. This VI computes the single-sided power spectrum of the time-domain vibration signal. The VI requires that the input time-domain signal contain at least three cycles for accurate transfer via the FFT. Since each data sample will be recorded for two seconds, this VI requirement was easily met. The equation used by the VI to compute the power spectrum is:

$$\text{Power Spectrum} = \frac{\text{FFT}^{*}(\text{Signal}) \times \text{FFT}(\text{Signal})}{n^2}$$

where n is the number of points in the **Signal** and * denotes complex conjugation [2]. Once the power spectrum is calculated, the VI adjusts the nominal dual-sided spectrum into a single-sided power spectrum. The power spectrum computed by the VI was further processed by breaking the spectral power versus frequency plot up into frequency-bands and calculating the area under the curve of those respective bands (see Appendix F for sample spreadsheet calculations). Data from both the vertical and horizontal accelerometers was processed in this manner. The frequency bands were first selected based on an observation of the spectral power versus frequency plot. Figure 30 represents a frequency domain plot from the vertically positioned accelerometer (accel 1) of an RTF test.

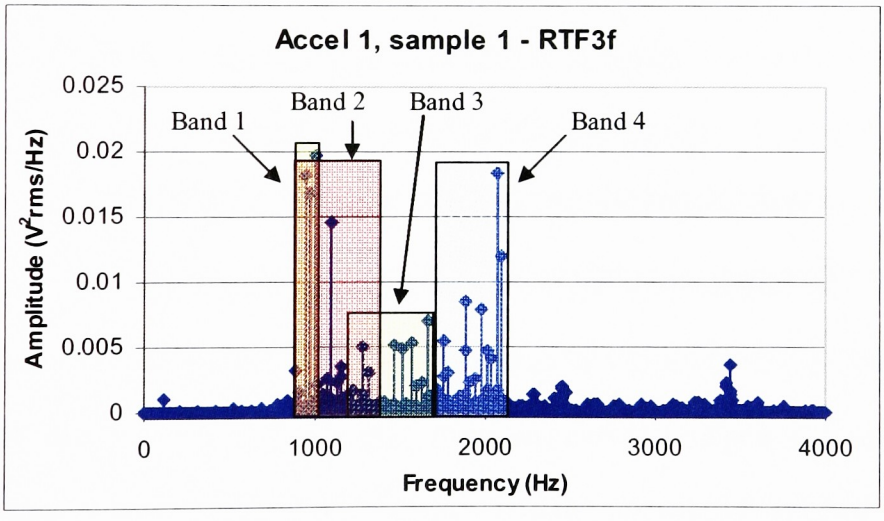

Figure 30. Frequency Domain Plot from RTF3f, Vertical Accelerometer

Frequency bands with a large amount of "activity" were chosen for analysis. As a first stage analysis, the following four frequency bands were examined: 900 – 1000 Hz, 900 – 1400Hz, 1200 – 1700 Hz, and 1700 – 2100 Hz (bands 1-4, respectively) [18]. Again, these were

selected based on frequency domain plots of the RTF tests. Two additional bands from 1250 – 1350 Hz and 2550 – 2700 Hz were included and are discussed in Section 6.5.1.

6.5.1 Frequency Bands 2550 – 2700 and 1250 – 1350 Hz

As previously mentioned, one area of interest in examining the vibration signatures is the bushing dimples. The number of dimples in 20 bushings was counted by the author (see Appendix G for detailed data). The average and standard deviation were calculated to be 92.3 ± 1.2 dimples per bushing. The number of dimples per bushing ranged from 88 to 93. This range was multiplied by the rotational frequency of the pin (29 Hz) and the first sub-harmonic was examined to identify signatures that may be related to the dimples as shown below:

$$\text{Lower limit: } = 88 * 29Hz = 2552Hz$$

$$\text{Upper limit: } = 93 * 29Hz = 2697Hz$$

$$\text{First Sub-harmonic lower limit: } = 0.5 * (2552Hz) = 1276Hz$$

$$\text{First Sub-harmonic upper limit: } = 0.5 * (2697Hz) = 1348.5Hz$$

Based on these calculations, the 1250 – 1350 Hz and 2550 – 2700 Hz frequency bands were included in the data analysis. The area under the power curve (band power) from each specified frequency band of interest was plotted versus the amount of linear bushing wear that was recorded using the digital indicator.

6.6 Results of RTF Testing

After baseline testing from the original test matrix and most of the RTF testing (from the adjusted test matrix) was conducted, it was noticed that the bushing block had cracked from

fatigue (see Section 9.1 for details). Therefore, a new block was ordered from the same tooling company (Morgood Tool, Rochester, NY), who made the first block and the six RTF tests were repeated. Baseline testing was not repeated since it was now known that baseline testing for worn bushings could not be acquired. Also, similar frequency-domain plots from the first set of baseline tests had already showed data consistency between test trials. Therefore, running a set of specific baseline tests would not add any value to the current wear study. The results discussed below are from the second set of RTF tests with the new bushing block.

Six RTF tests began with new bushings and progressed until the acetal layer was worn. Each test was analyzed as described in Section 6.5 to create frequency band power versus wear plots. Of the six tests, two were omitted since the ball bearings that support the pin began to wear, thus distorting the vibration signature. Data collection showed unusual vibration signatures, and once the BT was disassembled after these two tests it was noticed that the bushings had not worn evenly across the area that is in contact with the pin. Unfortunately, replacing these bearings without altering other BT components could not be achieved due to unexpected difficulties. (This topic is discussed in detail in Section 9.2).

Data from the four remaining RTF tests was analyzed as described in Section 6.5 (see Appendix O for temperature and wear plots of RTF tests). Results showed that the 1700 to 2100 Hz frequency band correlated bushing wear to vibration signature better than the other frequency bands. Therefore, band power (of 1700 to 2100 Hz frequency band) versus wear plots from the horizontal accelerometer (accel 2) of the four RTF tests are illustrated below

in Figures 31 through 34 (see Appendix H for results from other frequency bands and representative test details of RTF2).

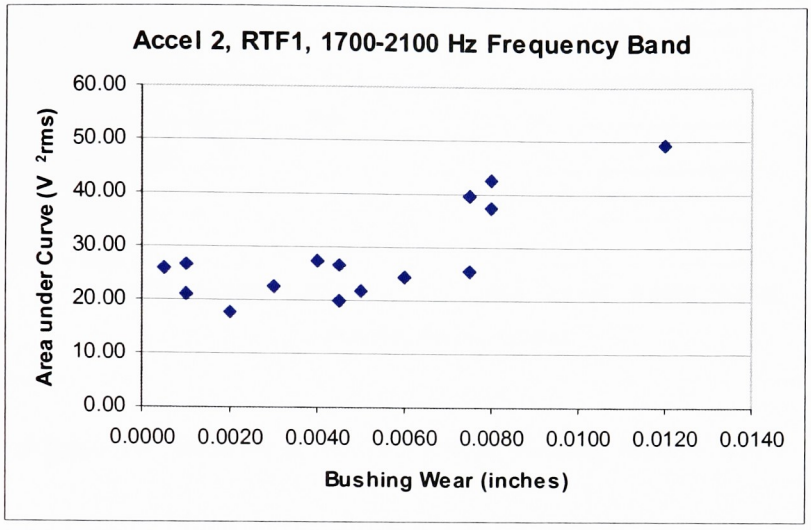

Figure 31. Area Under Curve versus Bushing Wear – RTF1

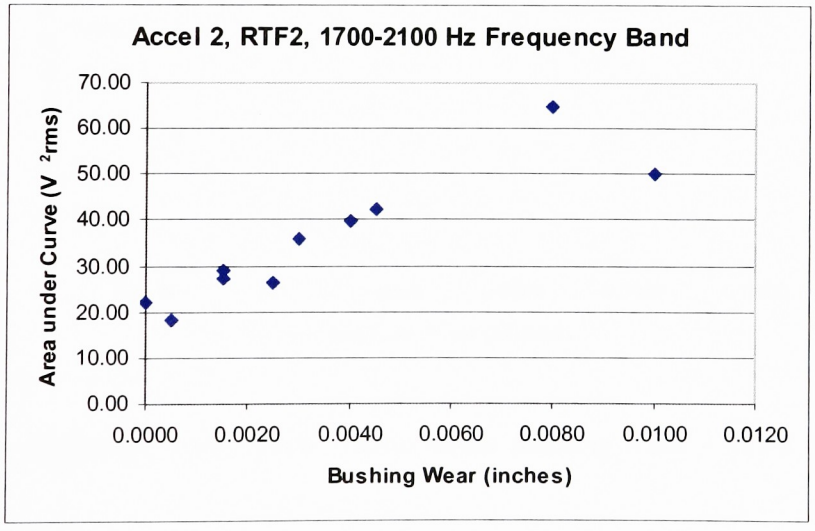

Figure 32. Area Under Curve versus Bushing Wear – RTF2

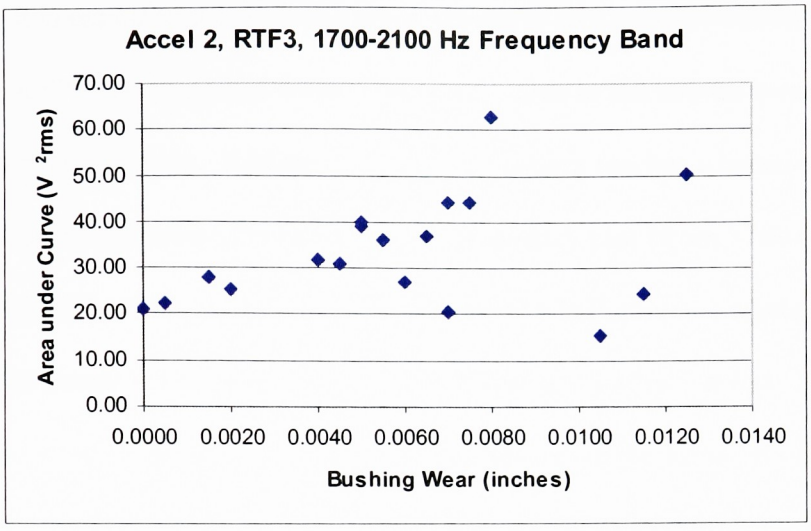

Figure 33. Area Under Curve versus Bushing Wear – RTF3

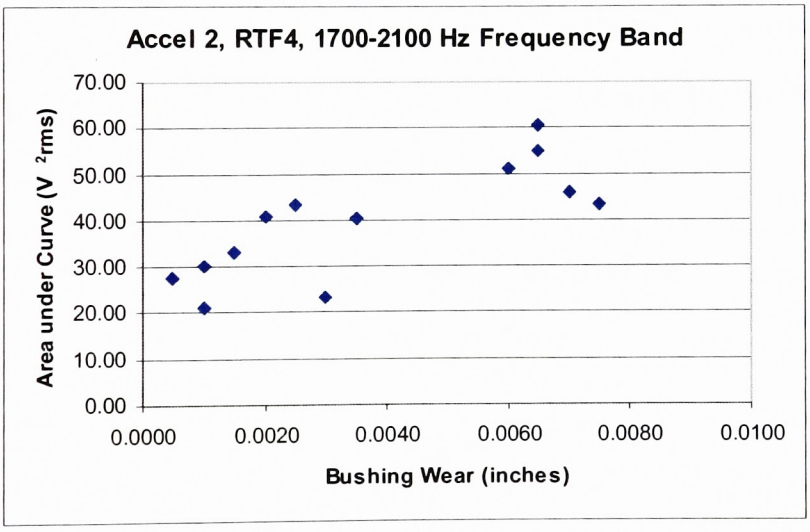

Figure 34. Area Under Curve versus Bushing Wear – RTF4

The common upward trend shown in Figures 31-34 suggests a direct relationship between band power of the 1700 to 2100 Hz frequency band and bushing wear. Upon disassembly, it was noticed that the bushing from RTF1 did not wear completely even (see Section 9.4 for details). This was attributed to "breaking in" the new block. Since only part of the contact

area had worn, it is expected that the area under the curve of a specific bandwidth would be slightly less than if the bushing had worn completely. Due to the uneven wear, RTF1 was omitted from further analyses. Additionally, once a bushing reaches a certain threshold of wear, the area under the curve of the power verus frequency plot (from 1700 to 2100 Hz) decreases dramatically. This is especially evident in RTF3 (Figure 33) where the amplitude drops from approximately 65 V^2rms at 0.0080'' of wear to 15 V^2rms at 0.0105'' of wear. A graph was made where Figures 32, 33, and 34 were plotted on the same set of axis with linear fits (Figure 35). Data points above 0.008'' of wear were eliminated from the plot so that a trendline could be fitted to the data. Truncating the data at 0.0080'' of wear is acceptable for this current study since, at this state of bushing life, extensive wear has occurred and the bushing is beyond the "point of no return." The goal of this thesis is to recognize wear at an early stage in bushing life so that appropriate action can be taken by the USMC to prolong bushing life and avoid secondary component failures.

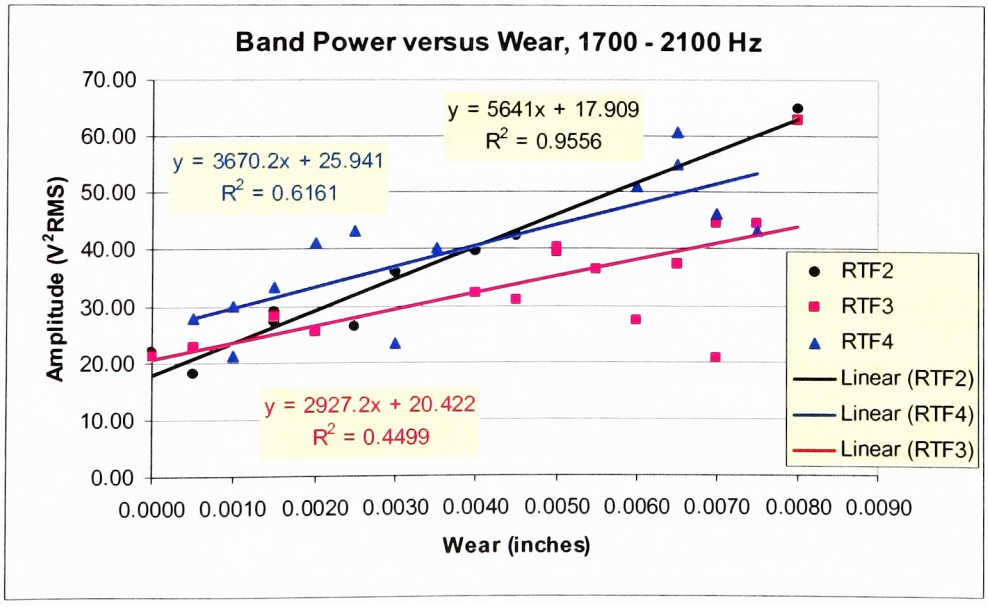

Figure 35. Accel 2, 1700-2100 Hz Frequency Band, RTF2, RTF3, and RTF4 with trend-lines plotted from 0.0000'' to 0.0080'' of Wear

The next step was to take a look at the individual tests and remove any outliers that exist. Outliers were eliminated based on the 95% confidence interval rule (see Section 7.1.1 for confidence interval used for predicting bushing wear from band power). Data from the three tests was imported into MATLAB so that confidence interval bands could be added to the plot using the "polytool" command (see Appendix I for MATLAB code and individual confidence interval plots). Outliers located beyond the 95% confidence interval bands were eliminated. Test RTF3 contained the only outlier. The graph in Figure 35 was reconstructed omitting the outlier that was established using MATLAB. This new plot is illustrated below in Figure 36.

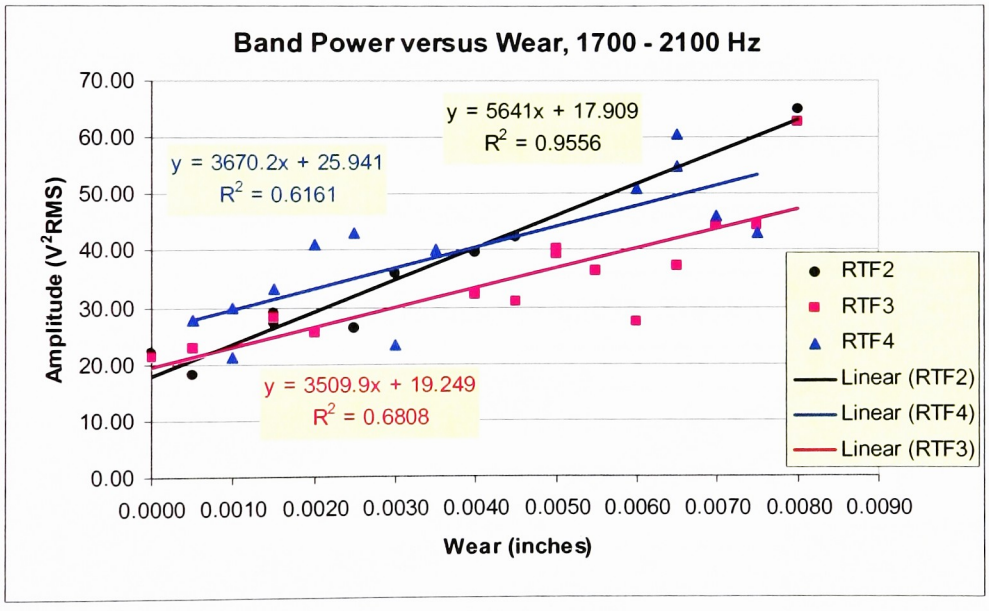

Figure 36. Accel 2, 1700-2100 Hz Frequency Band, RTF2, RTF3, and RTF4 with trend-lines plotted from 0.0000'' to 0.0080'' of Wear less the outlier highlighted in Appendix I

As illustrated, results from this first stage analysis show significant wear-signature correlation in the 1700 – 2100 Hz band of the radially positioned accelerometer (accelerometer 2). The linear fits produced R^2 values ranging from 61.6% to 95.6%. Table 6 below includes summary data of the three resulting trendlines.

1700-2100 Hz Trendline Summary		
	Slope	Intercept
RTF2	5641	17.909
RTF3	3509.9	19.249
RTF4	3670.2	25.941
Average	4273.7	21.033
Standard Deviation	1186.826	4.302935

Table 6. 1700-2100 Hz Trendline Summary

The standard deviation of the slopes and intercepts of the three trendlines are 1186.8 and 4.3, respectively. In an effort to reduce these values and further pinpoint the significant frequency band, the 1700 to 2100 Hz band was dissected into 100 Hz intervals: 1700 to 1800 Hz, 1800 to 1900 Hz, 1900 to 2000 Hz, and 2000 to 2100 Hz. These frequency bands were examined in a similar manner to the 1700 to 2100 Hz band. The analysis showed that the 2000 – 2100 Hz band had the best bushing wear-vibration signature correlation. The final plot for this frequency band (omitting outliers) is illustrated in Figure 37 (see Appendix I for analysis details). As with the 1700-2100 Hz band, only one outlier was omitted from RTF3.

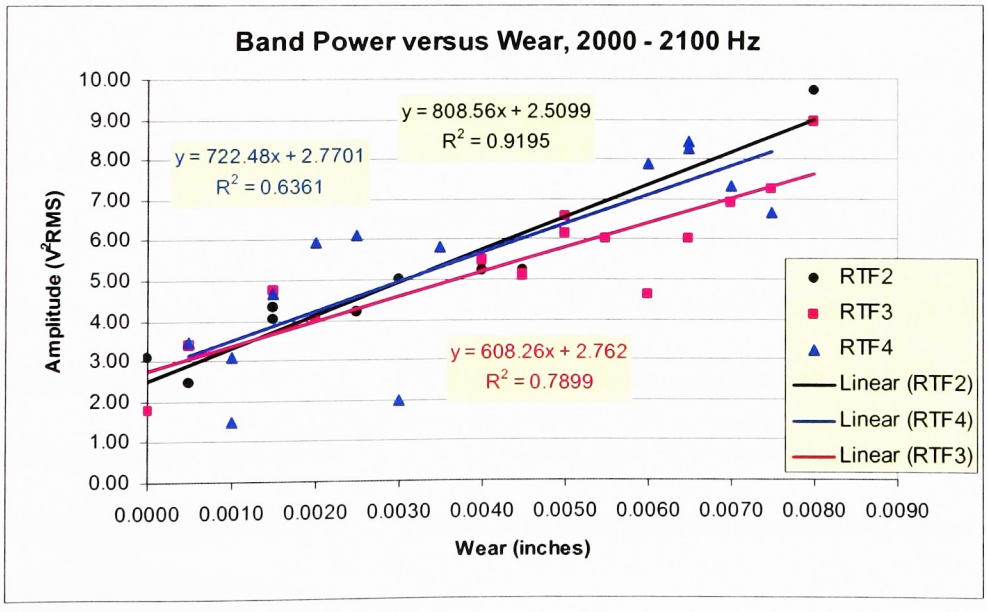

Figure 37. Accel 2, 2000-2100 Hz Frequency Band, RTF2, RTF3, and RTF4 with trend-lines plotted from 0.0000'' to 0.0080'' of Wear less the outliers highlighted in Appendix I

The plot in Figure 37 indicates a clear relationship between the band power of the 2000 to 2100 Hz frequency band and bushing wear. The R^2 values of 63.6%, 79.0%, and 92.0% are indicative of this direct relationship between band power and bushing wear. Summary data for the trendlines is provided in Table 7.

2000-2100 Hz Trendline Summary

	Slope	Intercept
RTF2	808.56	2.5099
RTF3	608.26	2.762
RTF4	722.48	2.7701
Average	713.1	2.6807
Standard Deviation	100.479	0.14794

Table 7. 2000-2100 Hz Trendline Summary

The standard deviation of the slopes and intercepts of the three trendlines for the 2000-2100 Hz frequency band are 100.5 and 0.148, respectively. Since the data from these three tests matches closely, it suggests repeatability between RTF tests on the BT. Disassembling and reassembling the BT and changing the bushing and pin do not appear to alter the vibration signature of the system as evidenced by Figure 37 and Table 7.

6.7 Results of Large Dimple RTF Testing

Three RTF tests were conducted using bushings with enlarged dimples (Figures 38a and 38b). The size of the dimples was increased manually by the author using a Dremel® tool (3/32-inch spherical grooved end tool). The precise circular geometry of the bushing dimples could not be accurately maintained with the Dremel® tool. This was considered acceptable, however, since the desired result of these tests is to determine the (qualitative) effect, if any, of dimple geometry on the bushing signature.

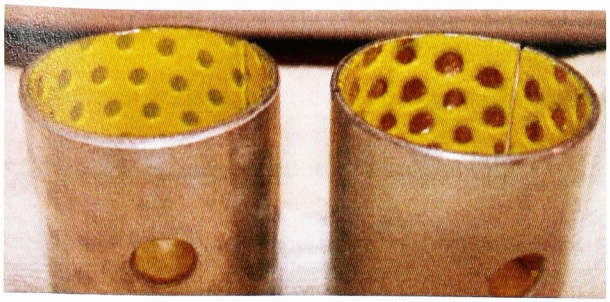

Figure 38a. Enlarged bushing dimples, Photo 1

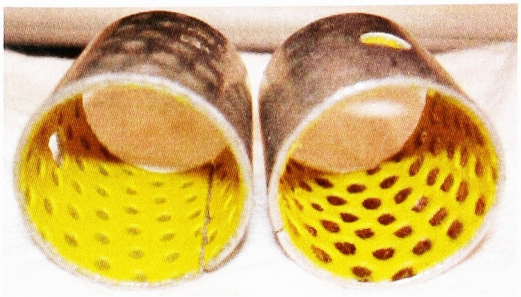

Figure 38b. Enlarged bushing dimples, Photo 2

Unfortunately, the BT radial ball bearings that support the pin began fretting before the enlarged dimple testing began. Therefore, a new set of baseline data was acquired from the BT after the new ball bearings were installed. This consisted of six RTF tests with new bushings. Results from large dimple RTF testing were compared to this new set of baseline data. (For more information on the effect of bearing changes on vibration signature, see Section 9.2). The six RTF tests did not match RTF tests 2, 3, and 4. This is, in part, due to the change in vibration signature that resulted from replacing the bearings. However, after the bearings were replaced, the bushings began wearing unevenly. This is most likely the major cause of the vibration signature differences between the first (RTF 2, 3, and 4) and second (six RTF tests with the new bearings) sets of RTF tests. The bearings also wore unevenly during large dimple testing. Therefore, it should be kept in mind that the data discussed in this section is preliminary in nature. Since consistent wear samples with large dimples could not be obtained, inferences cannot be made without further testing. Any obvious differences that may be seen when comparing typical bushings to those with large dimples could suggest relationships and warrant further testing on this subject matter. Additional details regarding uneven bushing wear are discussed in Section 9.4.

Results of RTF large dimple testing showed no notable frequency shift in bushing vibration signatures with regular dimples compared to those with large dimples. This is evidenced in Figure 39, where frequency components from the bushing with regular dimples (solid blue components) closely match those from the bushing with enlarged dimples (dotted magenta lines). Both bushings in this plot were at a beginning stage of wear (0.0015''). Similarly, Figure 40 illustrates the close match between bushings with regular and large dimples at an advanced stage of wear (0.0070''). In Figures 39 and 40, the frequency range was zoomed to 500 - 2500 Hz for a finer examination of the frequency bands. Additional supporting plots are provided in Appendix J.

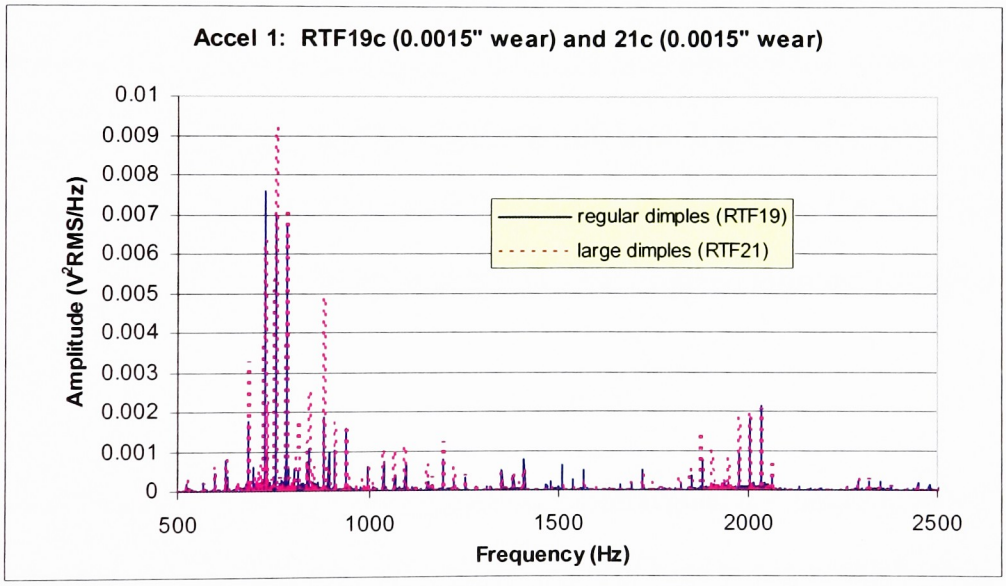

Figure 39. Large and Regular Bushing Dimple Comparison at low wear stage

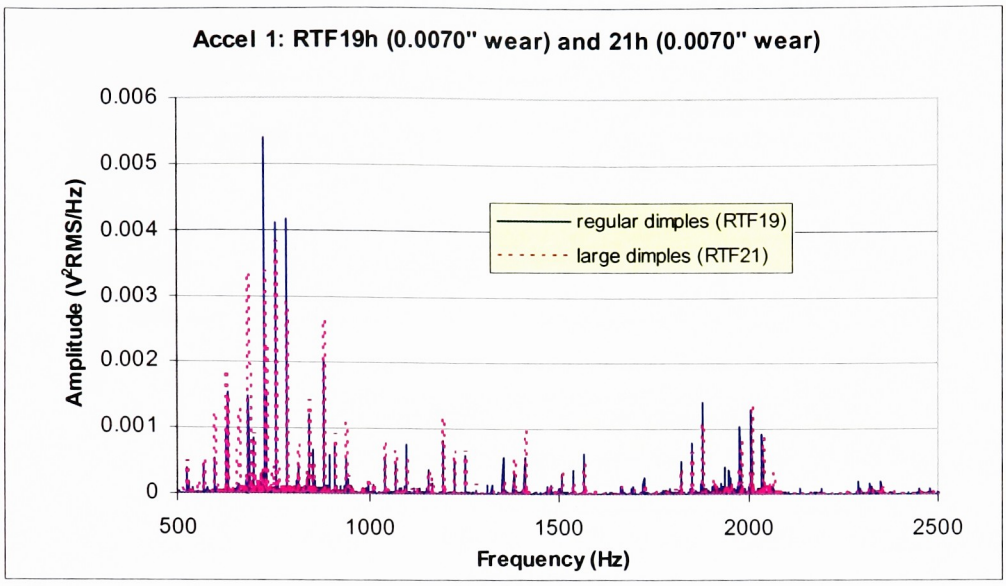

Figure 40. Large and Regular Bushing Dimple Comparison at significant wear stage

As illustrated in Figures 39, 40, and Appendix J, there is no observable frequency shift between bushings with regular dimples and those with large dimples. However, differences in amplitude are noticed between the two dimple types. Unfortunately, the amplitude differences are not consistent. This is mimicked in data acquired from accelerometer 2 (see Appendix J).

Band Power vibration data collected from bushings with regular and large dimples was also examined using power spectral density analysis. Plots of band power versus bushing wear were constructed where data from bushings with large dimples and regular dimples were included on the same graph (Figure 41). Additional plots are provided in Appendix K.

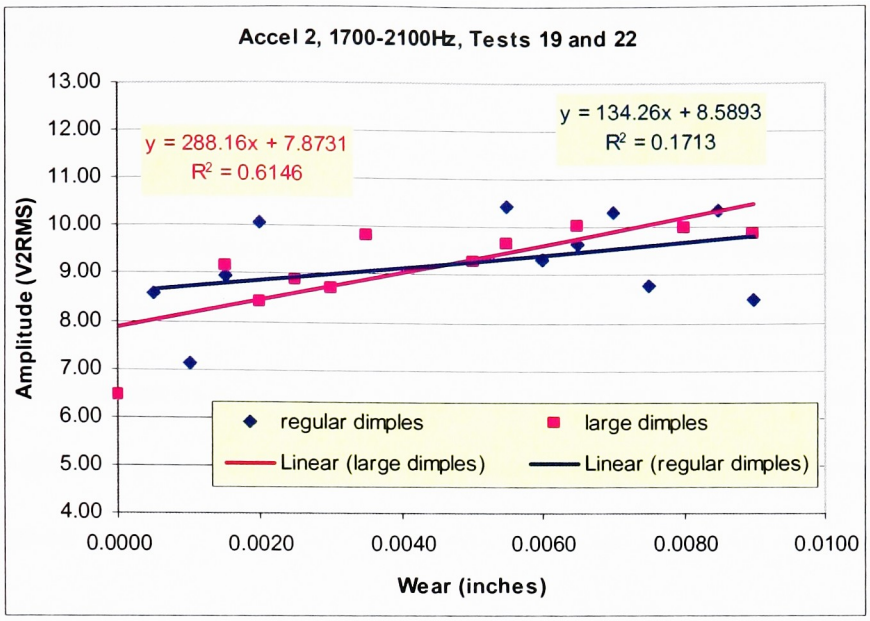

Figure 41. Bushing with large dimples versus bushing with regular dimples

The bushings with large dimples resulted in a much better linear fit than the bushings with regular dimples. However, as shown in Appendix K, these results are not consistent with those from the other tests. Therefore, band power analysis was inconclusive.

7.0 Conclusion

7.1 RTF Testing

Several run to failure tests were completed in this study in which new bushings were subjected to accelerated life testing on the BT. Vibration data was collected via two piezoelectric accelerometers at random bushing wear increments. The data was analyzed in the frequency-domain to develop band power (of narrow frequency bands) versus bushing wear plots. Based on the results of these RTF tests (discussed in Section 6.6), it is concluded that determining bushing wear via vibration signatures is feasible. This is strongly evidenced by the plot of band power of the 2000 to 2100 Hz frequency band versus bushing wear that is illustrated in Figure 37. The direct, linear trends between band power and bushing wear result in a simple relationship between the two that can be used to infer the amount of bushing wear given the band power from 2000 to 2100 Hz. This method appears to be more effective than the temperature-based wear correlation previously developed by CIMS. Results of this current study show that vibration signature data identifies bushing wear at a much earlier stage of wear (during RTF tests on the BT) than temperature data was able to.

The increase in band power displayed in Figures 36 and 37 (and other plots in Section 6.6) is consistent with the literature review in Chapter 3.0 of this current study. For example, Cavacece and Introini [4] utilized frequency-domain analysis to reveal a direct relationship between auto-power spectrum amplitude and ball bearing wear (as evidenced by the upward trend of the graph in Figure 11). Furthermore, recall that Peng and Kessissoglou [25] stated that wear mechanisms of gears can manifest themselves through increasing energy content in

narrow-band frequencies. Results of this current study show that energy content in narrow-band frequencies can be applied to bushing wear as well as to gear wear. Finally, results from the study completed by Liberatore and Carman [20] demonstrated that frequency-domain analysis techniques could be used to relate the "structural damage" of a simply supported beam to a change in power spectral density energy. Results from the current study suggest "wear damage" likewise can be related to changes in power spectral density energy. Overall, a frequency-domain analysis technique was chosen for the current study based on previous wear analyses discussed in the literature review. Although the application of this specific bushing wear study was different from those discussed in the literature review, results showed that the narrow band power analysis technique could successfully identify bushing wear.

In an effort to identify the source of the vibration signatures that exist in the 2000 – 2100 Hz frequency band, it was observed that this signature correlates to the number of bushing dimples that are not in the wear area of the bushing [3]. For example, a band of approximately 20 dimples is worn during a bushing wear test on the BT (Figure 23a). Subtracting this number of worn dimples from the average number of dimples per bushing (92.3, see Appendix G for details) results in approximately 72 unworn dimples. Multiplying the number of unworn dimples times the rotational frequency of the pin (29 Hz) yields 2088 Hz. Since this value falls within both the 1700 – 2100 Hz and 2000 – 2100 Hz bands, it is possible that the number of unworn dimples is the source of the vibration signatures that identify bushing wear. Additional testing would be required to prove (or disprove) this hypothesis. However, if this hypothesis is true, it should be noted that if this study is

"scaled-up" to testing where the entire acetal layer of the bushing is wearing (as opposed to the localized wear resulting from the BT), the frequency band used to indicate bushing wear will most likely change since all of the dimples are wearing.

Also interesting is the "break-in" period that the bushings appear to experience during RTF testing. Figures 31, 32, and 33 of Section 6.6 illustrate this via the initial decrease in band power amplitude between the first few data points. Figure 42 below is a representative graph of the bushing "break-in" period that is experienced during RTF testing.

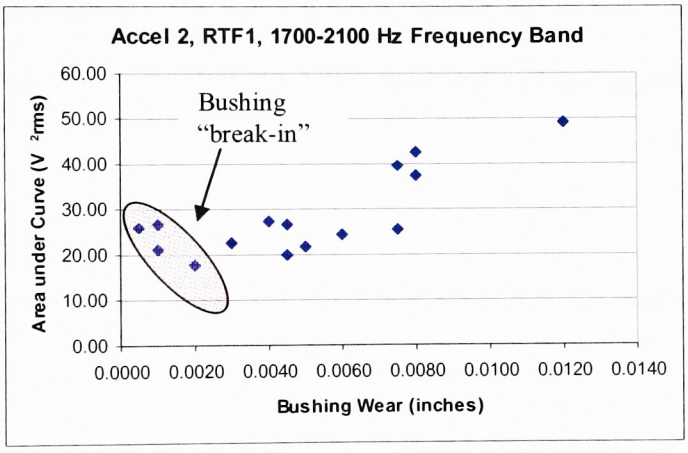

Figure 42. "Break-in" Period

The "break-in" period depicted in Figure X is supported by the literature review. Recall that Peng and Kessissoglou [25] discuss what should be expected when examining vibration signatures of gears. First, gears tend to go through a break-in period that shows relatively high vibration amplitudes. Once the gears have broken-in, the signature amplitudes decrease. Finally, as wear progresses, frequency amplitudes will increase [25]. This description fits, verbatim, with the narrow-band-power versus bushing wear results obtained in this study. Even though the application was different, the statement by Peng and Kessissoglou holds true for bushing wear analyses conducted during this study.

Although the results of this bushing wear study show that predicting bushing wear using vibration signatures seems feasible, second and perhaps third generation studies are necessary where the process is repeated on a physical system that closely simulates the entire planetary assembly. Before the idea is realized on an LAV, subsequent studies where the area of interest is less isolated must be completed. Suggestions for successive studies are discussed in detail in Chapter 8.0. Additionally, the plot in Figure 37 was obtained despite several variables associated with the BT rig. The slightest physical change in a mechanical system can alter the system's vibration signature. Therefore, several factors including ball bearing wear, uneven bushing wear, bushing block failure, and others made it difficult to collect consistent data. These problems are discussed in detail in Chapter 9.0.

7.1.1 Application of RTF Test Results

To implement vibration signature analysis of bushing wear onto an actual military vehicle, it is recommended that the data be analyzed differently than it was in this thesis. In the data analysis sections of this thesis that were used to evaluate the feasibility of bushing wear identification via vibration signature analysis, bushing wear was chosen as the independent variable since bushing wear was a concrete, measured value. However, in practice, band power will be the measured value while bushing wear will be indicated based on band power data. Therefore, when the idea is realized on an LAV, the axes should be inverted such that bushing wear versus band power is plotted. This will allow bushing wear to be identified based on measured band power data. Confidence interval plots (50%) of bushing wear versus band power based on accelerometer 2 were constructed for the 1700 – 2100 Hz and

2000 – 2100 Hz frequency bands of RTF2, 3, and 4. A representative plot of RTF2 for the 1700 – 2100 Hz band is shown in Figure 43 (see Appendix M for additional plots):

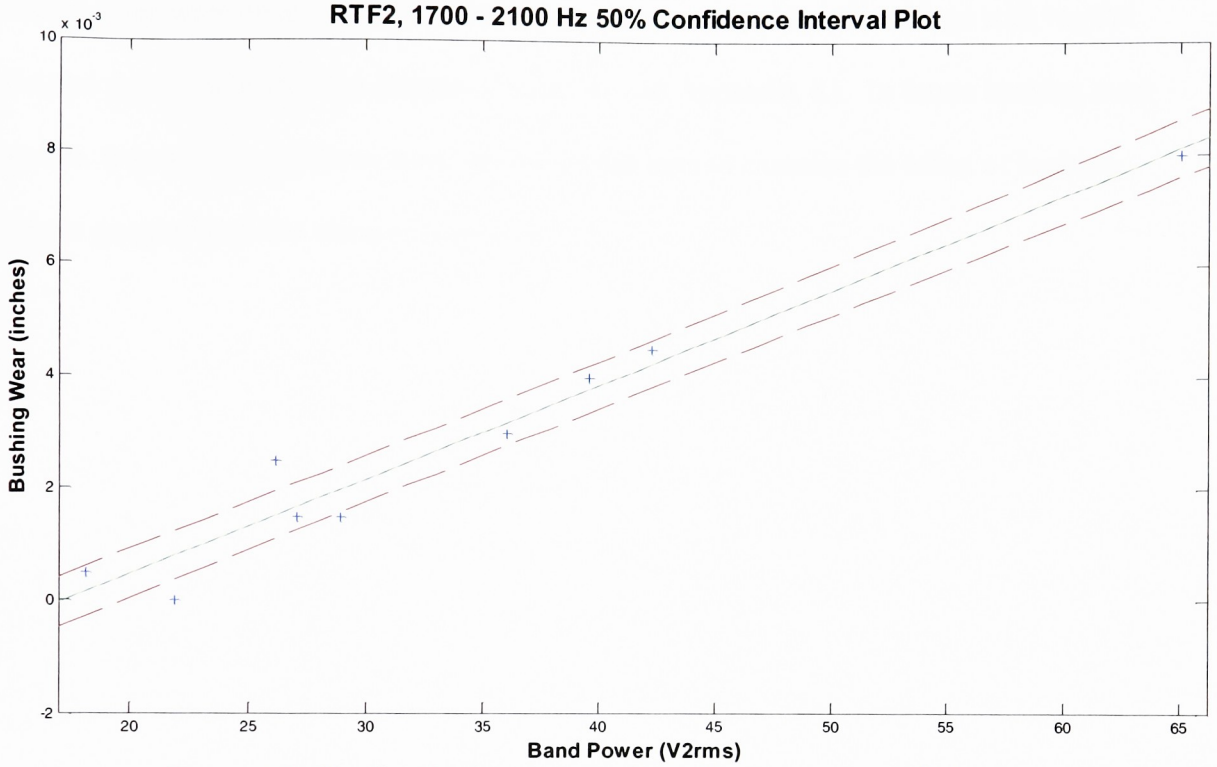

Figure 43. Plot for Application: Bushing Wear versus Band Power

As illustrated, the bushing wear versus band power plot allows for identification of bushing wear based on a measured band power value. For example, using a 50% confidence interval, a measured band power value of 40 V^2rms indicates that the bushing has worn between approximately 0.0035 inches and 0.0045 inches. Evidently, more data is necessary so that the level of confidence when predicting bushing wear can be increased. Nonetheless, the data does suggest a direct relationship between bushing wear and band power.

7.2 Large Dimple Testing

Planet gear bushing wear testing was also conducted to examine the effect of bushing dimple geometry on vibration signatures. As evidenced by the plots in Figures 39, 40, and Appendix

J, results showed that altering the bushing dimple geometry does not shift the resulting frequency bands nor (consistently) alter the amplitudes. Furthermore, no consistent relationships were observed in the band power versus wear plots of bushings with regular dimples and those with large dimples (Figure 41 and Appendix K). In future bushing wear studies, it may be desirable to complete additional tests to examine the effect of bushing dimple geometry on the vibration signature.

8.0 Recommendations for Future Work

The results of this study indicate that vibration signatures gathered from the BT are indicative of LAV planet gear bushing wear. This investigation was conducted as a feasibility assessment; therefore additional work is requried before this wear detection method can be implemented on an actual LAV. Labeling the current study as "Phase I" of LAV bushing wear detection, recommendations for Phases II and III are discussed below.

8.1 Phase II: Dynamometer Testing

As an intermediate step between BT testing and actual "on road" testing of the vehicle, it is recommended that a similar study in which bushing wear is analyzed using vibration signatures via dynamometer testing be conducted. Testing on the dynamometer is an excellent way to verify the results of this study since the entire planetary assembly is tested rather than one single bushing. If this secondary study were to be proven successful, the final step of bushing wear analysis on an operating LAV could be pursued (Phase III, below).

8.1.1 Anticipated Challenges

Data analysis of tests conducted on the dynamometer would be more challenging since additional signatures from planetary components other than the bushings would be present. It would be necessary to recognize and isolate these signatures. Perhaps it would be best to filter out these additional signatures where possible. Additionally, due to the physical contraints of the planetary system, it would not be possible to locate the accelerometers as close to the bushings as they were in this study. This would add complications in recognizing the wear signal.

8.1.2 Additional Considerations

Although the added components from testing on the dynamometer would likely conceal significant signatures in extraneous vibration frequencies, gear chatter as result of lost tolerances could help identify bushing wear. As the acetal layer of the bushing diminishes, there becomes more "play" between the inner-diameter of the gears and their respective pins. This tolerance could result in additional gear chatter, which may manifest itself in the vibration signature of the system. If so, it is likely that this signature could be used to indicate bushing wear.

8.2 Phase III: On Road Testing

As a final phase of LAV bushing wear detection, it is recommended that the project be scaled up to on road testing of the vehicle. This, of course, is contingent upon the success of Phase II. On road testing would be the final necessary step to complete the bushing wear detection study.

8.2.1 Anticipated Challenges

On road testing would introduce even more extraneous signatures from the tire on the terrain, the suspension, and other external noise. As with Phase II, these signatures would have to be isolated and filtered out of the usable data. Sensor location would require additional thought in this phase due to all of the rotating parts and possible environmental conditions that an accelerometer could be exposed to. Finally, a method for data transmission and/or on-board data analysis would need to be developed.

9.0 Notes for Future Bushing Wear Studies

This section is directed towards those readers who are interested in continuing bushing wear analysis via vibration signatures with a secondary phase of this project, whether it be as suggested in Section 8.0 or not. This supplemental information is provided here to guide and assist future researchers of this topic. It is also intended for readers interested in reproducing these results.

9.1 Cracked Block

The first point that should be noted is a previous problem that was encountered with the bushing block. After the first few weeks of testing, the preliminary data analysis showed very poor correlation plots of band power of specific frequency bands versus radial bushing wear. Shortly thereafter, bushings were wearing in a strange pattern. Rather than wearing a full strip across the height of the bushing (Figure 23a), only a portion of the bushing height would be worn. This was indicative of the load being applied at a point that was off-center on the bushing block. After an investigation of the BT, it was noticed that the bushing block had cracked. The crack started at the thermocouple well and then propagated upwards through the top of the bushing block (Figure 44).

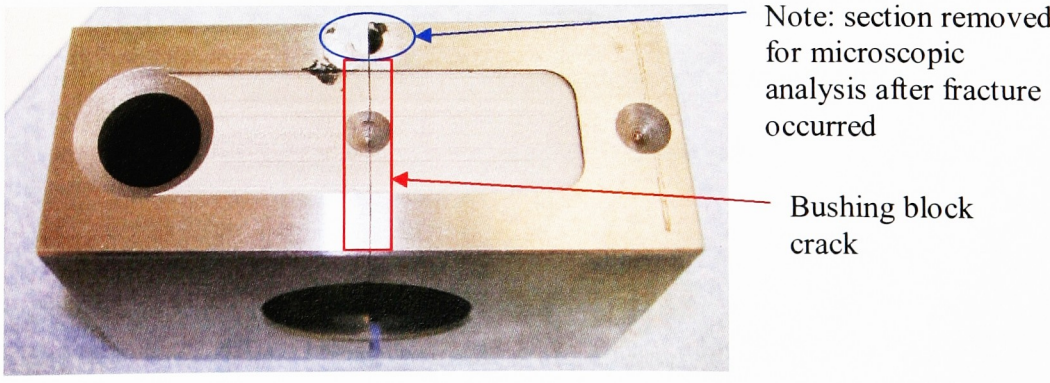

Figure 44. Bushing Block Crack

Since the crack was on a vital component and would therefore adversely affect the vibration signature of the system, the bushing block was replaced. Testing with the new block produced the results that were previously discussed in this paper.

9.2 Worn Ball Bearings

Another important point to note is that the radial ball bearings that support the rotating pin do wear and require replacement on occasion. The exact lifespan of the bearings is unknown since experience shows that it varies greatly from bearing to bearing. One clear indication that the bearings need to be replaced is fretting. Fretting is manifested by a "rust" colored residue on the inner race of the bearing and on the surface of the pin in a localized area near the fretted bearing. A second indication of bearing wear is uneven bushing wear as described in Section 9.1. A worn bearing can cause the pin to tip to a slight angle off of the horizontal datum, thus causing uneven bushing wear.

As expected, a newly replaced ball bearing has a different signature than one that has been significantly used. This was noticed after a new set of replacement ball bearings was installed. Figures 45 and 46 illustrate this difference in vibration signature that results from "old" versus "new" ball bearings. The change in signature that results adds variability to data analysis. Therefore, whenever a new set of bearings is installed in the BT, a new set of baseline data should be acquired after an appropriate bearing break-in period.

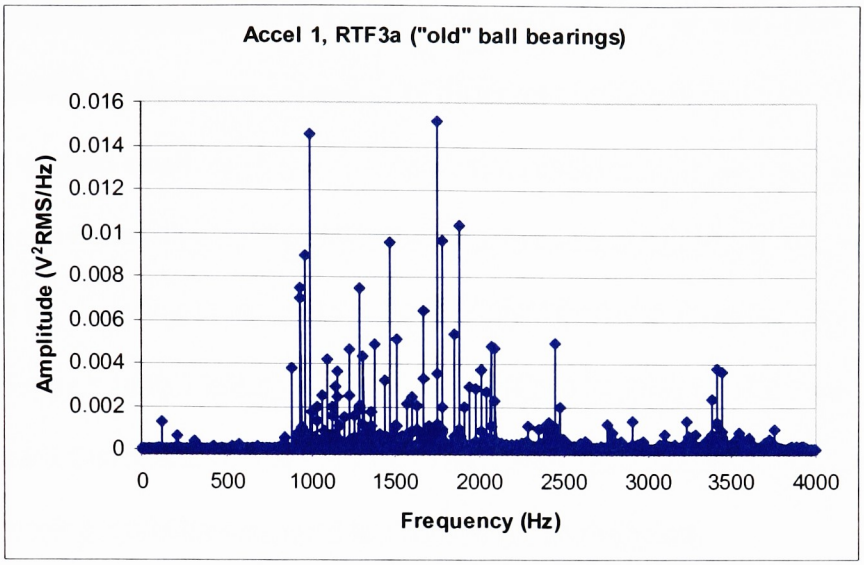

Figure 45. "Old" ball bearing frequency signatures

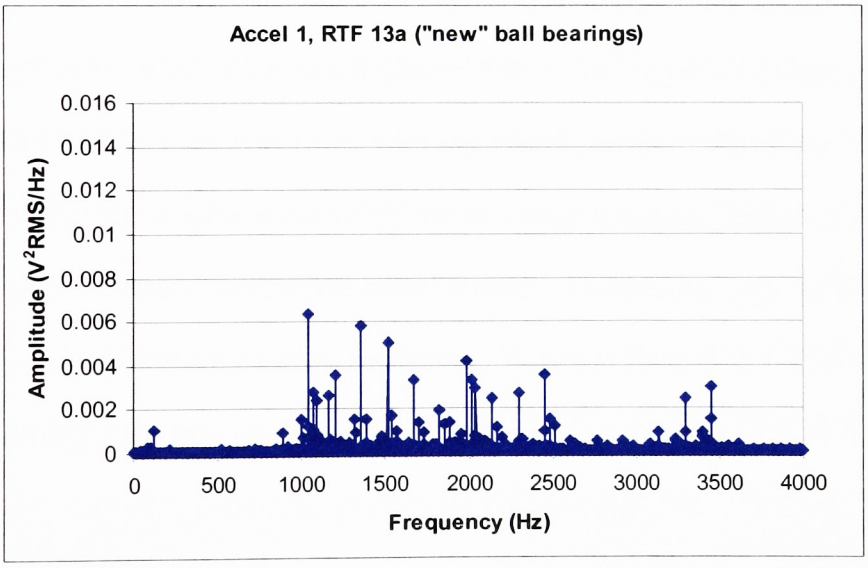

Figure 46. "New" ball bearing frequency signatures

9.2.1 Issues with Replacing Ball Bearings

Another problem was encountered during this study when the ball bearings were replaced after RTF testing. The ordered bearings had a smaller inner diameter than the current

bearings. Paperwork was checked to assure the proper part number was ordered and received. Several bearings were ordered from different vendors, but all had an inner diameter that was too small for the pins. The vendors could not explain the reasoning for this sudden change in dimension, so the only solution was to decrease the pin diameter. Ten pins were sent to a local tooling company to remove 0.001'' from the diameter. Once the pins were returned, large dimple testing was conducted. Since both the ball bearings and pins had changed, a new set of baseline data (with new bushings) was collected so that results from large dimple testing could be compared to this new baseline dataset.

9.3 Intermittent RTF Testing

A group of RTF tests were completed where the test was stopped midway, allowed to completely cool to room temperature, and then restarted. This type of testing closely simulates actual LAV operation since, as with any vehicle, several "starts" and "stops" are quite common. However, allowing the RTF test to cool to room temperature part-way through the test resulted in data analysis complications. The bushings appeared to experience another break-in stage when the test was restarted. This is evidenced by the sudden decrease in band power amplitude after re-start as illustrated in Figure 47. Therefore, it was decided that all RTF tests would be completed from start to finish without interruption.

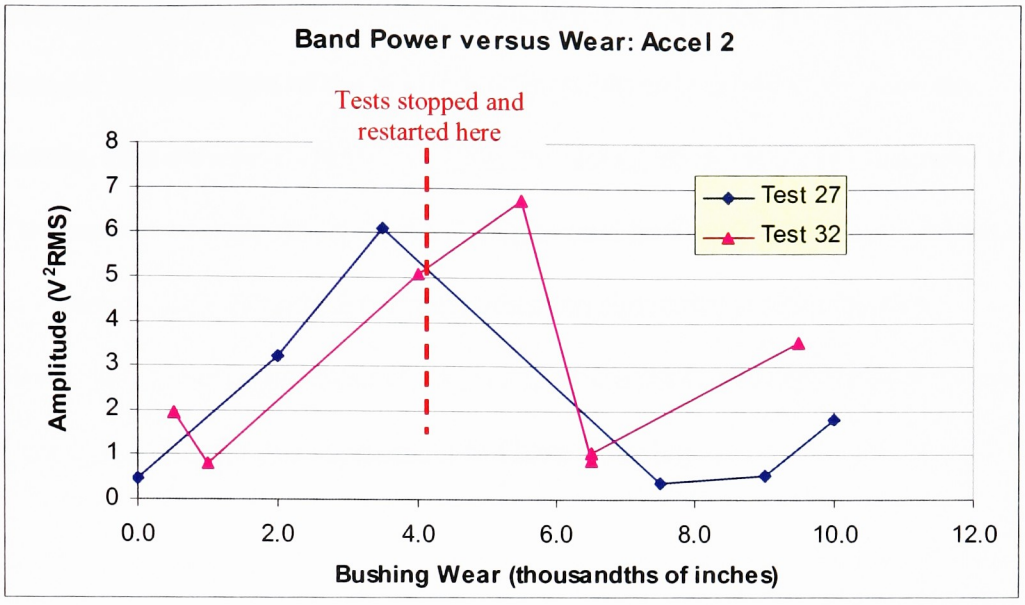

Figure 47. Effect of Stopping at Restarting an RTF Test

It may be worthwhile to examine bushing wear with several "vehicle" starts and stops in between a single test in future generations of this bushing wear study as this most closely simulates actual LAV operation.

9.4 Uneven Bushing Wear

Several BT problems such as the cracked bushing block and worn radial ball bearings (Sections 9.1 and 9.2, respectively) resulted in uneven bushing wear (Figures 48a and 48b).

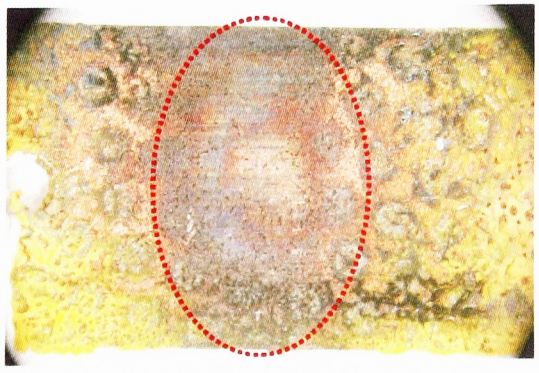

Figure 48a. Photo of even bushing wear

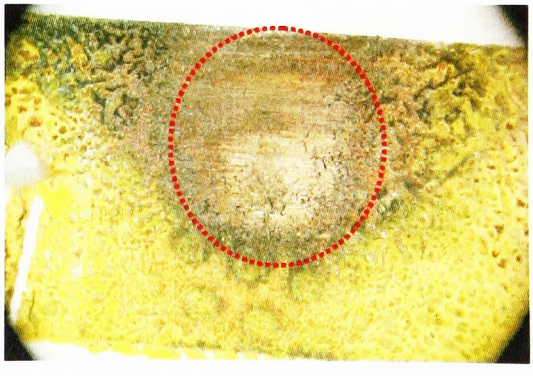

Figure 48b. Photo of uneven bushing wear

The large dimple testing (and the baseline testing that accompanied it) outlined in Table 5 and Section 6.7 showed eight of the twelve bushings that were tested wore unevenly. Unfortunately, after extensive efforts by the author and CIMS personnel to diagnose the cause of the uneven bushing wear, no direct cause could be found. Therefore, understanding the effect of dimple geometry on the system vibration signatures requires further investigation. It may be best to examine this area of interest on the entire planetary assembly tested in the dynamometer as a supplement to Phase II testing.

References

[1] "Aliasing and Sampling at Frequencies above the Nyquist Frequency." NI Developer Zone: Development Library (2005): 13 pars. 21 November 2005 <http://zone.ni.com/devzone/conceptd.nsf/ webmain/7C24348B34500BA386256F2C00628667>

[2] "Auto Power Spectrum." LabVIEW 7.1 Help Manual. Ni.com. 2005. National Instruments.

[3] Boedo, Stephen. Personal communication with the author. 16 February 2006.

[4] Cavacece, Massimo, and Alberto Introini. "Analysis of Damage of Ball Bearings of Aeronautical Transmission by Auto-Power Spectrum and Cross-Power Spectrum." Journal of Vibration and Acoustics 124 (2002):180-185.

[5] Choy, F. K., S. Huang, J. J. Zakrajsek, R. F. Handschuh, and D.P. Townsend. "Vibration Signature Analysis of a Faulted Gear Transmission System." Prepared for the 30th Joint Propulsion Conference, June 27-29, 1994. 1-14.

[6] Choy, F. K., D. H. Mugler, and J. Zhou. "Damage Identification of a Gear Transmission using Vibration Signatures." Journal of Mechanical Design 125 (2003):394-403.

[7] Choy, F. K., V. Polyshchuk, J. J. Zakrajsek, R. F. Handschuh, and D. P. Townsend. "Analysis of the Effects of Surface Pitting and Wear on the Vibration of a Gear Transmission System." Tribology International 29 (1996):77-83.

[8] Colquitt, Erin. "LAV Planet Gear Bushing Study: Comparison of Alternate Bushings and Lubricants." Microsoft Word® Document on CIMS private network. February 2005. <\\Polaris78\asset health management\LAV Material Aging Prognostic Development\ Planetary\bushing tester\V and A's Work\Summary info (as of 12-24-03)>

[9] Elali, Taan S. Discrete Systems and Digital Signal Processing with MATLAB®. New York: CRC Press LLC, 2004.

[10] Fister, D. and E. Colquitt. "DX, DP, HX synth-petr comparison." Microsoft Excel® Spreadsheet on CIMS private network. October 2004. <\\Polaris78\asset health management\LAV Material Aging Prognostic Development\Planetary\bushing tester\V and A's Work\Summary info (as of 12-24-03)>

[11] Fister, David R. Personal communication with the author. 28 October 2005.

[12] Galler, Don, and Andrew Booth. "The Shocking Truth of Accelerometer Selection." Machine Design 61, 14 (1989):85-89.

[13] GGB Bearing Technology. 2005. 7 June 2005. http://www.glacier-garlock-bearings.com/

[14] Hildick, James F. "Light Armored Vehicle Bushing Material Study." Project with Paper, Lead advisor: Dr. DeBartolo. Rochester Institute of Technology, 2003.

[15] "Introduction to Piezoelectric Accelerometers." Technical Literature: PCB.com. 2005. PCB Piezotronics, Inc.

[16] "Introduction to Piezoelectric Industrial Accelerometers." Technical Literature: PCB.com. 2005. PCB Piezotronics, Inc.

[17] Kacprzynski, Gregory. "A Novel Test Bed and Stochastic Vibration Diagnostics for Assessing the Condition of Constant Velocity Joints." M.S. Thesis. Rochester Institute of Technology, 2002.

[18] Kempski, M. and K. Kochersberger. Personal communication with the author. 3 August 2005.

[19] Kochersberger, K. Personal communication with the author. 23 March 2005.

[20] Liberatore, S. and G.P. Carman. "Power Spectral Density Analysis for Damage Identification and Location." Journal of Sound and Vibration 274 (2004):761-776

[21] "Light Armored Vehicle-25 (LAV-25)." FAS.org. 2000. FAS Military Analysis Network. 11 May 2005 <http://www.fas.org/man/dod-101/sys/land/lav-25.htm>

[22] "Light Armored Vehicle (LAV)." GlobalSecurity.org. 2005. 11 May 2005 <http://www.globalsecurity.org/military/systems/ground/lav.htm>

[23] Office of Naval Research Grant No. N0014-39-1-0154 Final Report, 1998-2003. National Center for Remanufacturing and Resource Recovery, 2004.

[24] Parnell, Victoria. "Planetary Bushing Tester Procedure Handbook." Microsoft Word® Document on CIMS private network. July 2005. <\\Polaris78\asset health management\LAV Material Aging Prognostic Development\Planetary\bushing tester\ V and A's Work\Bushing Tester Handbook (new load system as of 12-23-04)>

[25] Peng, Z. and Kessissoglou, N. "An Integrated Approach to Fault Diagnosis of Machinery using Wear Debris Analysis and Vibration Analysis." Wear 255 (2003):1221-1232

[26] "Power Spectrum." LabVIEW 7.1 Help Manual. Ni.com. 2005. National Instruments.

[27] Studley, A., V. Parnell, and K. Mather. "Dynamometer-Bushing Tester Correlation Study." Microsoft PowerPoint® Presentation on CIMS private network. May 2004. <\\Polaris78\asset health management\LAV Material Aging Prognostic Development\ Planetary\Dyno-Bushing Tester Comparison\10 min Correlation Presentation>

[28] Studley, A., V. Parnell, and K. Mather. "Dyno-bushing tester Comparison." Microsoft Word® Document on CIMS private network. May 2004. <\\Polaris78\asset health management\LAV Material Aging Prognostic Development\Planetary\Dyno-Bushing Tester Comparison\Dyno-bushing Comparison Report>

[29] "Test 25." Bushing wear data on CIMS private network. January, 2004. <\\Polaris78\ asset health management\LAV Material Aging Prognostic Development\Planetary\ bushing tester\V and A's Work\Raw Data (as of 12-24-03)\1-19-04, test 25>

[30] "The Fundamentals of Signal Analysis, Application Note 243." Agilent.com. Agilent Technologies 2000 <http://cpliterature.product.agilent.com/litweb/pdf/5952-8898E.pdf>

[31] Thomson, William T. and Marie Dillon Dahleh. Theory of Vibration with Applications, Fifth Edition. New Jersey: Prentice Hall, 1998.

[32] United States Marine Corps Department of the Navy. U.S. Marine Corps Technical Manual: Operator's Manual Light Armored Vehicle LAV-25 Automotive Hull. Washington D.C: Department of the Navy, 2000.

[33] "Using Fast Fourier Transforms and Power Spectra in LabVIEW." NI Developer Zone: Development Library (2005): NI.com. 25 January 2006. http://zone.ni.com/ devzone/ conceptd.nsf/webmain/cc9733cb28b14ea5862568650060daa2?OpenDocument

[34] Wilson, Jon. "A Practical Approach to Vibration Detection and Measurement; Part 2: Dynamic and Environmental Effects on Performance." Sensors Online (1999): 44 pars. March 1999 <http://www. sensorsmag.com/articles/0399/0399_52/main.shtml>

[35] Wilson, Jon. "A Practical Approach to Vibration Detection and Measurement; Part 3: Installation, Recalibration, and Application." Sensors Online (1999): 42 pars. 10 August 2005 <http://www.sensorsmag.com/articles/ 0499/0499_46/main.shtml>

[36] Xu, Ming. "Accelerometer Selection to Avoid Saturation in Vibration Measurements." Sound and Vibration 34, 11 (2000):22-26.

[37] Yen, Gary G., and Kuo-Chung Lin. "Conditional Health Monitoring using Vibration Signatures." Proceedings of the 38th Conference on Decision & Control. 1999. 4493-4498.

[38] "8774A50, 8776A50 Series Ceramic Shear Accelerometers." Kistler.com. Kistler Instrument Corporation. 15 August 2005. <http://www.kistler.com/mediaaccess/en/ 000-255e-10.02.pdf>

Appendix A – Torque-speed Calculations

	ENGINE Performance Specifications			Transmission Output			Transfer Case Output			Differential Output			Planetary Input (Sun Gear Input)		Planetary Output			LAV Speed	"P" Pin Loads	"V" Bushing Speed wrt Carrier		Bushing Projected Area	Bushing PV
Gear	Torque (ft-lbs)	RPM	HP (calc)	Gear Ratio	Torque (ft-lbs)	Speed (RPM)	Torque (ft-lbs)	Speed (RPM)	HP (calc)	Torque (ft-lbs)	Speed (RPM)	HP (calc)	Torque (ft-lbs)	Speed (RPM)	Torque (ft-lbs)	Speed (RPM)	HP (calc)	(MPH)	(lbs/pin)	(RPM)	(fpm)	(in2)	(psi-fpm)
1	627	1600	191	8.05	5047	199	2916	344	191	3252	154	96	1626	154	6162	41	48	4	8646	135	35	1.189	252759
	613	1800	210	8.05	4935	224	2851	387	210	3179	174	105	1590	174	6024	46	53	5	8453	152	39	1.189	278004
	600	2000	229	8.05	4830	248	2791	430	229	3112	193	114	1556	193	5897	51	57	5	8274	169	43	1.189	302343
	580	2200	243	8.05	4669	273	2698	473	243	3008	212	122	1504	212	5700	56	61	6	7998	185	48	1.189	321491
	560	2400	256	8.05	4508	298	2605	516	256	2904	231	128	1452	231	5504	61	64	7	7723	202	52	1.189	338624
	535	2600	265	8.05	4307	323	2488	559	265	2775	251	132	1387	251	5258	66	66	7	7378	219	56	1.189	350466
	525	2700	270	8.05	4226	335	2442	580	270	2723	260	135	1361	260	5160	69	68	7	7240	228	59	1.189	357143
	516	2800	275	8.05	4154	348	2400	602	275	2676	270	138	1338	270	5071	71	69	8	7116	236	61	1.189	364021
2	627	1600	191	3.58	2245	447	1297	773	191	1446	347	96	723	347	2740	92	48	10	3845	303	78	1.189	252759
	613	1800	210	3.58	2195	503	1268	870	210	1414	390	105	707	390	2679	103	53	11	3759	341	88	1.189	278004
	600	2000	229	3.58	2148	559	1241	967	229	1384	434	114	692	434	2622	114	57	12	3680	379	98	1.189	302343
	580	2200	243	3.58	2076	615	1200	1064	243	1338	477	122	669	477	2535	126	61	13	3557	417	107	1.189	321491
	560	2400	256	3.58	2005	670	1158	1160	256	1292	520	128	646	520	2448	137	64	15	3434	455	117	1.189	338624
	535	2600	265	3.58	1915	726	1107	1257	265	1234	564	132	617	564	2338	149	66	16	3281	493	127	1.189	350466
	525	2700	270	3.58	1880	754	1086	1305	270	1211	585	135	605	585	2295	154	68	17	3220	512	132	1.189	357143
	516	2800	275	3.58	1847	782	1067	1354	275	1190	607	138	595	607	2255	160	69	17	3165	531	137	1.189	364021
3	627	1600	191	2.09	1310	766	757	1325	191	844	594	96	422	594	1600	157	48	17	2245	519	134	1.189	252759
	613	1800	210	2.09	1281	861	740	1491	210	825	668	105	413	668	1564	176	53	19	2195	584	151	1.189	278004
	600	2000	229	2.09	1254	957	725	1656	229	808	743	114	404	743	1531	196	57	21	2148	649	167	1.189	302343
	580	2200	243	2.09	1212	1053	700	1822	243	781	817	122	390	817	1480	216	61	23	2077	714	184	1.189	321491
	560	2400	256	2.09	1170	1148	676	1987	256	754	891	128	377	891	1429	235	64	25	2005	779	201	1.189	338624
	535	2600	265	2.09	1118	1244	646	2153	265	720	965	132	360	965	1365	255	66	27	1915	844	218	1.189	350466
	525	2700	270	2.09	1097	1292	634	2236	270	707	1003	135	353	1003	1340	265	68	28	1880	876	226	1.189	357143
	516	2800	275	2.09	1078	1340	623	2319	275	695	1040	138	347	1040	1317	274	69	29	1847	909	234	1.189	364021
4	627	1600	191	1.39	872	1151	504	1992	191	561	893	96	281	893	1064	236	48	25	1493	781	201	1.189	252759
	613	1800	210	1.39	852	1295	492	2241	210	549	1005	105	274	1005	1040	265	53	28	1460	878	226	1.189	278004
	600	2000	229	1.39	834	1439	482	2490	229	537	1117	114	269	1117	1018	295	57	32	1429	976	252	1.189	302343
	580	2200	243	1.39	806	1583	466	2739	243	519	1228	122	260	1228	984	324	61	35	1381	1074	277	1.189	321491
	560	2400	256	1.39	778	1727	450	2988	256	501	1340	128	251	1340	950	354	64	38	1333	1171	302	1.189	338624
	535	2600	265	1.39	744	1871	430	3237	265	479	1452	132	240	1452	908	383	66	41	1274	1269	327	1.189	350466
	525	2700	270	1.39	730	1942	422	3362	270	470	1508	135	235	1508	891	398	68	43	1250	1318	340	1.189	357143
	516	2800	275	1.39	717	2014	414	3486	275	462	1563	138	231	1563	876	412	69	44	1229	1366	352	1.189	364021
5	627	1600	191	1	627	1600	362	2769	191	404	1242	96	202	1242	765	328	48	35	1074	1085	280	1.189	252759
	613	1800	210	1	613	1800	354	3115	210	395	1397	105	197	1397	748	369	53	39	1050	1221	315	1.189	278004
	600	2000	229	1	600	2000	347	3461	229	387	1552	114	193	1552	733	410	57	44	1028	1357	350	1.189	302343
	580	2200	243	1	580	2200	335	3808	243	374	1707	122	187	1707	708	451	61	48	994	1492	385	1.189	321491
	560	2400	256	1	560	2400	324	4154	256	361	1863	128	180	1863	684	491	64	53	959	1628	420	1.189	338624
	535	2600	265	1	535	2600	309	4500	265	345	2018	132	172	2018	653	532	66	57	916	1764	455	1.189	350466
	525	2700	270	1	525	2700	303	4673	270	338	2095	135	169	2095	641	553	68	59	899	1831	472	1.189	357143
	516	2800	275	1	516	2800	298	4846	275	332	2173	138	166	2173	630	573	69	61	884	1899	490	1.189	364021

Appendix B – Explanation of NA4*, and NB4* (quoted from [5])

NA4*[4,20,21] is a general fault detection parameter with trending capabilities. A residual signal is constructed by removing regular meshing components from the time averaged signal. For NA4, the first order sidebands stay in the residual signal and the fourth statistical moment of the residual signal is then divided by the averaged variance of the residual signal, raised to the second power. The average variance is the mean value of the variance of all previous records in the run ensemble. This allows NA4 to compare the current gear vibration with the baseline of the system under nominal conditions. NA4 is given by the quasi-normalized kurtosis equation shown below:

$$NA4^*(M) = \frac{N\sum_{i=1}^{N}(r_i - \bar{r})^4}{\left\{\frac{1}{M}\sum_{j=1}^{N}\left[\sum_{i=1}^{N}(r_{ij} - \bar{r}_j)^2\right]\right\}^2} \qquad (4)$$

where

- r = residual signal
- $\bar{r}$ = mean value of residual signal
- N = total number of data points in one time record
- i = data point number in time record
- j = time record number
- M = current time record number in run ensemble

An enhancement to this parameter is given by NA4*, in which the value of the averaged variance is "locked" when the instantaneous variance exceeds a pre-determined value.[4] This provides NA4 with enhanced trending capabilities, in which the kurtosis of the current signal is compared to the variance of the locked baseline signal under nominal conditions.

NB4 is another parameter similar to NA4 that also uses the quasi-normalized kurtosis given in equation (4). The major difference is that instead of using a residual signal, NB4 uses the envelope of the signal banpassed about the mesh frequency. Again, as with NA4*, NB4* is an enhancement to the NB4 parameter, in which the value of the average variance is "locked" when the instantaneous variance exceeds a pre-determined value. The equation for NB4* is given below:

$$NB4^*(M) = \frac{N\sum_{i=1}^{N}(s_i - \bar{s})^4}{\left\{\frac{1}{M}\sum_{j=1}^{N}\left[\sum_{i=1}^{N}(s_{ij} - \bar{s}_j)^2\right]\right\}^2} \qquad (5)$$

and

$$s(t) = \text{magnitude of } \{b(t) + i\,\{H[b(t)]\}\} \qquad (6)$$

where

- $b(t)$ = time averaged signal bandpassed filtered about the meshing frequency
- $H[b(t)]$ = the Hilbert Transform of $b(t)$
- N = total number of data points in one time record
- i = data point number in time record
- j = time record number
- M = current time record number in run ensemble

Appendix C– Accelerometer Selection Literature Review

C.1 Amplitude Range and Sensitivity. "The peak amplitude range of an accelerometer is inversely proportional to its sensitivity" [36]. Therefore, when the amplitude range of an accelerometer is increased, it is done so at the cost of decreased sensitivity. These two characteristics must be appropriately balanced when selecting an accelerometer. The typical sensitivity of an industrial, general-purpose accelerometer is 100 mV/g [36]. The specified amplitude range of an accelerometer should not be exceeded since this could cause permanent damage to the sensor [12]. Many external objects can affect an accelerometer's amplitude range and sensitivity such as connected cables, amplifiers, and mounting style [34].

C.2 Frequency Response. The Frequency response of an accelerometer is "the frequency range over which accurate output signals are generated" [12]. Frequency response should not be underestimated; according to Galler and Booth [12], it is the most important criterion to consider when choosing an accelerometer. Physical characteristics of the accelerometer such as stiffness determine the upper end of the frequency response while the amplifier roll-off and the discharge time constant control the low frequency range [16]. Since the system of interest is mechanical, the vibration signature frequencies should be relatively low. Therefore, it is expected that a typical accelerometer frequency response range of 1 Hz to 10 kHz is adequate [19].

C.3 Operating Environment. When selecting an accelerometer, it is important to consider where it will be operating since environmental factors such as temperature, material contamiation, and ambient noise can have substantial effects on measurement accuracy [34].

C.3.1 Temperature. Temperature, for example, can affect an accelerometers performance [12]. Accelerometer temperature stability is rated in two ways: thermal zero shift and thermal gain shift [12]. Thermal zero shift is the change in accelerometer output due to a change in temperature when no acceleration is applied while thermal gain shift is an adjustment in accelerometer sensitivity as a result of a temperature change [12]. These values are typically listed in an accelerometer's specification sheet. Galler and Booth state that "Piezoelectric accelerometers with separate charge amplifiers have the widest temperature ranges" [12]. Operating in an environment whose temperature is outside of the specified temperature range should be avoided as this can result in permanent damage to the sensor [34]. The specified maximum operating temperature will be vital when choosing an accelerometer for this application since the system is heated. However, typical bushing wear tests in the past have had a relatively stable operating temperature, so sensitivity to temperature should not be a central issue when selecting an appropriate accelerometer.

C.3.2 Material Contamination. Possible contaminants that exist in the operating environment of the accelerometer must be considered. Moisture, dirt, oil, and other chemicals are a few possible contaminants [15]. It is recommended to use accelerometers that are made of 316L stainless steel and hermetic-style connectors when operating in harsh environments [16]. Other recommendations for sensor protection include using heat-

shrinkable tubing, RTV sealant, or silicone grease on all cable connections [15]. Finally, the sensor, cabling, and connector material specifications should be checked to ensure that they are suitable for the operating environment [16].

C.3.3 Ambient Noise. External noise can be transmitted through the signal when the accelerometer is mounted to an electrically conductive material [15]. "Noise from other electrical equipment and machines that are grounded to the structure, such as motors, pumps, and generators, can enter the ground path of the measurement signal through the base of a standard accelerometer," [15]. Therefore, it is recommended to electrically isolate the accelerometer from the test specimen to avoid ground noise and ground loops [15].

C.4 Mounting. Adhesive mounting, stud mounting, magnetic mounting, and probe tips are the four main methods used to fasten accelerometers to the appropriate vibration examination site [16]. The effect that the mounting method has on the frequency response of the accelerometer should be taken into account when choosing a technique [15]. Along with a loss of frequency response, poor mounting can also result in increased noise [36]. Of all the mounting options, stud mounting is the most secure and therefore results in the most true frequency response [16]. However, one point of caution to consider when using the stud mount option is base strain. An accelerometer that is screwed down too tightly can strain the mounting surface [34]. This strain can be transmitted to the accelerometer housing and distort the signal [34]. Typically, accelerometers have specifications on base strain sensitivity as well as torque (for stud mounting application) that should be carefully

followed. When stud mounting an accelerometer, it is also important to avoid bottoming out of the screw [15, 35].

Every mounting technique other than the stud option introduces a mounted resonance that "is lower than the natural resonance of the sensor and reduces the upper frequency range. The farther the sensor is removed from the measurement point, the lower the mounted resonance and the lower the usable frequency range" [16]. This change in mounted resonance is illustrated below in Figure C-1.

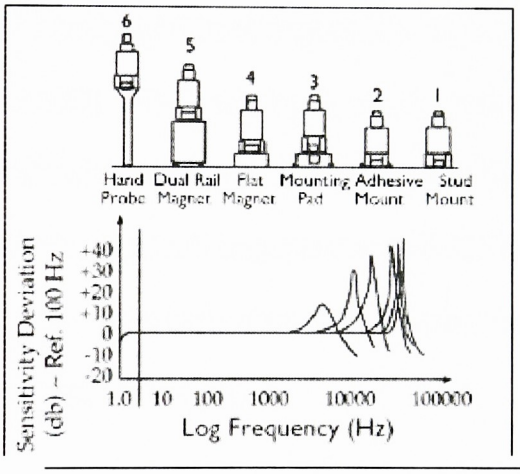

Figure C-1. Effect of mounting technique on resonance [16]

Adhesive mounting is common in miniature accelerometers used for temporary testing [35]. Several different adhesive types are commercially available; they vary according to environmental temperature, desired duration of mount, and surface finish [15]. Temporary adhesives such as Petro Wax tend to be lower in stiffness and therefore limit the accelerometer's frequency range much more than a permanent adhesive with increased rigidity would [15]. Typically, these temporary adhesives should be used for frequencies that are less than 500 Hz [15]. It is important to keep in mind that as the number of adhesive joints between the accelerometer and test specimen increase, the signal transmissibility

decreases [35]. Surface finish and adhesive thickness can also adversely affect the accelerometer's operating capabilities. "Generally, as surface irregularities or the thickness of the adhesive increase, the usable frequency range decreases," [15]. Finally, certain adhesives can result in cosmetic or physical damage to material surfaces. Therefore, if this is an area of concern, adhesives should be tested before being applied [15].

Magnetic mounting is another convenient, temporary attachment option. Stronger magnets result in better responses at high frequencies [15]. It is important to consider the weight of the magnet with respect to the weight of the test specimen. Typically, magnets are used for low frequency measurements [35]. The reasoning for this is shown in Figure 10 above where the flat magnet mounting method (option "4") shows large sensitivity deviations at frequencies greater than 10 kHz. Dual rail magnets are available for mounting on curved surfaces; although they should only be used when absolutely necessary as they considerably reduce the accelerometer's frequency range [15].

Mounting blocks are available for use where data is desired from more than one axis. Their use, however, should be limited since they act as a spring-mass system that reduces the frequency response of the accelerometer [35]. It should be noted that when mounting blocks are used, the measurements reflect the motion of the block itself, which may or may not accurately correspond to the motion of the test specimen [35]. For this reason, mounting blocks should "be kept as small, lightweight, and stiff as possible," [35]. Regardless which mounting technique is chosen, the surface of the object must be appropriately prepared to maximize signal transmission.

C.4.1 Surface Preparation. The surface where the accelerometer is to be attached should be smooth and flat [15]. Typically, a surface finish specification is supplied in the accelerometer instruction manual. The mounting surface must also be thoroughly cleaned [16]. Finally, a lubricant should be applied to the mounting surface. This fills voids and therefore increases the stiffness (in compression) of the bond site [35]. Common lubricants include bee's wax, machine oil, and silicone grease [16]. "This coating aids in the transmissibility of the higher frequency vibrations and improves high frequency response of sensors" [16]. It is particularly important to use a lubricant when recording frequencies above 1000 Hz [35].

8774A50, 8776A50 SERIES CERAMIC SHEAR ACCELEROMETERS

The 8774A50, 8776A50 series are low impedance, voltage mode accelerometers designed for vibration measurement in single or multichannel applications. The unique connector design is rugged and maintains excellent integrity with repeated connections. The ceramic sensing element components are carefully designed to provide the level of performance most often required in general purpose vibration measurements. Kistler's shear technology assures high immunity to base strain, thermal transients and transverse accelerations. Other outstanding features include high frequency response, lightweight and hermetic sealing.

Continued

- Low impedance, voltage mode
- Ceramic Shear sensing element
- High sensitivity, high resolution
- Low transverse sensitivity
- Rugged connector for repeated connections
- Priced for OEM or low cost/channel applications
- Conforming to CE

8774A50 8776A50, M1, M3 8776A50M6

Technical Data	Units	8774A50	8776A50, M1	8776A50M3	8776A50M6
Acceleration Range	*g*	±50	±50	±50	±50
Acceleration Limit	g_{pk}	±500	±500	±500	±500
Threshold nom.	g_{rms}	0.0025	0.0025	0.0025	0.0025
Sensitivity 5%, +30% (5%, +35% for M1)	mV/*g*	100	100	100	100
Resonant Frequency mounted, nom.	kHz	44	38 (1)	38 (1)	40 (1)
Frequency Response ± 5%	Hz	1...10000	1 ... 7000 (1)	0.5 ... 4000 (1)	1...10000
Phase Shift 4 ... 2000 Hz	degree	<5	<5	<5	<5
Amplitude Non-linearity	%FSO	≤1	≤1	≤1	≤1
Time Constant	s	≥0.5	≥0.5	≥1.0	≥0.5
Transverse Sensitivity typ., (max.)	%	1.5 (5)	1.5 (5)	3 (5)	1.5 (5)
Environmental:					
Base Strain Sensitivity @ 250 µε	µ*g*/µε	0.002	0.0005 (1)	0.001 (1)	0.002
8776A50M1	*g*/µε	–	0.001 (1)	–	–
Shock Limit (1ms pulse width) max.	*g* pk		5000		
Temperature Coefficient of Sensitivity	%/°F		–0.08		
	%/°C		–0.14		
Temperature Range Operating (4 mA supply current)	°F (°C)		–65...250 (–55...120)		
Output:					
Bias nom.	VDC		11		
Impedance	Ω		100		
Voltage full scale	V		±5		
Current	mA		2		
Source:					
Voltage	VDC		20 ... 30		
Constant Current	mA		2 ... 20		
Impedance min.	kΩ		>100		
Construction:					
Sensing Element	type		ceramic/shear		
Housing/ Base	material		titanium		
Sealing housing/ connector	type		hermetic		
Connector	type		10-32 neg		
Ground Isolation (8776A50 not GND. isolated)	MΩ	–	10	10	–
Weight	grams	4.0	4.3	4.3	4.5
Mounting Torque (8774A50, 8776A50M6)	lbf in (Nm)	18 (2)	wax/adhesive	wax/adhesive	18 (2)

(1) wax mounted

1 *g* = 9.80665 m/s², 1 inch = 25.4 mm, 1 gram = 0.03527 oz, 1 lbf in = 0.1129 Nm

Kistler Instrument Corporation, 75 John Glenn Drive, Amherst NY 14228
Phone 716-691-5100, Fax 716-691-5226, e-mail: sales.us@kistlercom, www.kistlercom

A low impedance, voltage output is provided by the internal electronic impedance converter. This output allows for the use of an inexpensive coaxial cable, while providing high noise immunity and insensitivity to cable motion. Power this accelerometer with one of Kistler's couplers, signal conditioners or from any voltage mode piezoelectric sensor supply.

Applications

Types 8774A and 8776A are multipurpose accelerometers, useful for many applications. These accelerometers provide 2.5 milli-g resolution suitable for use in low level measurement applications. The wide bandwidth and rugged construction are ideal for impact and vibration related applications including condition monitoring and vehicle testing. These sensors offer excellent performance and cost advantages for demanding applications. Contact Kistler for OEM and quantity discounts.

Related Products

8284A30 high impedance, charge mode, –33pC/*g*
8286A30 high impedance, charge mode, –33pC/*g*
8290A25 high impedance, charge mode, triaxial, –25pC/*g*
8784A50 low impedance, voltage mode, 5 *g*, 1000mV/*g*
8786A50 low impedance, voltage mode, 5 *g*, 1000mV/*g*

Ordering Information

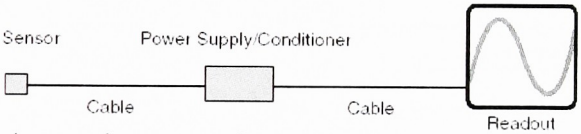

Specify:

1 - 8774A50 top connector accelerometer, stud mounting or
8776A50 side connector accelerometer adhesive mounting or
8776A50M1 side connector accelerometer, ground isolated, adhesive mounting or
8776A50M3 side connector accelerometer with phase matching, adhesive mounting and ground isolated or
8776A50M6 side connector accelerometer, stud mounting
2 - 1761B... sensor cable, 10-32 pos. to BNC pos., specify length in meters
3 - 5100 series coupler or dual mode amplifier
4 - 1511... output cable, BNC pos. to BNC pos., specify

Supplied Accessory

8432 mounting wax for 8776A50

Optional Accessories

8436 adhesive mounting pad
8452 mounting magnet
8524 mounting cube for 8774A50
8526 cube for adhesive mounting 8776A50

Dimensions in inches [mm]

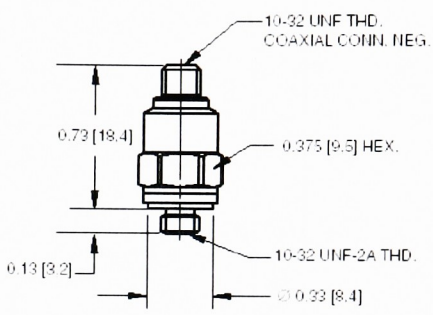

8774A50

Dimensions in inches [mm]

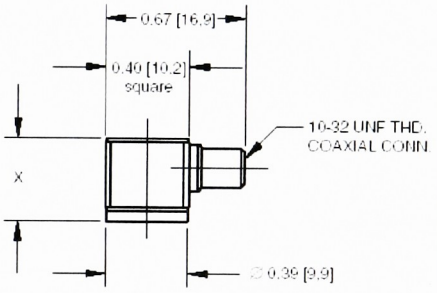

8776A50 X = 0.40 [10.2]
8776A50M1,M3 X = 0.45 [11,4]

Dimensions in inches [mm]

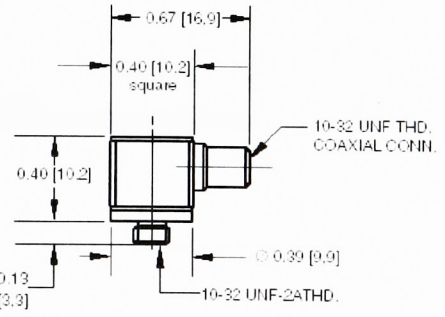

8776A50M6

Kistler Instrument AG Winterthur, Postfach 304, CH-8408 Winterthur
Tel + 41 - 052 - 224 11 11, Fax + 41 - 052 - 224 14 14, sales@kistler.ch, www.kistler.com

Kistler Instrument Corporation, 75 John Glenn Drive, Amherst NY 14228
Phone 716-691-5100, Fax 716-691-5226, e-mail: sales.us@kistler.com, www.kistler.com

Appendix E – Horizontal Accelerometer Data

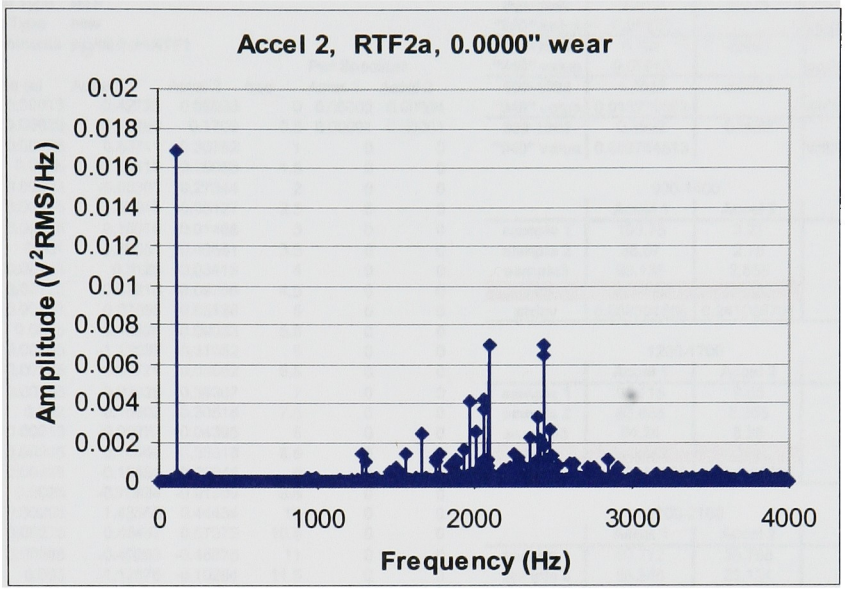

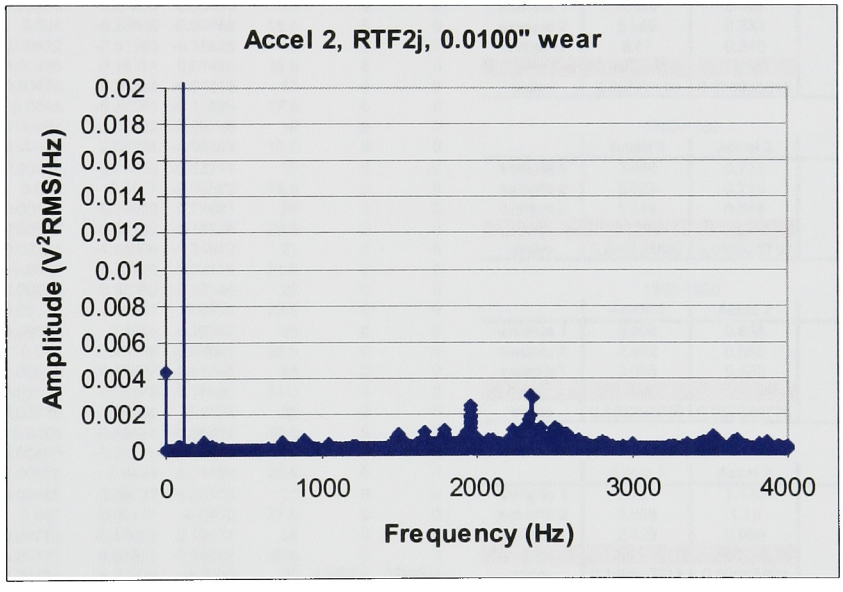

Appendix F – Sample Calculation (1 of 2)

Thesis Testing
Test No. RTF2a
Date 10/14/2005
Test Type RTF
Pin Type new
Comments pin/oil from RTF1

Time (s)	Accel 1	Accel 2	freq	Pwr Spectrum Accel 1	Pwr Spectrum Accel 2
0.00013	-0.42725	0.09033	0	0.00002	0.00004
0.00025	0.18066	0.1709	0.5	0.00001	0.00001
0.00038	0.53711	0.30762	1	0	0
0.0005	-0.03418	0.29053	1.5	0	0
0.00063	-0.08301	0.27344	2	0	0
0.00075	-0.52246	-0.05127	2.5	0	0
0.00088	0.13916	-0.01465	3	0	0
0.001	0.39551	0.49561	3.5	0	0
0.00113	0.3125	-0.03418	4	0	0
0.00125	-0.43213	-0.09766	4.5	0	0
0.00138	0.07568	0.65186	5	0	0
0.0015	0.48828	-0.09033	5.5	0	0
0.00163	-1.13037	-0.31982	6	0	0
0.00175	0.40771	0.03662	6.5	0	0
0.00188	0.23926	0.39307	7	0	0
0.002	0.16602	-0.30518	7.5	0	0
0.00213	-0.00977	-0.04395	8	0	0
0.00225	0.14404	0.38818	8.5	0	0
0.00238	-0.12451	-0.22949	9	0	0
0.0025	-0.79834	-0.91309	9.5	0	0
0.00263	1.43555	0.44434	10	0	0
0.00275	0.43457	0.57373	10.5	0	0
0.00288	-0.40283	-0.46875	11	0	0
0.003	-1.17676	-0.10254	11.5	0	0
0.00313	-0.06836	0.18066	12	0	0
0.00325	0.34912	-0.49072	12.5	0	0
0.00338	0.13916	0.11475	13	0	0
0.0035	0.86182	0.05371	13.5	0	0
0.00363	-0.50049	-0.17334	14	0	0
0.00375	-0.33447	-0.18311	14.5	0	0
0.00388	-0.21973	0.02686	15	0	0
0.004	-0.28809	-0.09766	15.5	0	0
0.00412	-0.01953	-0.15625	16	0	0
0.00425	0.18311	0.01465	16.5	0	0
0.00438	0.20264	-0.07813	17	0	0
0.0045	-0.39551	-0.12695	17.5	0	0
0.00463	-0.03662	-0.09766	18	0	0
0.00475	0.08301	-0.06348	18.5	0	0
0.00488	-0.27832	-0.53711	19	0	0
0.005	0.1001	-0.06592	19.5	0	0
0.00513	0.24658	0.77881	20	0	0
0.00525	-0.86182	-0.78125	20.5	0	0
0.00538	-1.04004	-0.34912	21	0	0
0.0055	0.78125	0.03174	21.5	0	0
0.00563	0.69092	-0.13184	22	0	0
0.00575	0.56641	-0.0708	22.5	0	0
0.00588	-0.1001	0.26367	23	0	0
0.006	-0.45898	-0.02686	23.5	0	0
0.00613	-0.77637	-0.41748	24	0	0
0.00625	-0.21973	0.18066	24.5	0	0
0.00638	0.87646	0.2124	25	0	0
0.0065	-0.13184	-0.28564	25.5	0	0
0.00663	-0.05615	-0.18066	26	0	0
0.00675	0.4834	0.21484	26.5	0	0
0.00688	0.04883	0.22705	27	0	0
0.007	-0.05127	-0.0415	27.5	0	0
0.00713	-0.60059	0.19531	28	0	0
0.00725	0.01953	-0.08789	28.5	0	0
0.00738	0.20508	-0.2002	29	0.00002	0.00002
0.0075	0.28564	0.42725	29.5	0	0
0.00763	0.43213	0.44678	30	0	0.00001
0.00775	-1.19629	-0.64941	30.5	0.00001	0
0.00788	0.57861	-0.04395	31	0	0
0.008	1.03271	1.22314	31.5	0	0
0.00813	-0.24902	-0.52002	32	0	0
0.00825	-1.01807	-0.22949	32.5	0	0
0.00838	-0.48584	0.78857	33	0	0
0.0085	0.48584	-0.10986	33.5	0	0
0.00863	-0.14893	-0.1001	34	0	0
0.00875	0.46631	0.20752	34.5	0	0
0.00888	0.51025	-0.16357	35	0	0
0.009	0.31494	0.39551	35.5	0	0
0.00913	-0.16846	0.16357	36	0	0
0.00925	-0.77393	-0.00977	36.5	0	0
0.00938	-0.29541	-0.2124	37	0	0

	Accel 1	Accel 2	
900-1000	5.196	0.084	
"940" value	0.01213		sample 1
900-1000	4.412	0.071	
"940" value	0.01127		sample 2
900-1000	4.751	0.068	
"940" value	0.01643		sample 3
900-1000	4.7863	0.0743	
"940" value	0.013276667		AVG
900-1000	0.3932	0.0085	
"940" value	0.002764513		STDEV

900-1400

	Accel 1	Accel 2
sample 1	100.75	3.21
sample 2	88.07	2.75
sample3	93.135	2.855
avg	93.9850	2.9383
stdev	6.382591558	0.241056701

1200-1700

	Accel 1	Accel 2
sample 1	94.115	9.68
sample 2	83.865	8.365
sample3	84.24	8.25
avg	87.4067	8.7650
stdev	5.812612006	0.794496696

1700-2100

	Accel 1	Accel 2
sample 1	60.772	23.768
sample 2	55.848	22.124
sample3	53.552	19.784
avg	56.7240	21.8920
stdev	3.688852396	2.00210689

1250-1350

	Accel 1	Accel 2
sample 1	6.504	0.407
sample 2	5.589	0.333
sample3	6.07	0.349
avg	6.0543	0.3630
stdev	0.45770114	0.038935845

1700-1800

	Accel 1	Accel 2
sample 1	3.466	0.775
sample 2	3.027	0.715
sample3	3.044	0.685
avg	3.1790	0.7250
stdev	0.248694592	0.045825757

1800-1900

	Accel 1	Accel 2
sample 1	3.206	0.655
sample 2	2.902	0.555
sample3	3.035	0.563
avg	3.0477	0.5910
stdev	0.152395319	0.055569776

1900-2000

	Accel 1	Accel 2
sample 1	2.721	1.133
sample 2	2.688	1.15
sample3	2.429	0.969
avg	2.6127	1.0840
stdev	0.159913518	0.09995499

2000-2100

	Accel 1	Accel 2
sample 1	5.858	3.395
sample 2	5.37	3.119
sample3	4.882	2.729
avg	5.3700	3.0810
stdev	0.488	0.334622175

2550-2700

	Accel 1	Accel 2
sample 1	1.089	1.482
sample 2	1.062	1.56
sample3	1.0995	1.3965
avg	1.0835	1.4795
stdev	0.019345542	0.081778665

Sample Calculation (2 of 2)

Thesis Testing
Test No. RTF2a
Date 38639
Test Type RTF
Pin Type new
Comments pin/oil fromF

Time (s)	Accel 1	Accel 2	freq	Column E Pwr Spectrum Accel 1	Column F Pwr Spectrum Accel 2
0.00013	-0.42725	0.09033	0	0.00002	0.00004
0.00025	0.18066	0.1709	0.5	0.00001	0.00001
0.00038	0.53711	0.30762	1	0	0
0.0005	-0.03418	0.29053	1.5	0	0
0.00063	-0.08301	0.27344	2	0	0
0.00075	-0.52246	-0.05127	2.5	0	0
0.00088	0.13916	-0.01465	3	0	0
0.001	0.39551	0.49561	3.5	0	0
0.00113	0.3125	-0.03418	4	0	0
0.00125	-0.43213	-0.09766	4.5	0	0
0.00138	0.07568	0.65186	5	0	0
0.0015	0.48828	-0.09033	5.5	0	0
0.00163	-1.13037	-0.31982	6	0	0
0.00175	0.40771	0.03662	6.5	0	0
0.00188	0.23926	0.39307	7	0	0
0.002	0.16602	-0.30518	7.5	0	0
0.00213	-0.00977	-0.04395	8	0	0
0.00225	0.14404	0.38818	8.5	0	0
0.00238	-0.12451	-0.22949	9	0	0
0.0025	-0.79834	-0.91309	9.5	0	0
0.00263	1.43555	0.44434	10	0	0
0.00275	0.43457	0.57373	10.5	0	0
0.00288	-0.40283	-0.46875	11	0	0
0.003	-1.17676	-0.10254	11.5	0	0
0.00313	-0.06836	0.18066	12	0	0
0.00325	0.34912	-0.49072	12.5	0	0
0.00338	0.13916	0.11475	13	0	0
0.0035	0.86182	0.05371	13.5	0	0
0.00363	-0.50049	-0.17334	14	0	0
0.00375	-0.33447	-0.18311	14.5	0	0
0.00388	-0.21973	0.02686	15	0	0
0.004	-0.28809	-0.09766	15.5	0	0
0.00412	-0.01953	-0.15625	16	0	0
0.00425	0.18311	0.01465	16.5	0	0
0.00438	0.20264	-0.07813	17	0	0
0.0045	-0.39551	-0.12695	17.5	0	0
0.00463	-0.03662	-0.09766	18	0	0
0.00475	0.08301	-0.06348	18.5	0	0
0.00488	-0.27832	-0.53711	19	0	0
0.005	0.1001	-0.06592	19.5	0	0
0.00513	0.24658	0.77881	20	0	0
0.00525	-0.86182	-0.78125	20.5	0	0
0.00538	-1.04004	-0.34912	21	0	0
0.0055	0.78125	0.03174	21.5	0	0
0.00563	0.69092	-0.13184	22	0	0
0.00575	0.56641	-0.0708	22.5	0	0
0.00588	-0.1001	0.26367	23	0	0
0.006	-0.45898	-0.02686	23.5	0	0
0.00613	-0.77637	-0.41748	24	0	0
0.00625	-0.21973	0.18066	24.5	0	0
0.00638	0.87646	0.2124	25	0	0
0.0065	-0.13184	-0.28564	25.5	0	0
0.00663	-0.05615	-0.18066	26	0	0
0.00675	0.4834	0.21484	26.5	0	0
0.00688	0.04883	0.22705	27	0	0
0.007	-0.05127	-0.0415	27.5	0	0
0.00713	-0.60059	0.19531	28	0	0
0.00725	0.01953	-0.08789	28.5	0	0
0.00738	0.20508	-0.2002	29	0.00002	0.00002
0.0075	0.28564	0.42725	29.5	0	0
0.00763	0.43213	0.44678	30	0	0.00001
0.00775	-1.19629	-0.64941	30.5	0.00001	0
0.00788	0.57861	-0.04395	31	0	0
0.008	1.03271	1.22314	31.5	0	0
0.00813	-0.24902	-0.52002	32	0	0
0.00825	-1.01807	-0.22949	32.5	0	0
0.00838	-0.48584	0.78857	33	0	0
0.0085	0.48584	-0.10986	33.5	0	0
0.00863	-0.14893	-0.1001	34	0	0
0.00875	0.46631	0.20752	34.5	0	0
0.00888	0.51025	-0.16357	35	0	0
0.009	0.31494	0.39551	35.5	0	0
0.00913	-0.16846	0.16357	36	0	0
0.00925	-0.77393	-0.00977	36.5	0	0
0.00938	-0.29541	-0.2124	37	0	0

	Accel 1	Accel 2	
900-1000	=(SUM(E1809:E2009))*100	=(SUM(F1809:F2009))*100	
"940" value	0.01213		**sample 1**
900-1000	=(SUM(E17809:E18009))*100	=(SUM(F17809:F18009))*100	
"940" value	0.01127		**sample 2**
900-1000	=(SUM(E33809:E34009))*100	=(SUM(F33809:F34009))*100	
"940" value	0.01643		**sample 3**
900-1000	=AVERAGE(I2,I4,I6)	=AVERAGE(J2,J4,J6)	
"940" value	=AVERAGE(I3,I5,I7)		**AVG**
900-1000	=STDEV(I2,I4,I6)	=STDEV(J2,J4,J6)	
"940" value	=STDEV(I7,I5,I3)		**STDEV**

900-1400

	Accel 1	Accel 2	
sample 1	=(SUM(E1809:E2809))*500	=(SUM(F1809:F2809))*500	
sample 2	=(SUM(E17809:E18809))*500	=(SUM(F17809:F18809))*500	
sample3	=(SUM(E33809:E34809))*500	=(SUM(F33809:F34809))*500	
avg	=AVERAGE(I15:I17)	=AVERAGE(J15:J17)	
stdev	=STDEV(I15:I17)	=STDEV(J15:J17)	

1200-1700

	Accel 1	Accel 2	
sample 1	=(SUM(E2409:E3409))*500	=(SUM(F2409:F3409))*500	
sample 2	=(SUM(E18409:E19409))*500	=(SUM(F18409:F19409))*500	
sample3	=(SUM(E34409:E35409))*500	=(SUM(F34409:F35409))*500	
avg	=AVERAGE(I23:I25)	=AVERAGE(J23:J25)	
stdev	=STDEV(I23:I25)	=STDEV(J23:J25)	

1700-2100

	Accel 1	Accel 2	
sample 1	=(SUM(E3409:E4209))*400	=(SUM(F3409:F4209))*400	
sample 2	=(SUM(E19409:E20209))*400	=(SUM(F19409:F20209))*400	
sample3	=(SUM(E35409:E36209))*400	=(SUM(F35409:F36209))*400	
avg	=AVERAGE(I31:I33)	=AVERAGE(J31:J33)	
stdev	=STDEV(I31:I33)	=STDEV(J31:J33)	

1250-1350

	Accel 1	Accel 2	
sample 1	=(SUM(E2509:E2709))*100	=(SUM(F2509:F2709))*100	
sample 2	=(SUM(E18509:E18709))*100	=(SUM(F18509:F18709))*100	
sample3	=(SUM(E34509:E34709))*100	=(SUM(F34509:F34709))*100	
avg	=AVERAGE(I39:I41)	=AVERAGE(J39:J41)	
stdev	=STDEV(I39:I41)	=STDEV(J39:J41)	

1700-1800

	Accel 1	Accel 2	
sample 1	=(SUM(E3409:E3609))*100	=(SUM(F3409:F3609))*100	
sample 2	=(SUM(E19409:E19609))*100	=(SUM(F19409:F19609))*100	
sample3	=(SUM(E35409:E35609))*100	=(SUM(F35409:F35609))*100	
avg	=AVERAGE(I47:I49)	=AVERAGE(J47:J49)	
stdev	=STDEV(I47:I49)	=STDEV(J47:J49)	

1800-1900

	Accel 1	Accel 2	
sample 1	=(SUM(E3609:E3809))*100	=(SUM(F3609:F3809))*100	
sample 2	=(SUM(E19609:E19809))*100	=(SUM(F19609:F19809))*100	
sample3	=(SUM(E35609:E35809))*100	=(SUM(F35609:F35809))*100	
avg	=AVERAGE(I55:I57)	=AVERAGE(J55:J57)	
stdev	=STDEV(I55:I57)	=STDEV(J55:J57)	

1900-2000

	Accel 1	Accel 2	
sample 1	=(SUM(E3809:E4009))*100	=(SUM(F3809:F4009))*100	
sample 2	=(SUM(E19809:E20009))*100	=(SUM(F19809:F20009))*100	
sample3	=(SUM(E35809:E36009))*100	=(SUM(F35809:F36009))*100	
avg	=AVERAGE(I63:I65)	=AVERAGE(J63:J65)	
stdev	=STDEV(I63:I65)	=STDEV(J63:J65)	

2000-2100

	Accel 1	Accel 2	
sample 1	=(SUM(E4009:E4209))*100	=(SUM(F4009:F4209))*100	
sample 2	=(SUM(E20009:E20209))*100	=(SUM(F20009:F20209))*100	
sample3	=(SUM(E36009:E36209))*100	=(SUM(F36009:F36209))*100	
avg	=AVERAGE(I71:I73)	=AVERAGE(J71:J73)	
stdev	=STDEV(I71:I73)	=STDEV(J71:J73)	

2550-2700

	Accel 1	Accel 2	
sample 1	=(SUM(E5109:E5409))*150	=(SUM(F5109:F5409))*150	
sample 2	=(SUM(E21109:E21409))*150	=(SUM(F21109:F21409))*150	
sample3	=(SUM(E37109:E37409))*150	=(SUM(F37109:F37409))*150	
avg	=AVERAGE(I79:I81)	=AVERAGE(J79:J81)	
stdev	=STDEV(I79:I81)	=STDEV(J79:J81)	

Appendix G – DX Bushing Dimple Count

No. dimples
93
88
93
93
92
92
92
93
92
93
93
93
92
93
91
93
93
92
93
91
Avg 92.3
Std Dev 1.2

Appendix H – RTF Test Detailed Data
RTF 2 Raw Data Plots:

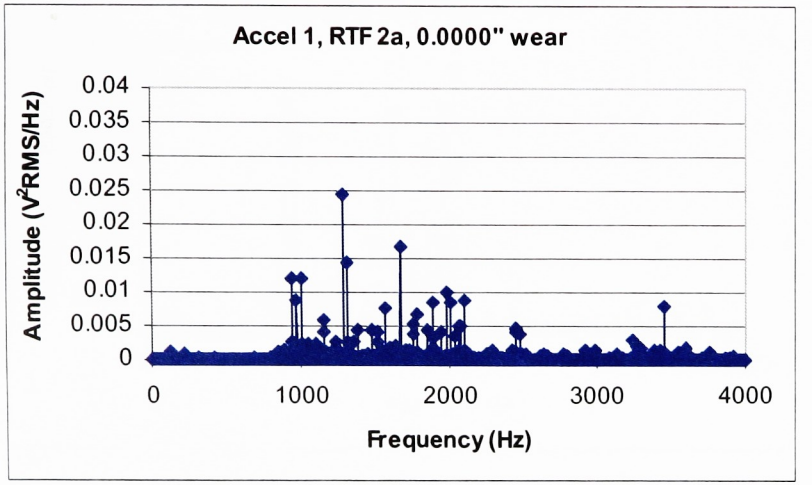

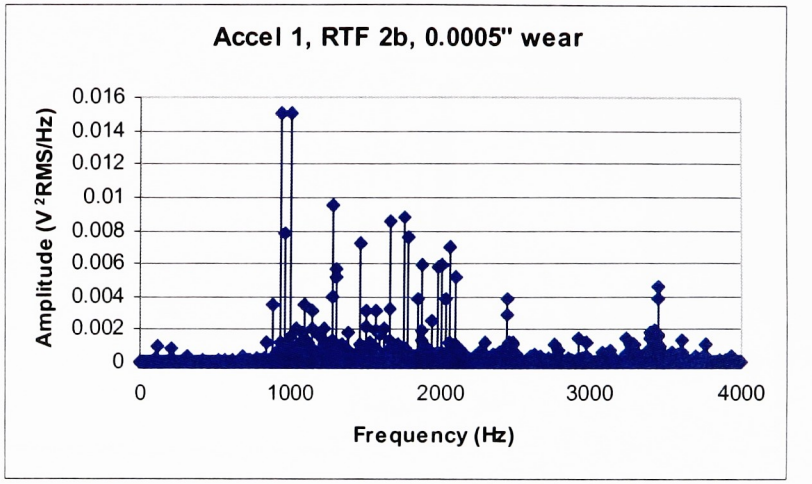

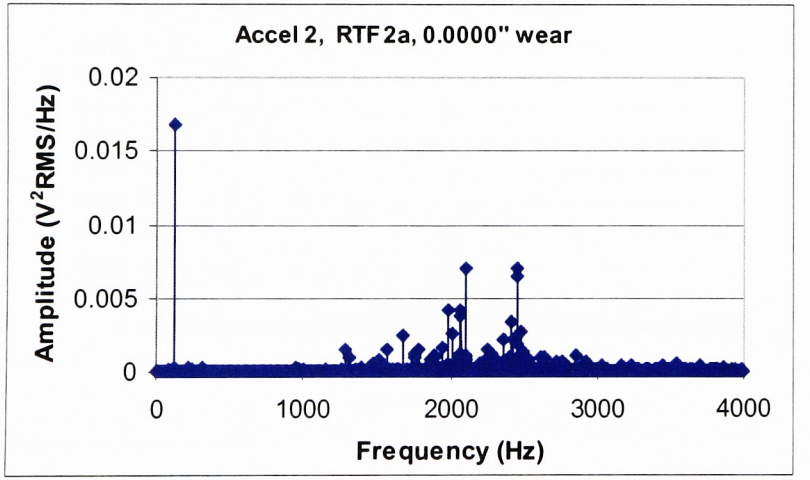

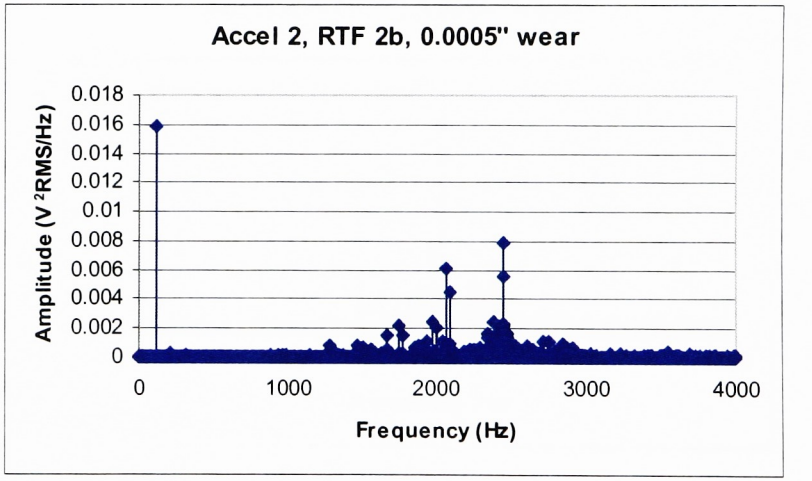

(RTF 2 Raw Data Plots, continued)

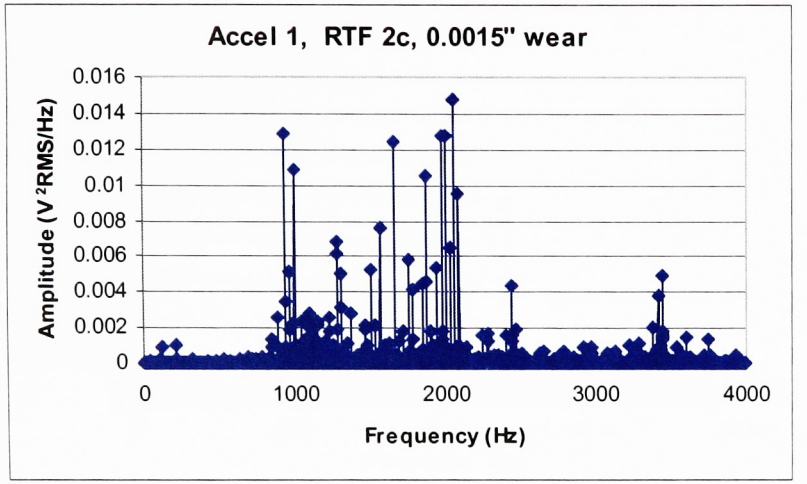

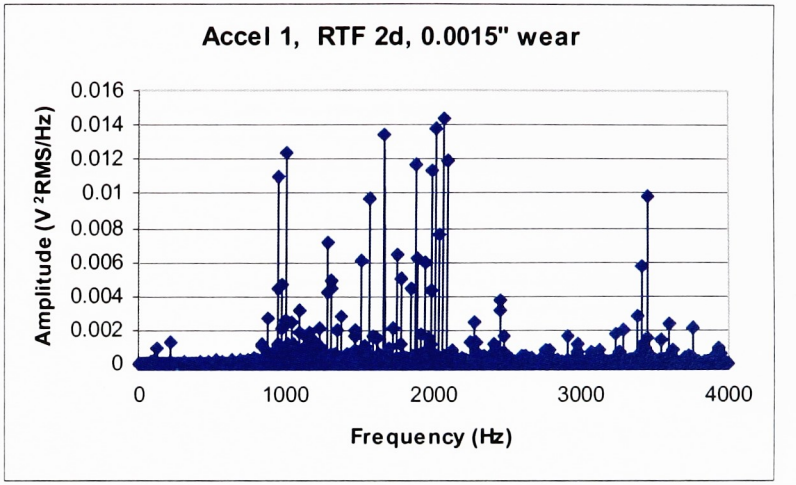

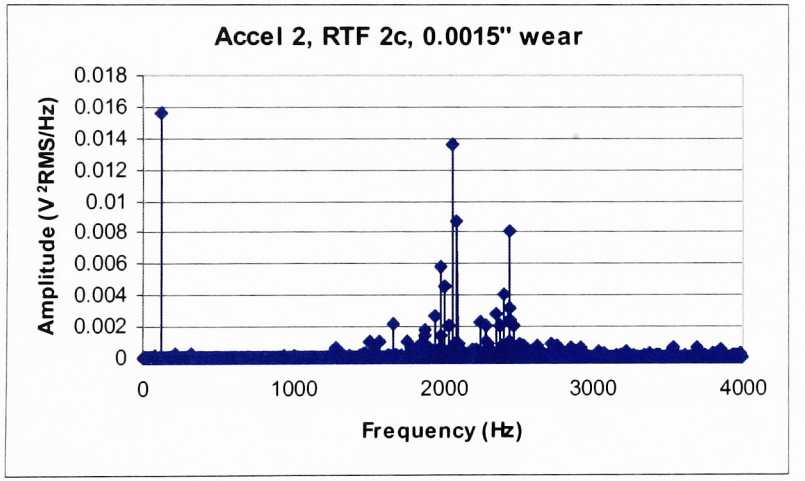

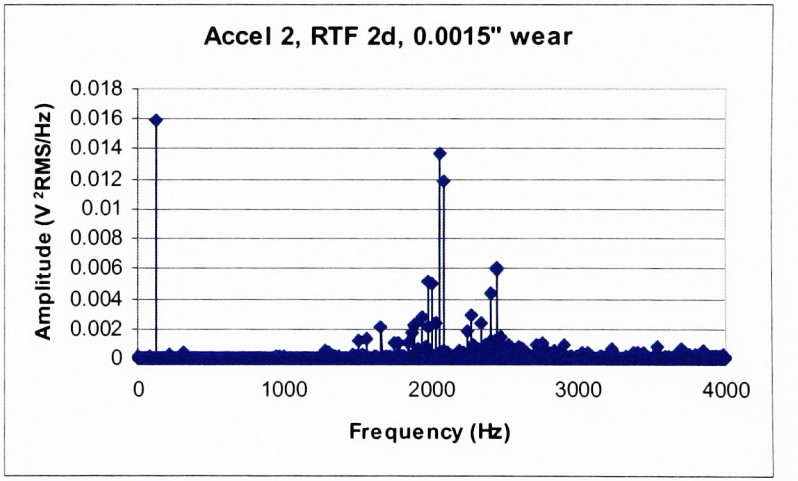

(RTF 2 Raw Data Plots, continued)

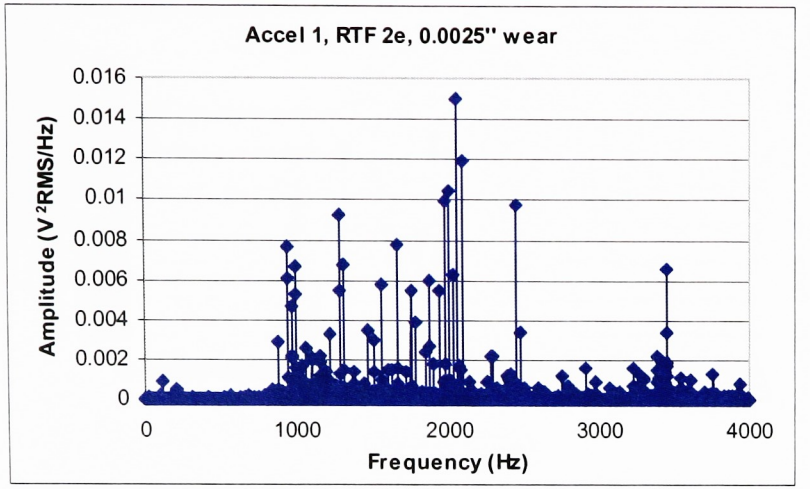

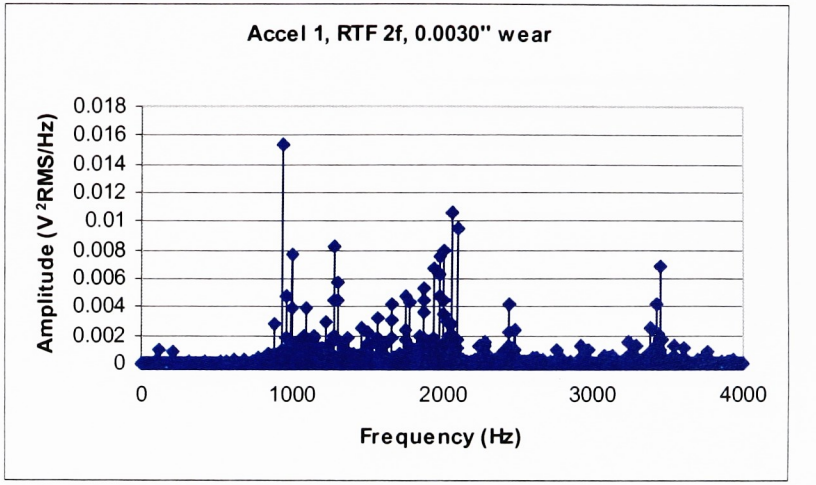

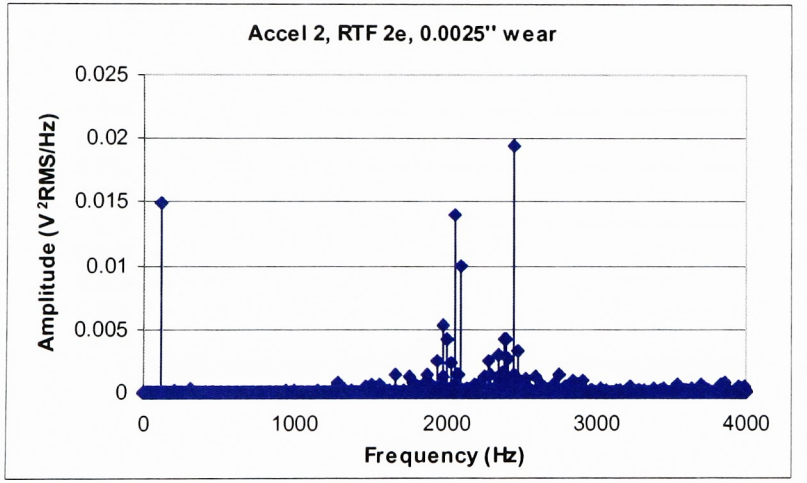

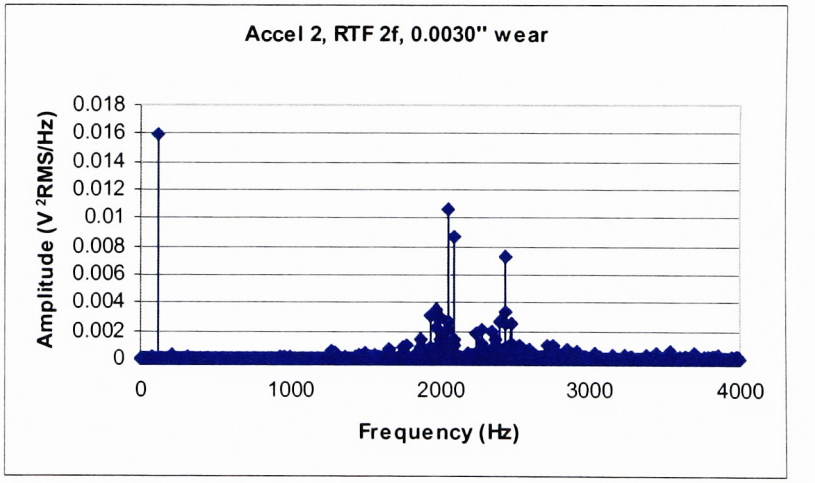

(RTF 2 Raw Data Plots, continued)

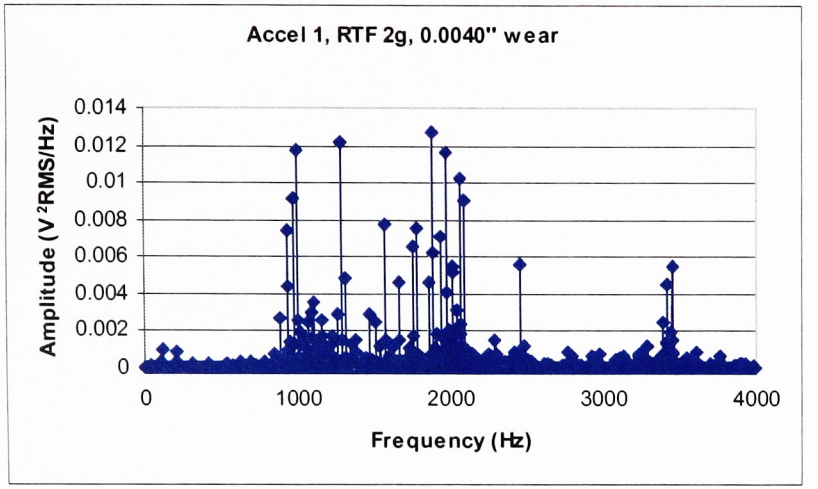

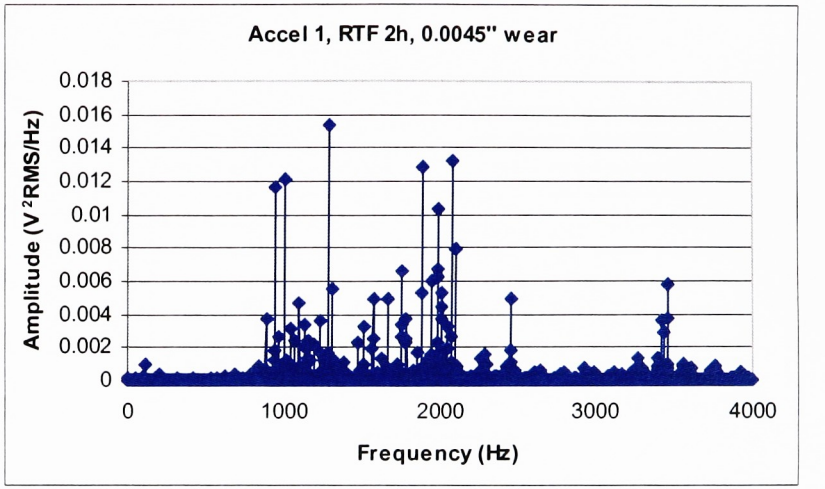

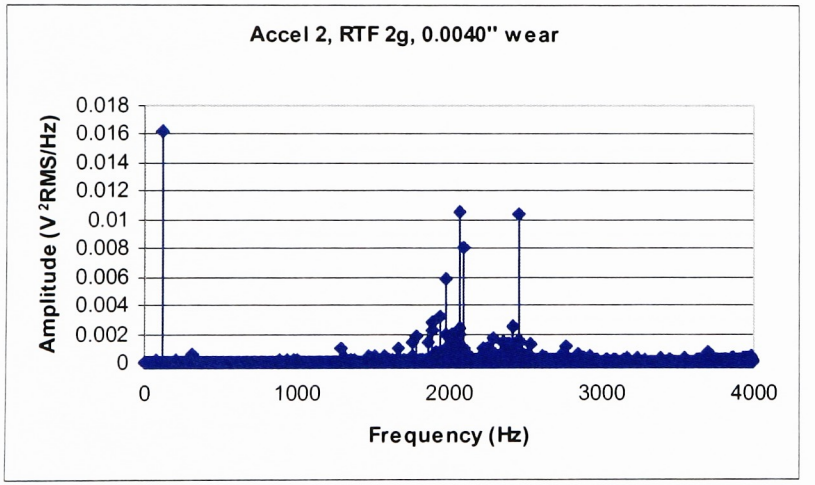

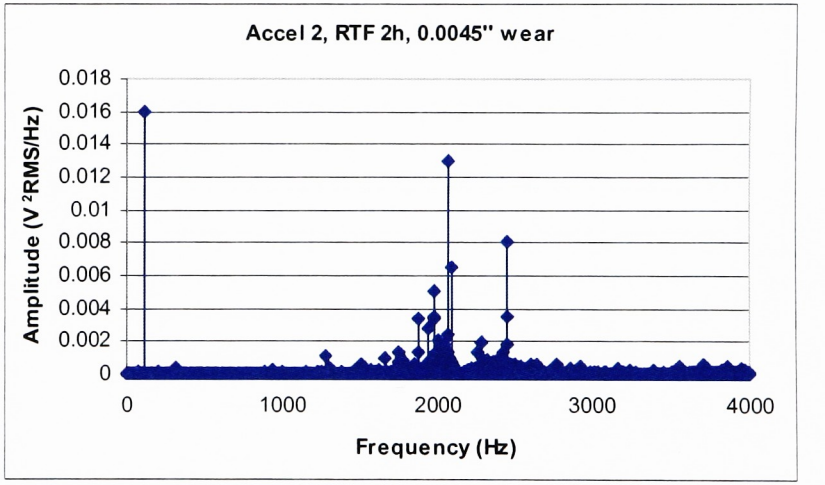

(RTF 2 Raw Data Plots, continued)

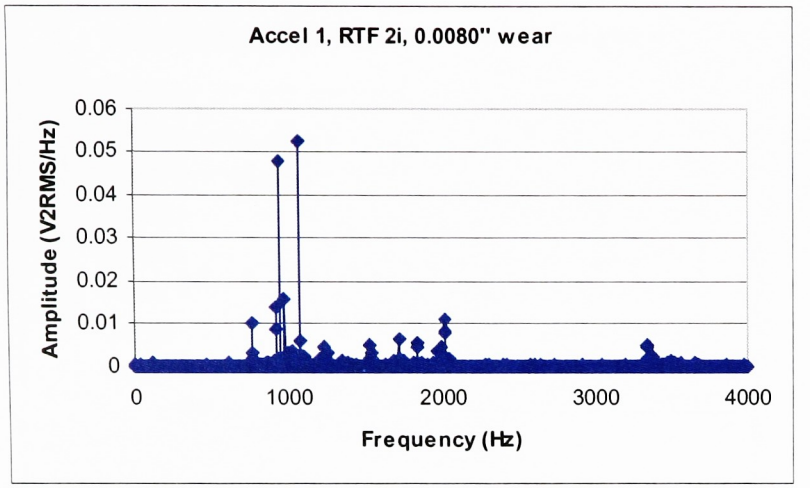

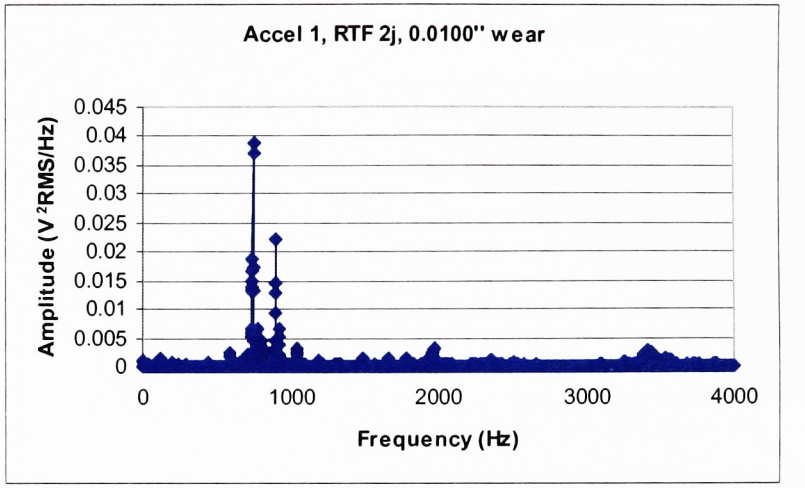

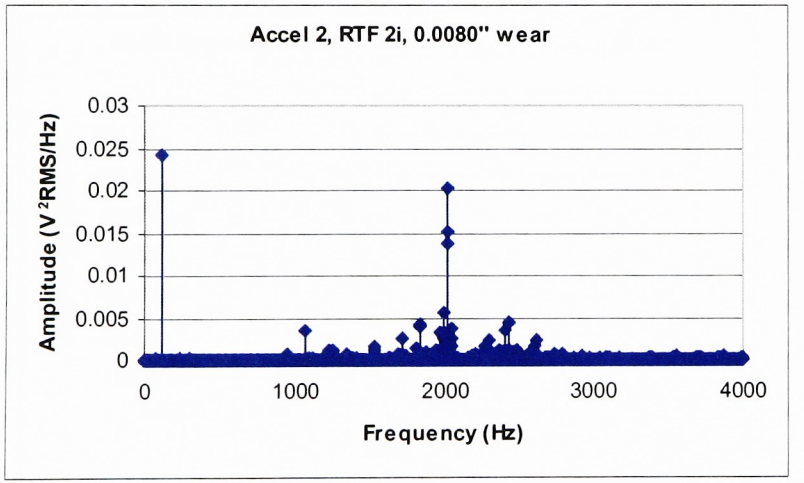

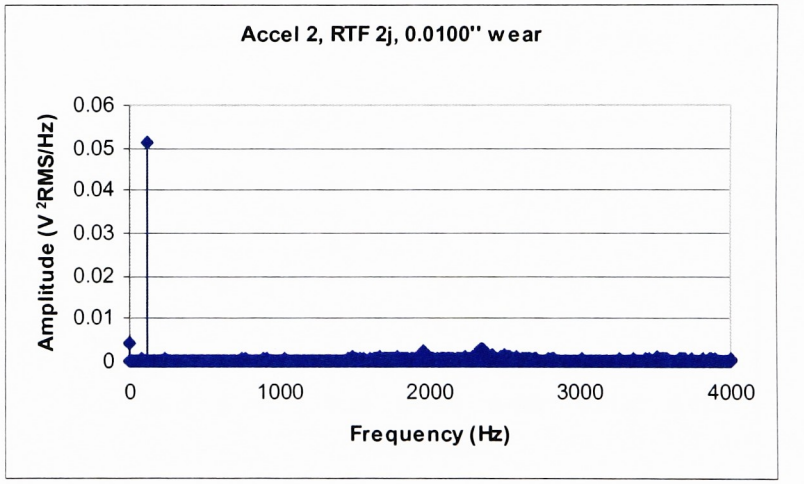

RTF 2: Band Power for Various Frequency Bands

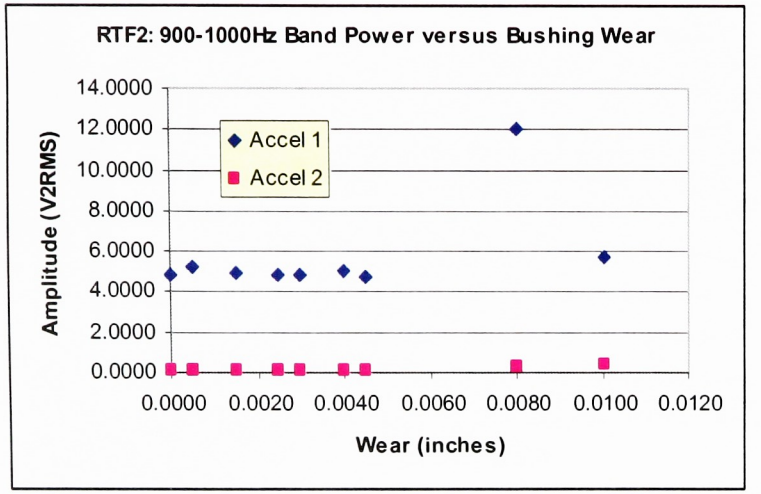

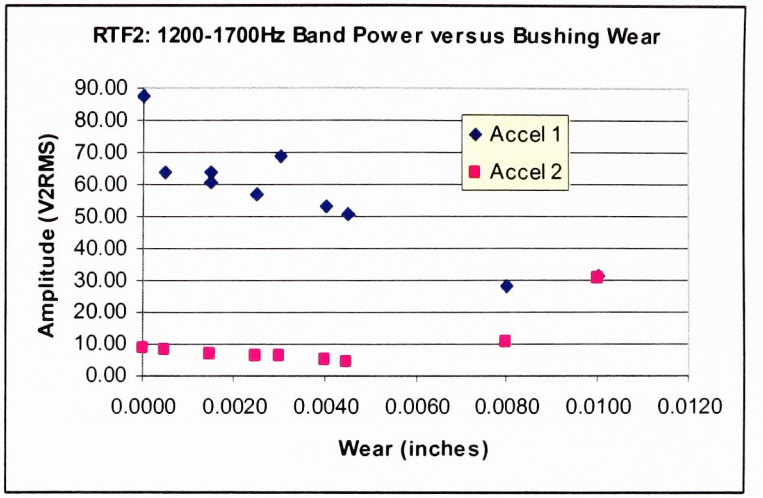

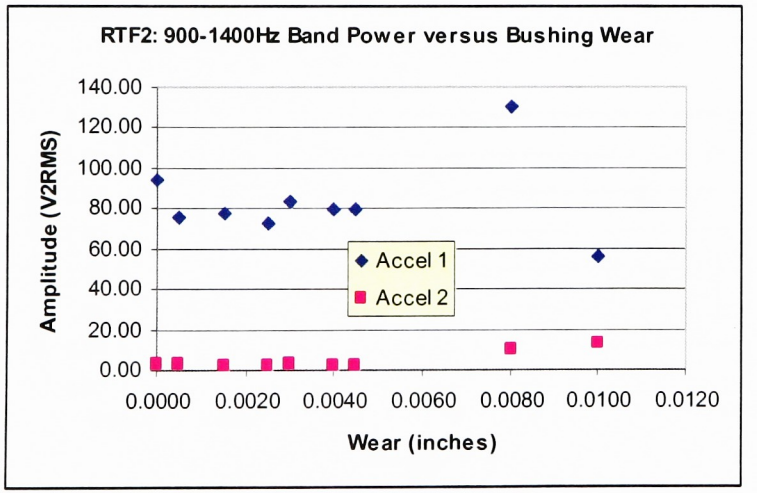

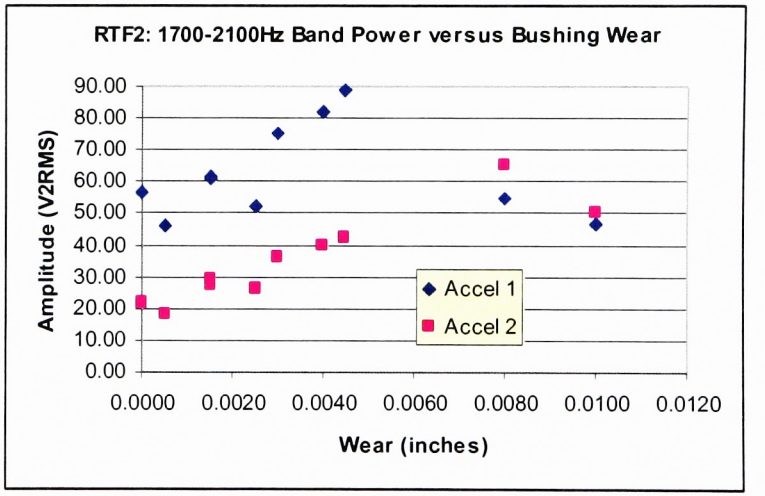

(RTF 2 Band Power for Various Frequency Bands, continued)

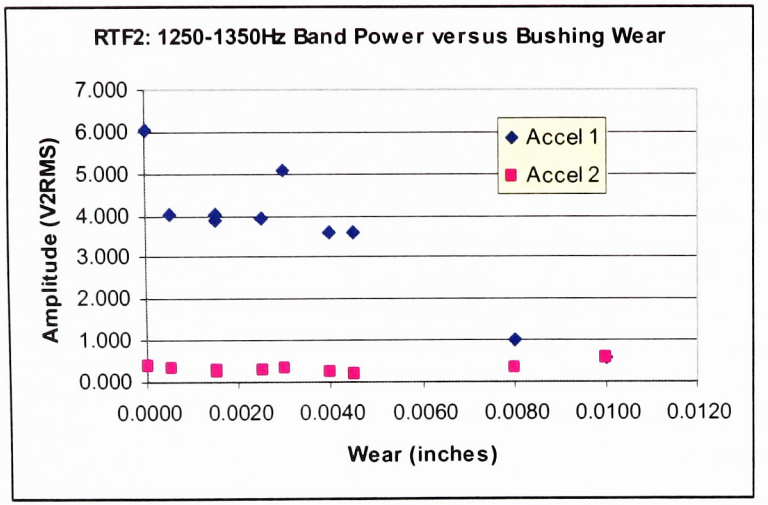

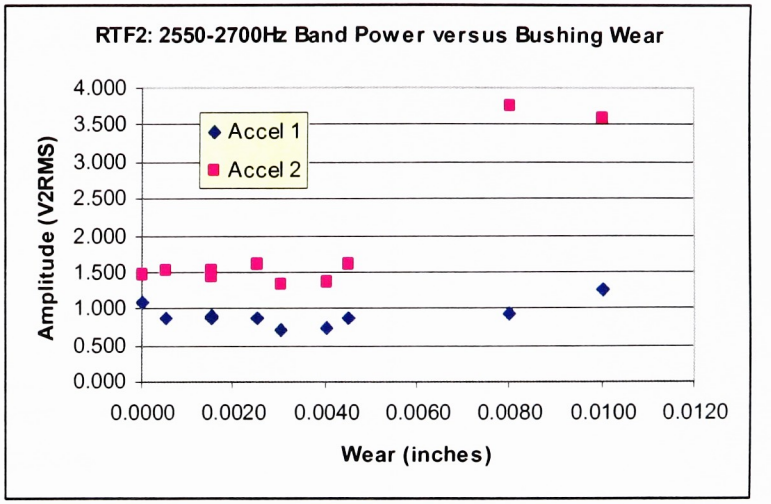

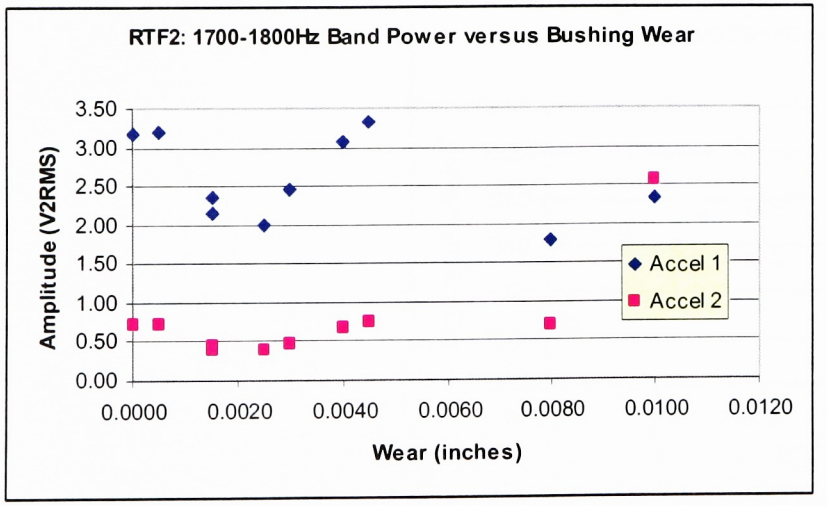

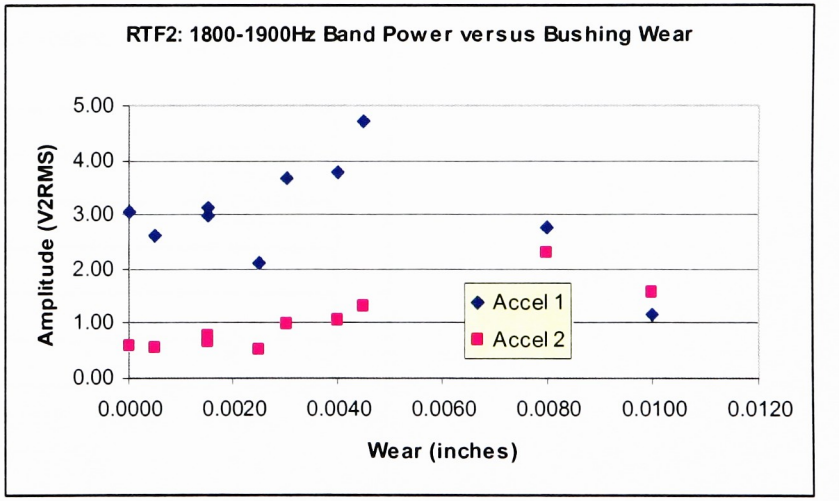

(RTF 2 Band Power for Various Frequency Bands, continued)

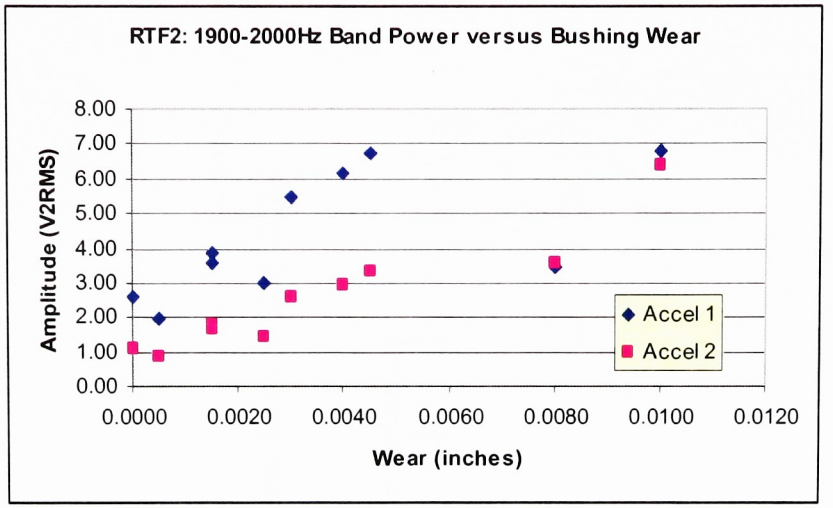

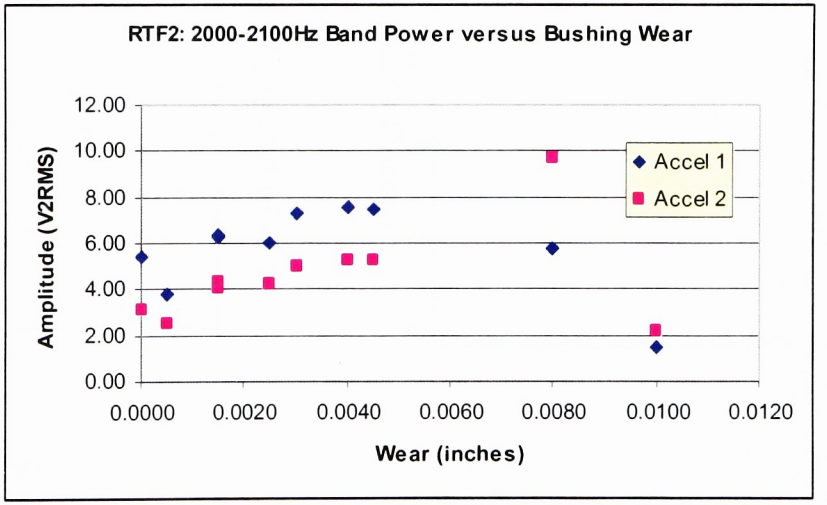

Appendix I – Outlier Elimination Details

MATLAB Code:

```
>> %RTF2 Confidence Plots
>> polytool(RTF2wear,RTF2_17_21,1,0.05)
>> polytool(RTF2wear,RTF2_20_21,1,0.05)
```

RTF2, 1700-2100 Hz 95% Confidence Interval Plot

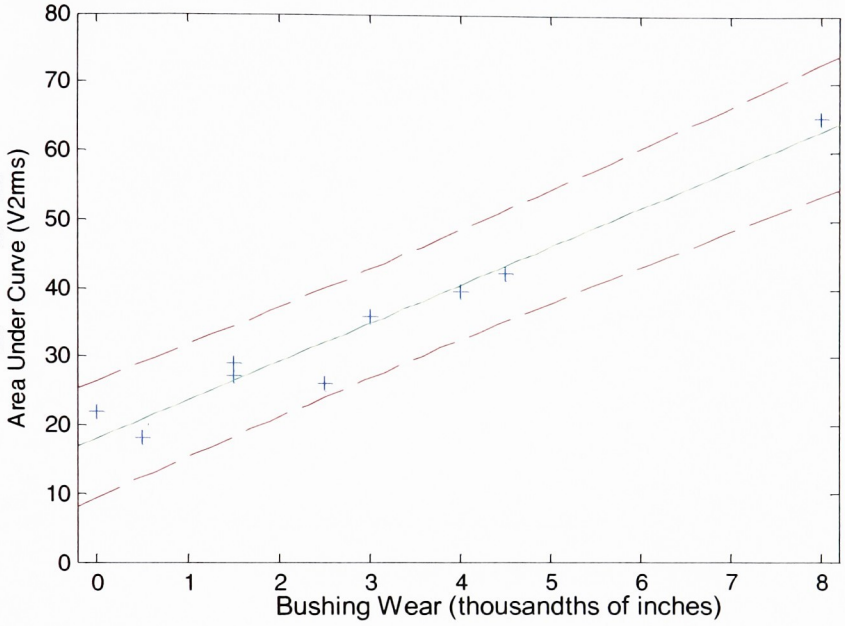

RTF2, 2000-2100 Hz 95% Confidence Interval Plot

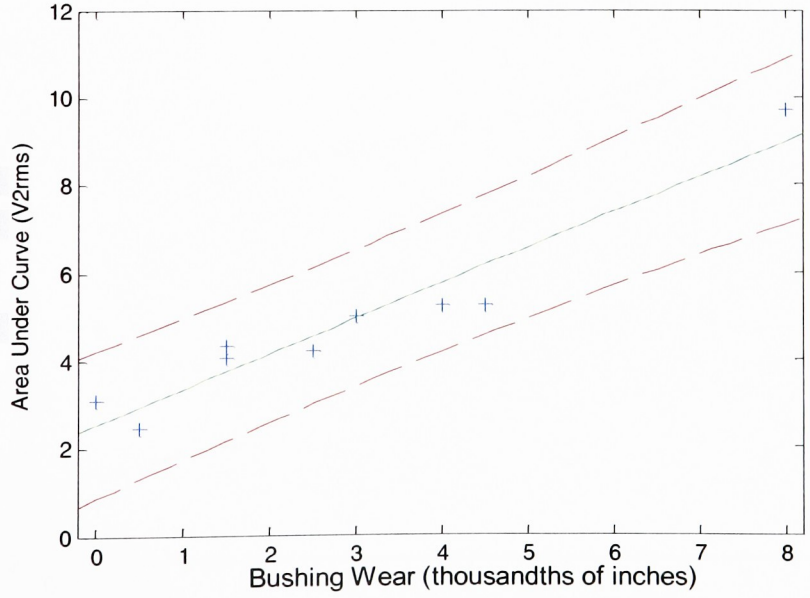

```
>> %RTF3 Confidence Plots
>> polytool(RTF3wear,RTF3_17_21,1,0.05)
>> polytool(RTF3wear,RTF3_20_21,1,0.05)
```

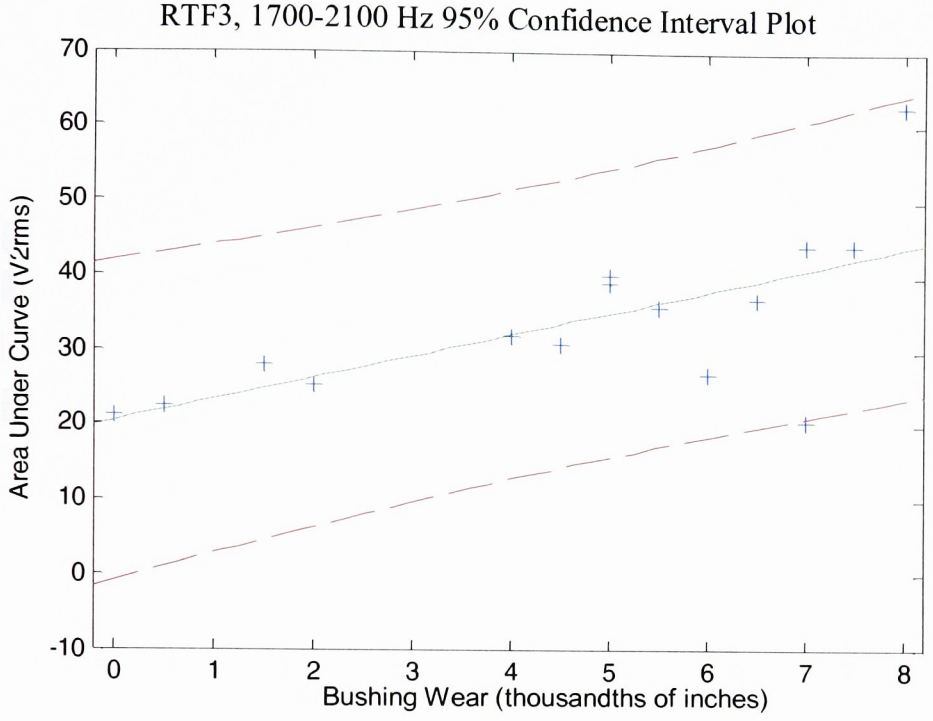

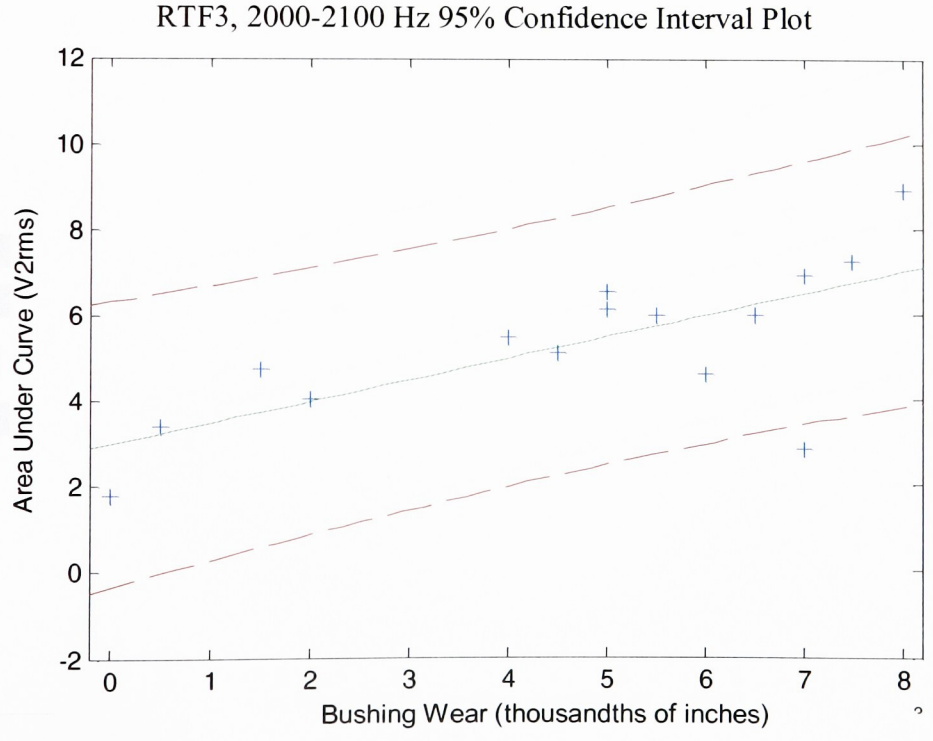

```
>> %RTF4 Confidence Plots
>> polytool(RTF4wear,RTF4_17_21,1,0.05)
>> polytool(RTF4wear,RTF4_20_21,1,0.05)
```

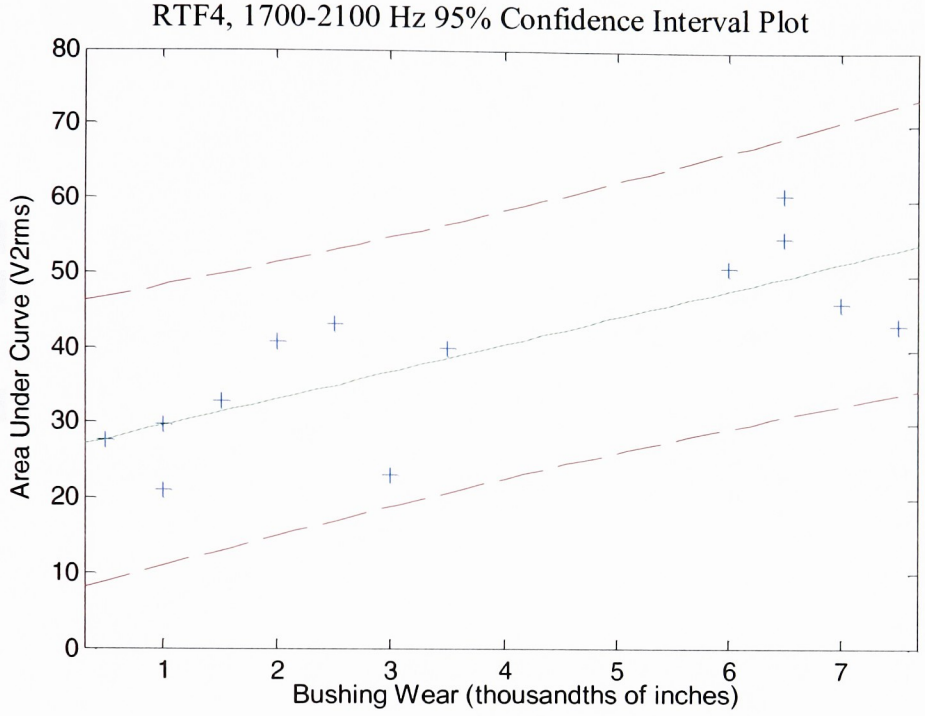

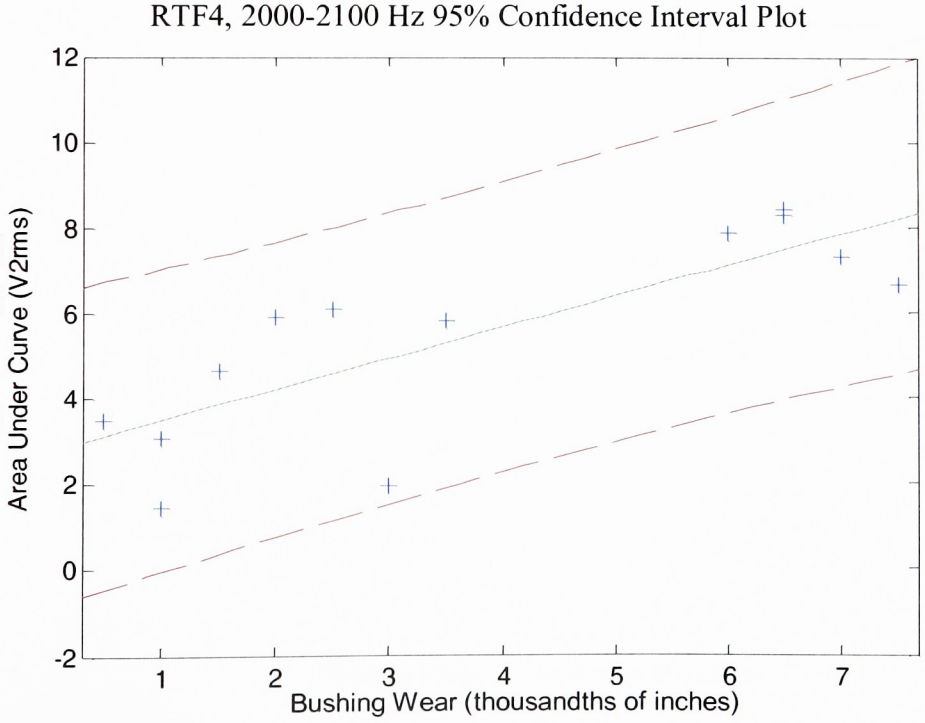

```
>> %RTF3 Confidence Plots, 2nd Iteration
>> polytool(RTF3wear_2nditeration,RTF3_17_21_2nditeration,1,0.05)
>> polytool(RTF3wear_2nditeration,RTF3_20_21_2nditeration,1,0.05)
```

RTF3, 1700-2100 Hz 95% Confidence Interval Plot, Second Iteration

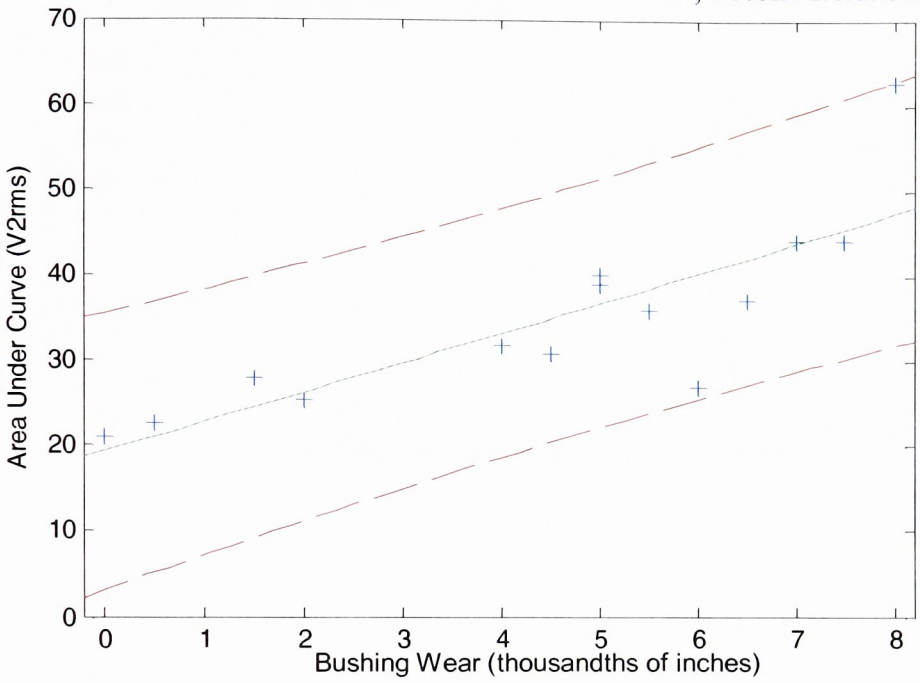

RTF3, 2000-2100 Hz 95% Confidence Interval Plot, Second Iteration

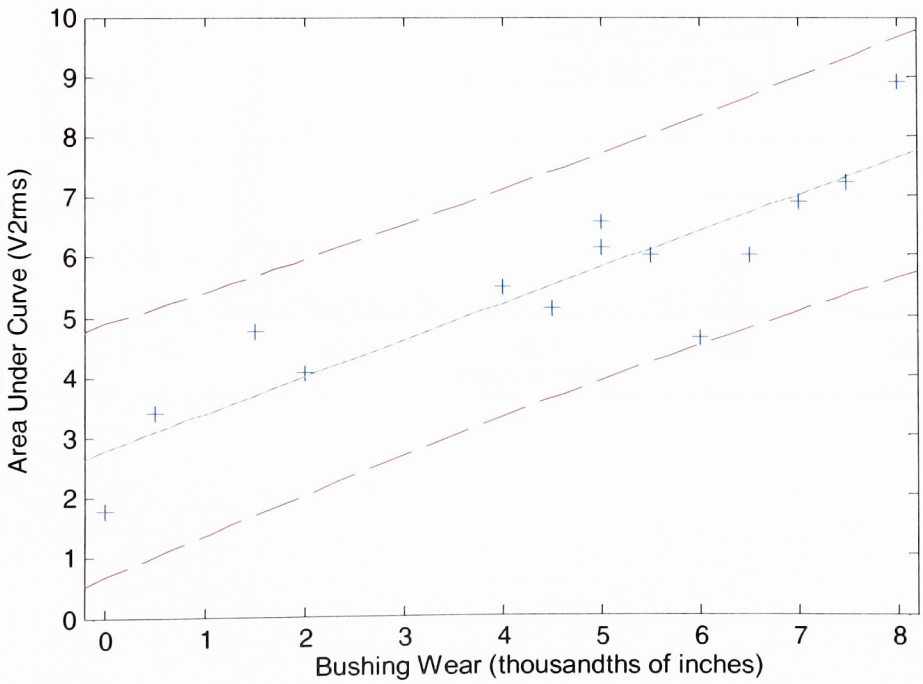

Appendix J – Planet Gear Bushing Dimple Geometry Comparison

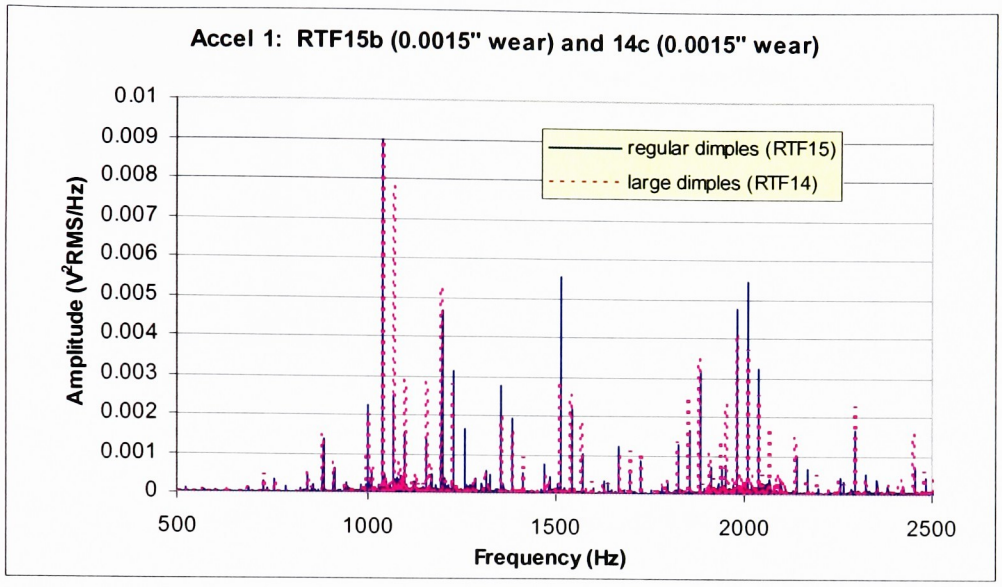

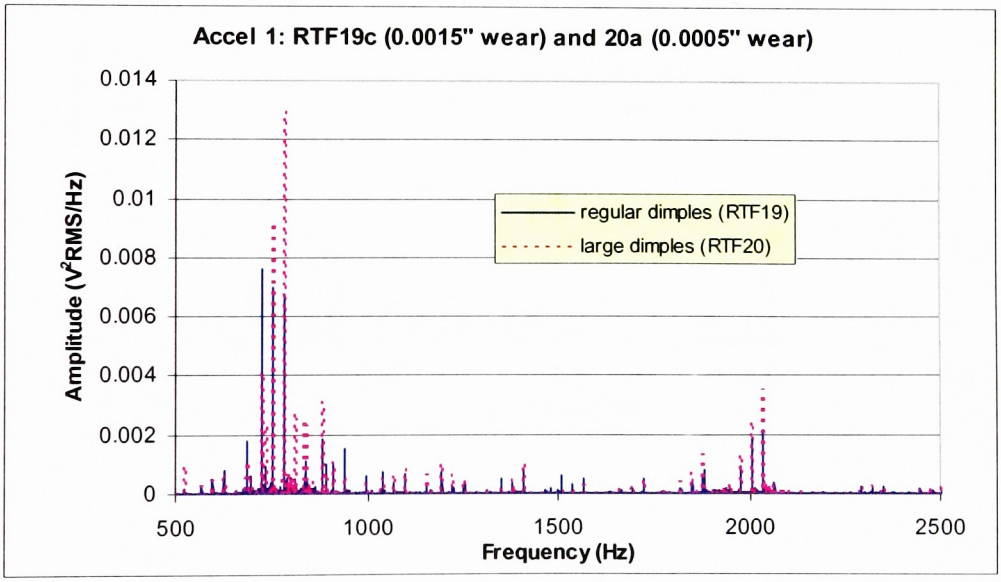

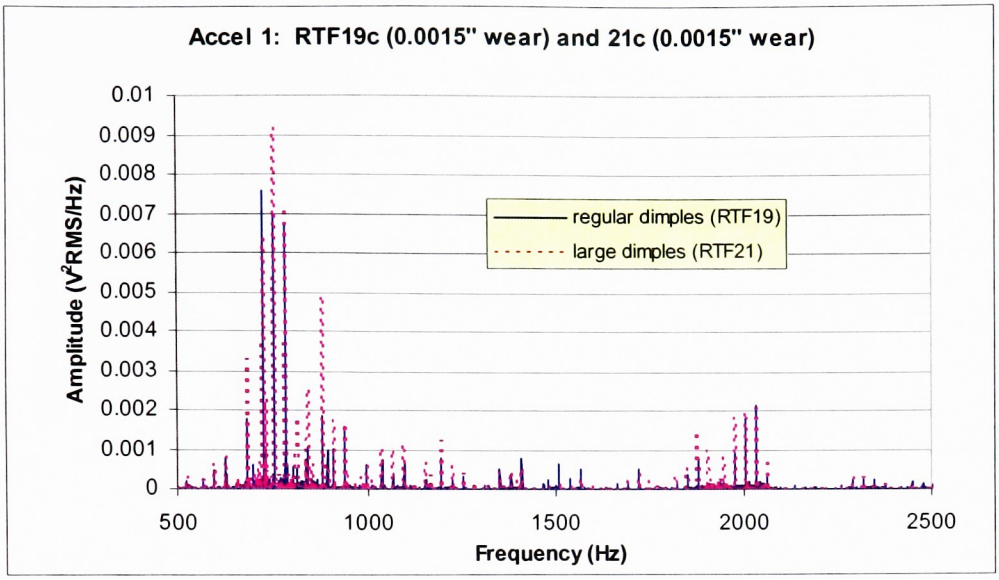
Accel 1: RTF19c (0.0015" wear) and 21c (0.0015" wear)
Amplitude (V²RMS/Hz)
0.01
0.009
0.008
0.007
0.006
0.005
0.004
0.003
0.002
0.001
0
500
1000
1500
2000
2500
Frequency (Hz)
regular dimples (RTF19)
large dimples (RTF21)

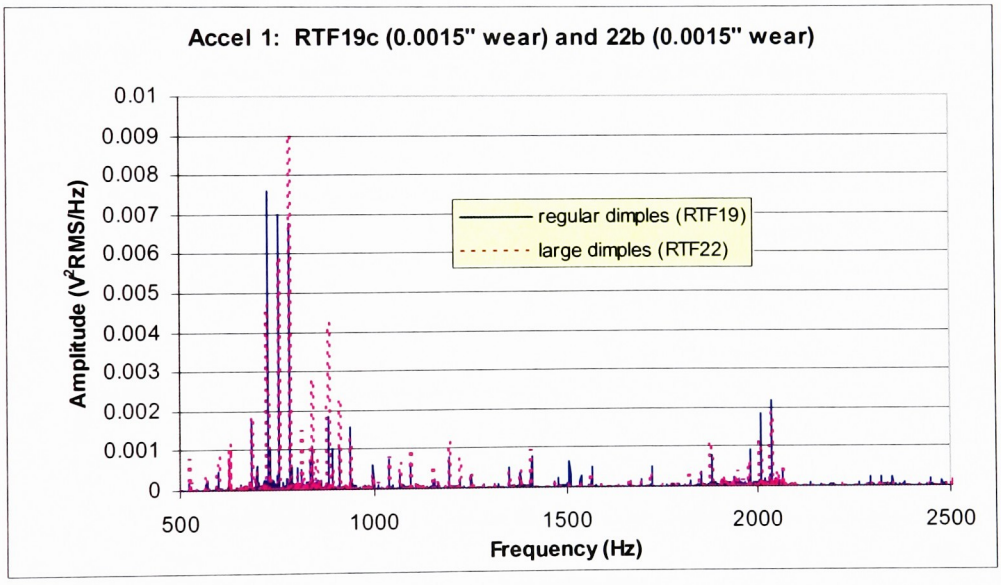
Accel 1: RTF19c (0.0015" wear) and 22b (0.0015" wear)
Amplitude (V²RMS/Hz)
0.01
0.009
0.008
0.007
0.006
0.005
0.004
0.003
0.002
0.001
0
500
1000
1500
2000
2500
Frequency (Hz)
regular dimples (RTF19)
large dimples (RTF22)

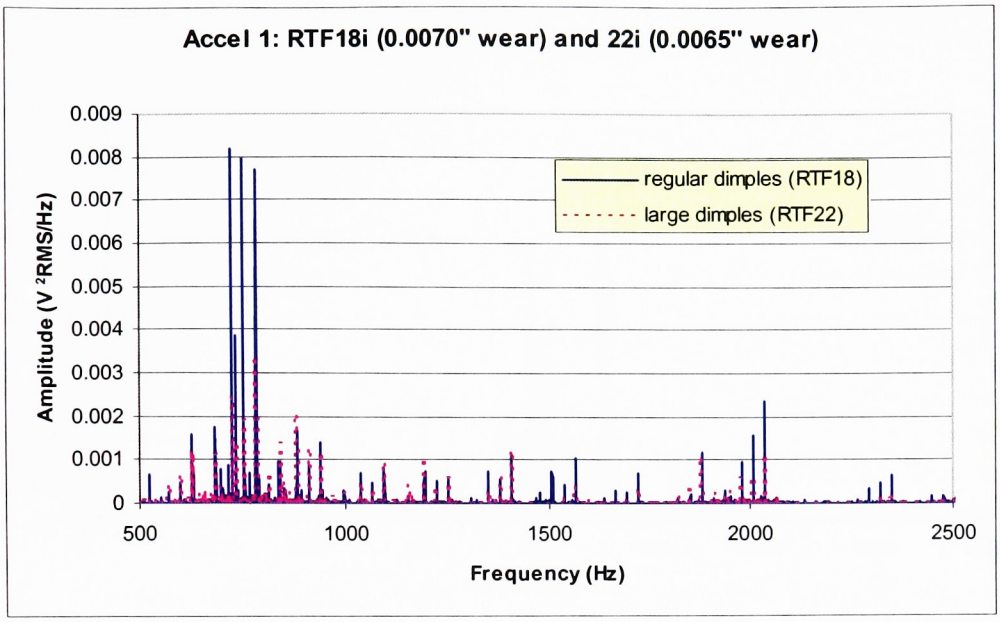
Accel 1: RTF18i (0.0070" wear) and 22i (0.0065" wear)
Amplitude (V ²RMS/Hz)
0.009
0.008
0.007
0.006
0.005
0.004
0.003
0.002
0.001
0
500
1000
1500
2000
2500
Frequency (Hz)
regular dimples (RTF18)
large dimples (RTF22)

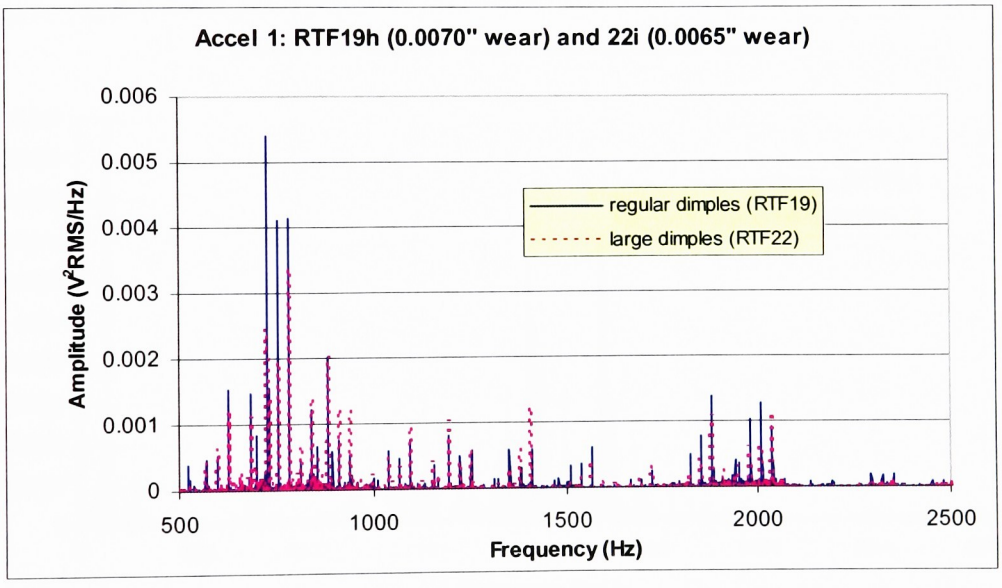
Accel 1: RTF19h (0.0070" wear) and 22i (0.0065" wear)
Amplitude (V²RMS/Hz)
0.006
0.005
0.004
0.003
0.002
0.001
0
500
1000
1500
2000
2500
Frequency (Hz)
regular dimples (RTF19)
large dimples (RTF22)

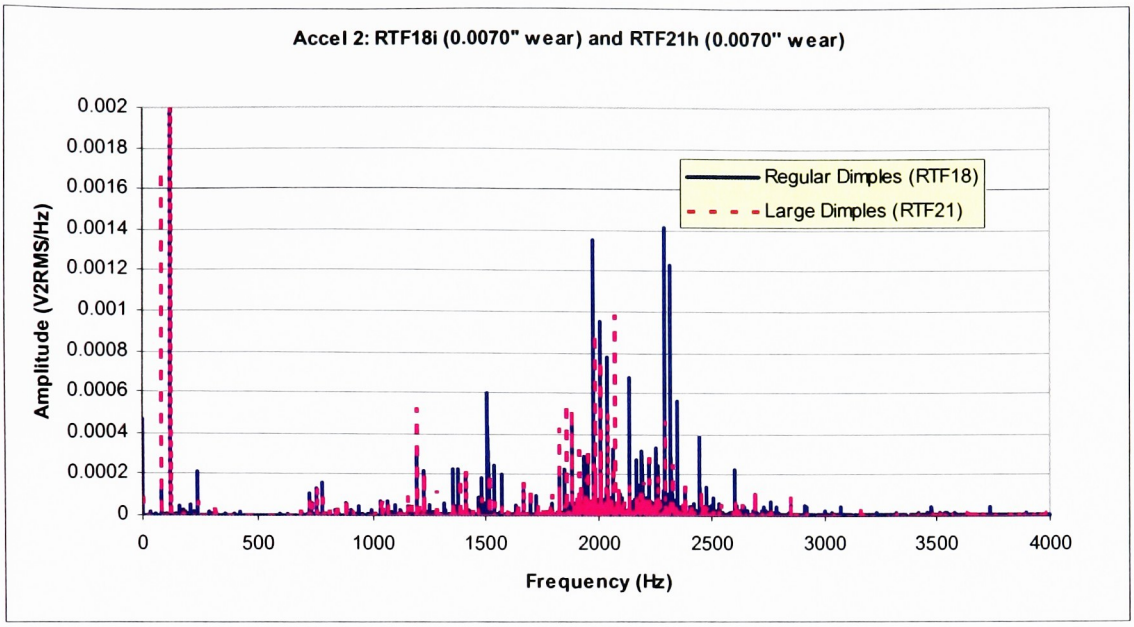
Accel 2: RTF18i (0.0070" wear) and RTF21h (0.0070" wear)
Amplitude (V2RMS/Hz)
0.002
0.0018
0.0016
0.0014
0.0012
0.001
0.0008
0.0006
0.0004
0.0002
0
0
500
1000
1500
2000
2500
3000
3500
4000
Frequency (Hz)
Regular Dimples (RTF18)
Large Dimples (RTF21)

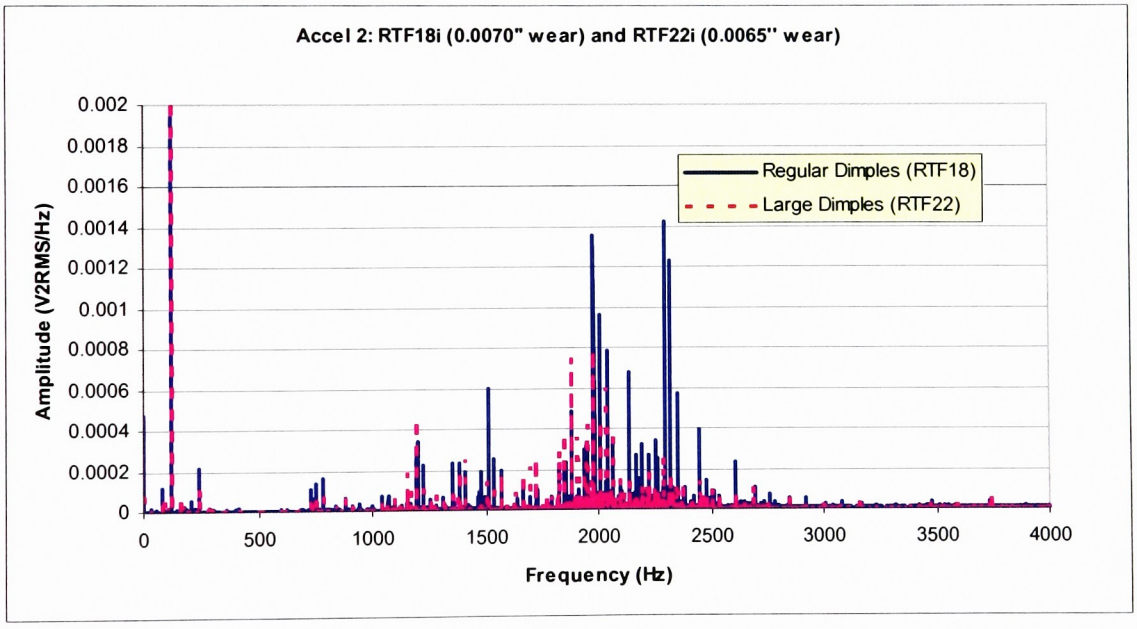
Accel 2: RTF18i (0.0070" wear) and RTF22i (0.0065" wear)
Amplitude (V2RMS/Hz)
0.002
0.0018
0.0016
0.0014
0.0012
0.001
0.0008
0.0006
0.0004
0.0002
0
0
500
1000
1500
2000
2500
3000
3500
4000
Frequency (Hz)
Regular Dimples (RTF18)
Large Dimples (RTF22)

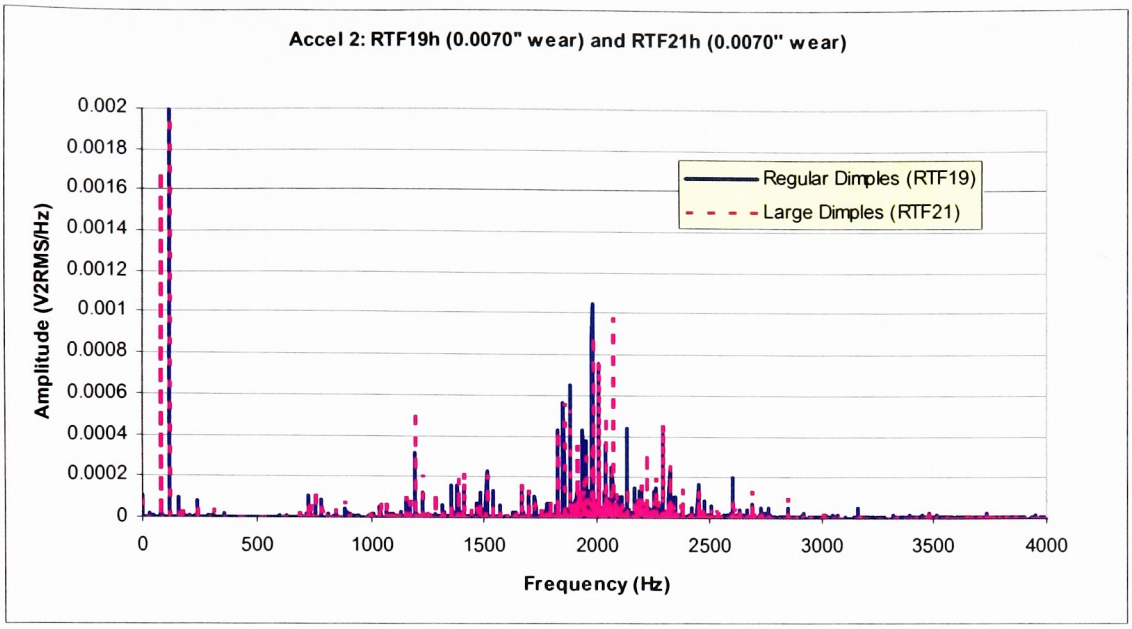
Accel 2: RTF19h (0.0070" wear) and RTF21h (0.0070" wear)
Amplitude (V2RMS/Hz)
0.002
0.0018
0.0016
0.0014
0.0012
0.001
0.0008
0.0006
0.0004
0.0002
0
0
500
1000
1500
2000
2500
3000
3500
4000
Frequency (Hz)
Regular Dimples (RTF19)
Large Dimples (RTF21)

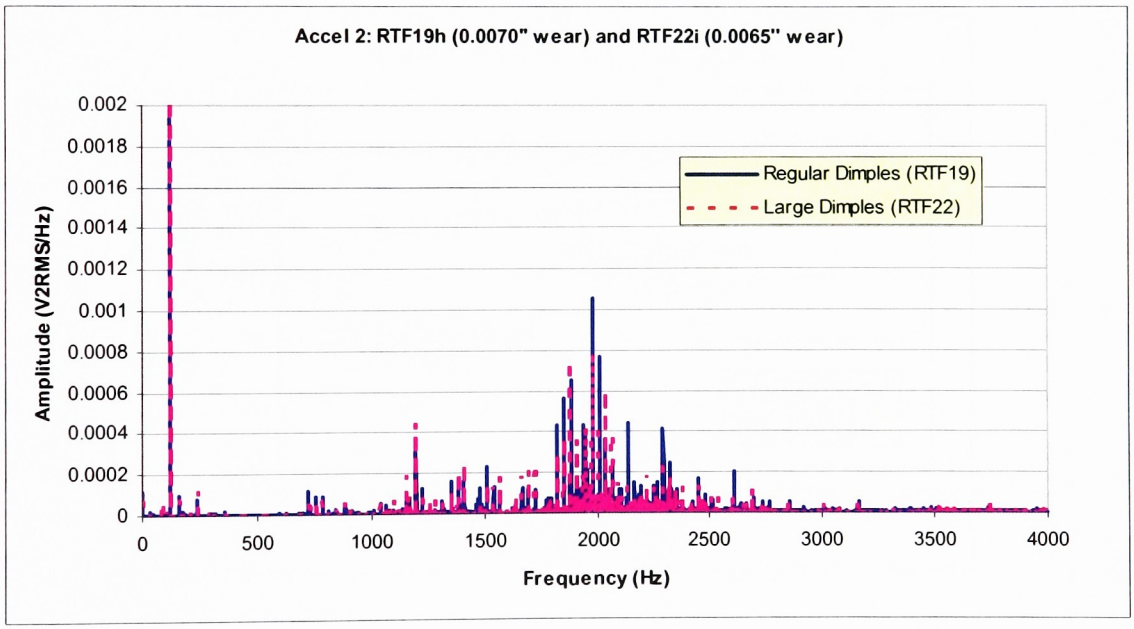
Accel 2: RTF19h (0.0070" wear) and RTF22i (0.0065" wear)
Amplitude (V2RMS/Hz)
0.002
0.0018
0.0016
0.0014
0.0012
0.001
0.0008
0.0006
0.0004
0.0002
0
0
500
1000
1500
2000
2500
3000
3500
4000
Frequency (Hz)
Regular Dimples (RTF19)
Large Dimples (RTF22)

Appendix K –Bushing Dimple Geometry Comparison via Band Power Plots

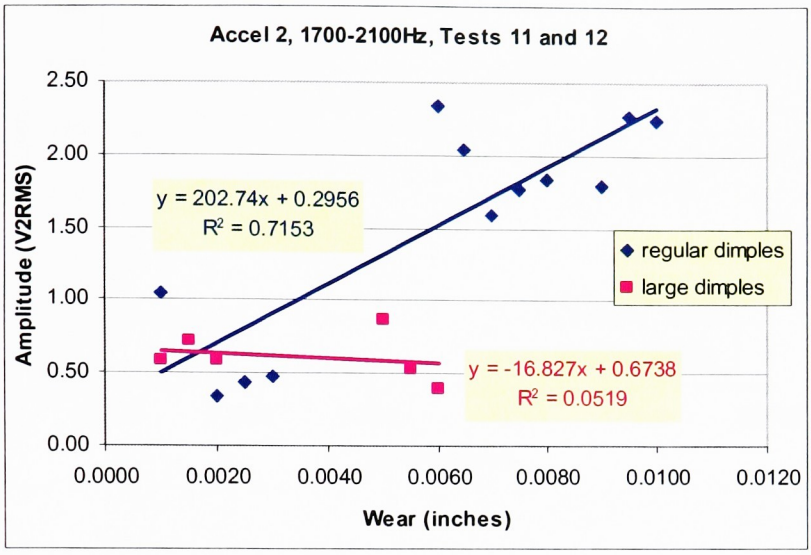

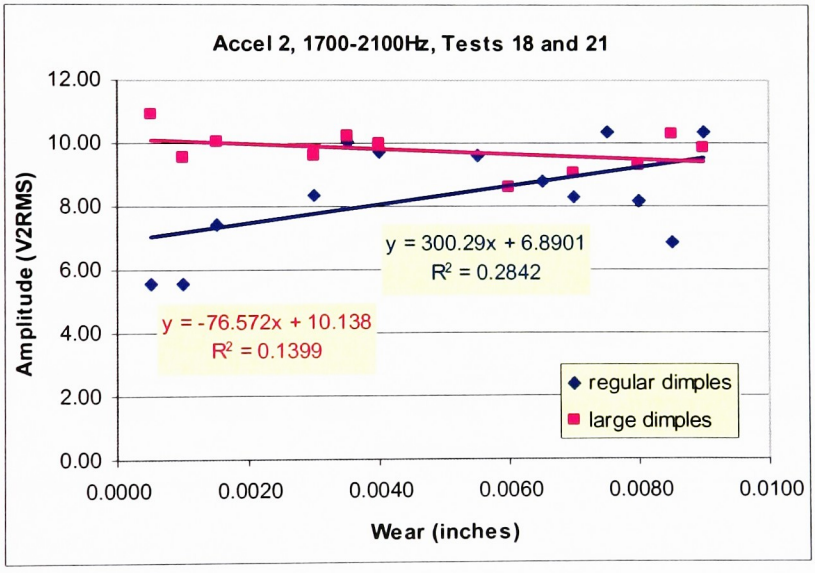

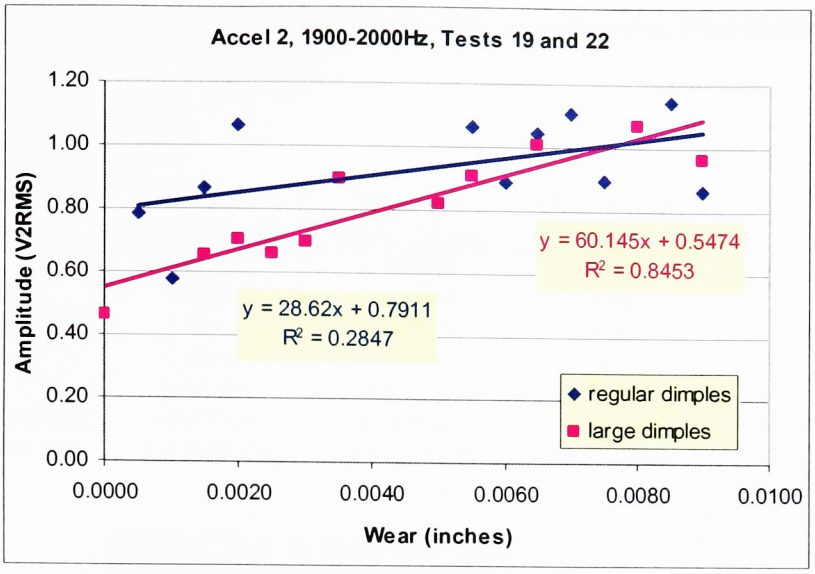
Accel 2, 1900-2000Hz, Tests 19 and 22
Amplitude (V2RMS)
1.20
1.00
0.80
0.60
0.40
0.20
0.00
0.0000
0.0020
0.0040
0.0060
0.0080
0.0100
Wear (inches)
y = 60.145x + 0.5474
R² = 0.8453
y = 28.62x + 0.7911
R² = 0.2847
regular dimples
large dimples

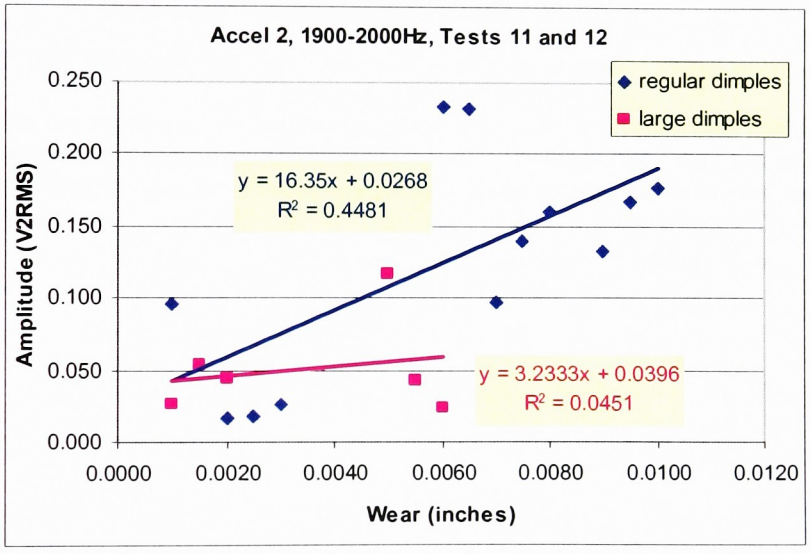
Accel 2, 1900-2000Hz, Tests 11 and 12
Amplitude (V2RMS)
0.250
0.200
0.150
0.100
0.050
0.000
0.0000
0.0020
0.0040
0.0060
0.0080
0.0100
0.0120
Wear (inches)
regular dimples
large dimples
y = 16.35x + 0.0268
R² = 0.4481
y = 3.2333x + 0.0396
R² = 0.0451

Appendix L – Bushing Block, Pin, and Bushing Dimensions

	[1]Original Pin Diameter (in)	[2]New Pin Diameter (in)	Bushing ID (in)
	0.98410	0.98310	0.9864
	0.98425	0.98315	0.9864
	0.98405	0.98310	0.9866
	0.98425	0.98305	0.9862
	0.98425	0.98310	0.9862
Average	**0.984180**	**0.983100**	**0.98636**
Std Dev	**9.7468E-05**	**3.5355E-05**	**1.67332E-04**

Pin Type	Clearance (in)
original pin	0.00109
"new" pin	0.00163

[1]The "original" pins are those with a diameter specification of 0.9840". These were used during RTF testing.

[2]The "new" pins are those with a diameter specification of 0.9830". When new ball bearings were installed, the pins did not fit through the ID since the ID was slilghtly less than that of the original ball bearings. Therefore, the pin diameter was reduced. These smaller diameter pins were used during large dimple testing.

Table L-1. Pin-bushing Clearance Values

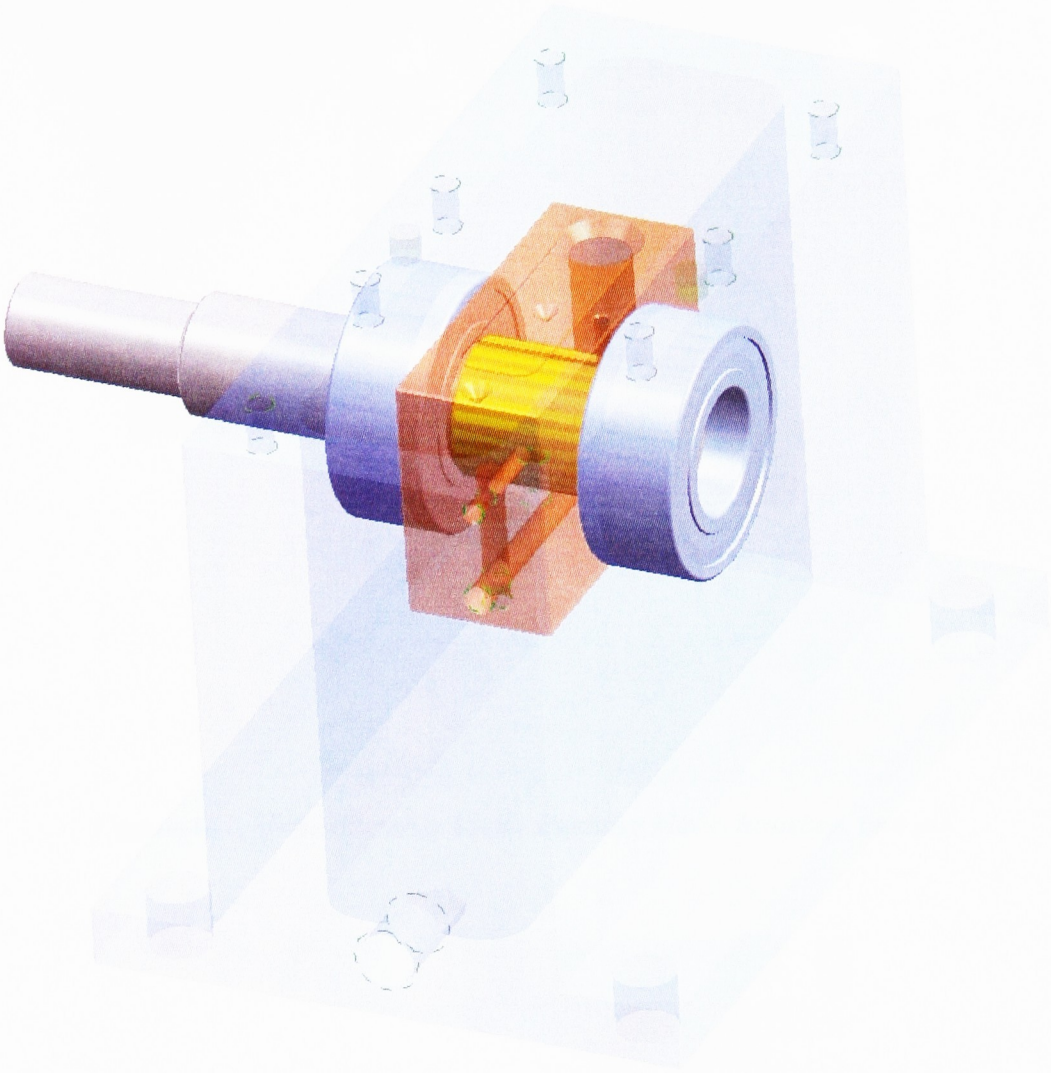

Figure L-1. Isometric Assembly View: Bushing block, housing, and pin

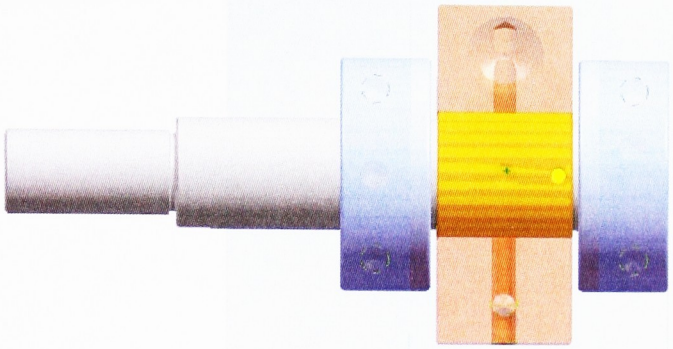

Figure L-2. Top Assembly View: Bushing block, housing, and pin

Figure L-3. Side Assembly View: Bushing block, housing, and pin

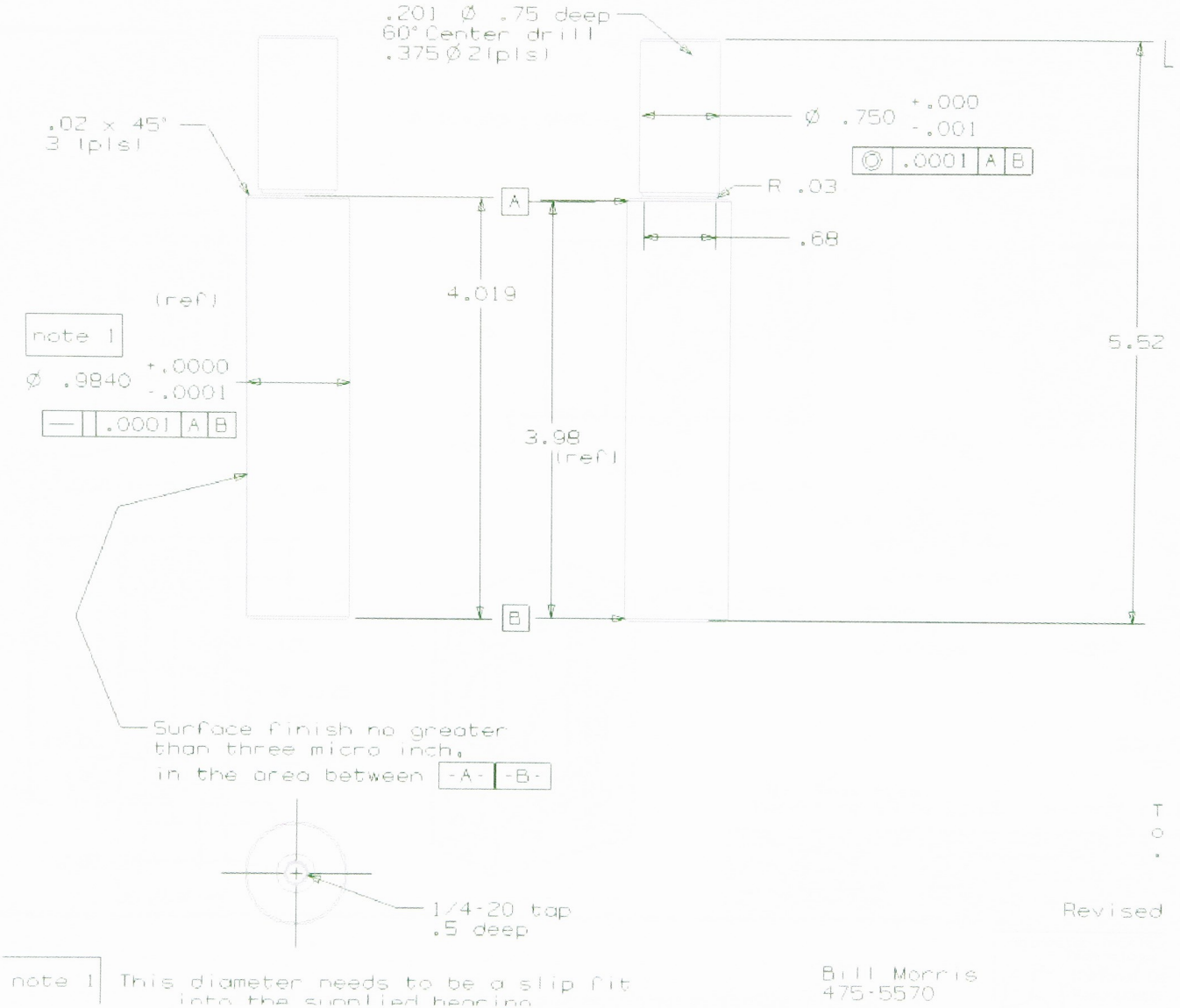

Figure L-4. Dimension Drawing for Pin

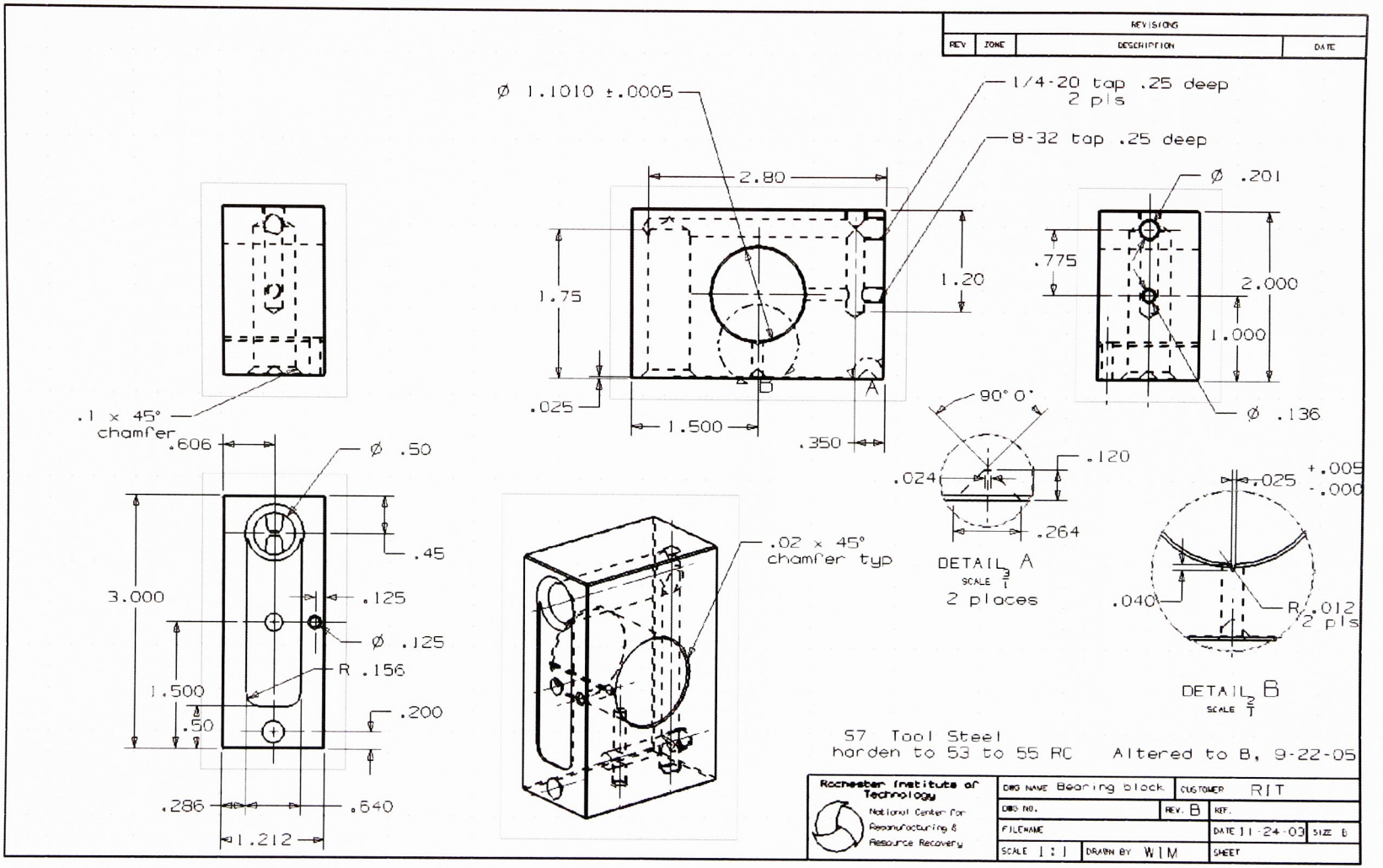

SH2 (DWG) WORK

Figure L-5. Dimension Drawing for Bushing Block

Appendix M – 50% Confidence Bands for Bushing Wear versus Band Power

Note: RTF3 data was plotted omitting the outlier found in Section 6.6 and Appendix I

MATALB Code:

```
>> % 50% Confidence Bands
>> % Plotting Bushing wear versus Band Power for Prediction Purposes
>> polytool(RTF2_17_21,RTF2wear,1,0.5)
>> polytool(RTF2_20_21,RTF2wear,1,0.5)
>> polytool(RTF3_17_21_2nditeration,RTF3wear_2nditeration,1,0.5)
>> polytool(RTF3_20_21_2nditeration,RTF3wear_2nditeration,1,0.5)
>> polytool(RTF4_17_21,RTF4wear,1,0.5)
>> polytool(RTF4_20_21,RTF4wear,1,0.5)
```

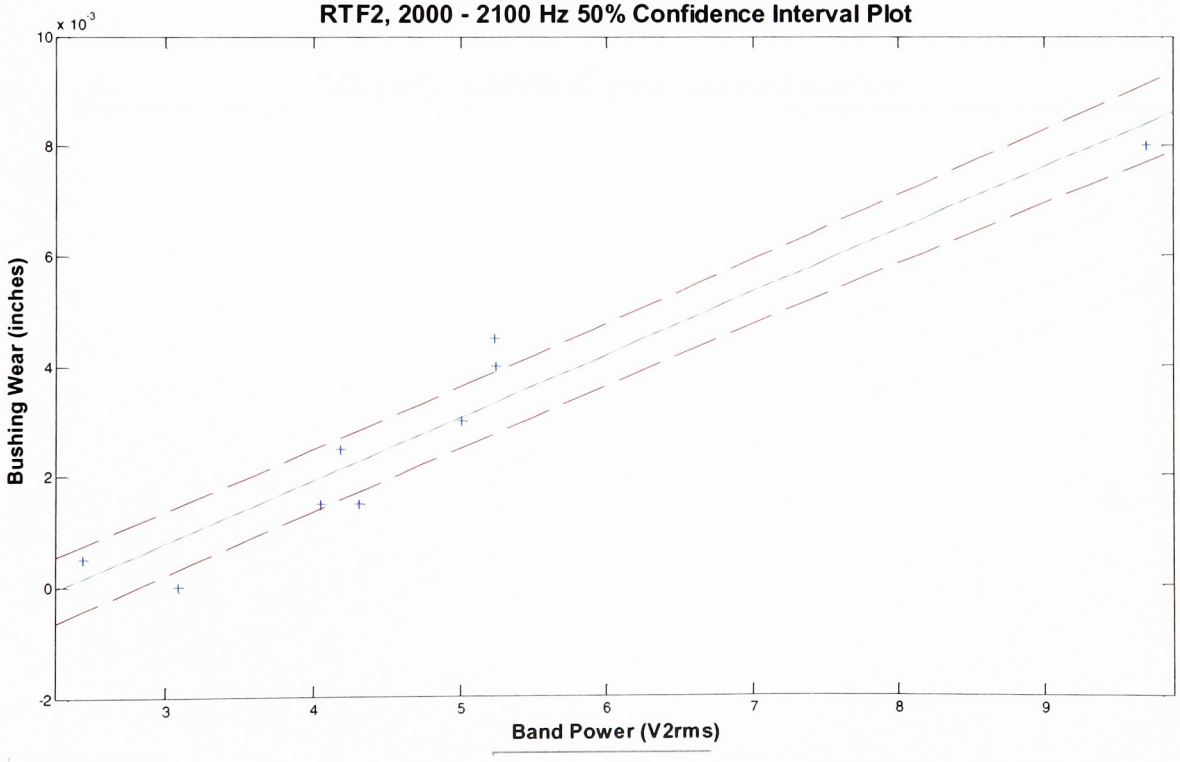

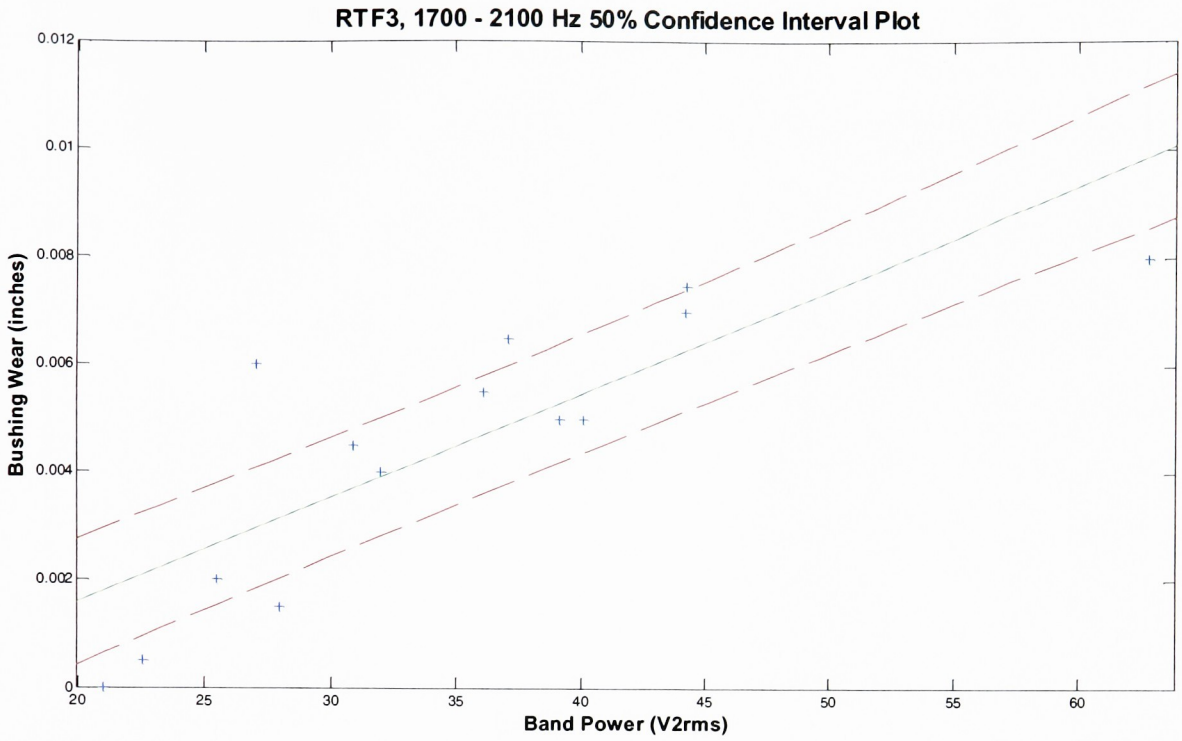
RTF3, 1700 - 2100 Hz 50% Confidence Interval Plot
Bushing Wear (inches)
Band Power (V2rms)
0.012
0.01
0.008
0.006
0.004
0.002
0
20
25
30
35
40
45
50
55
60

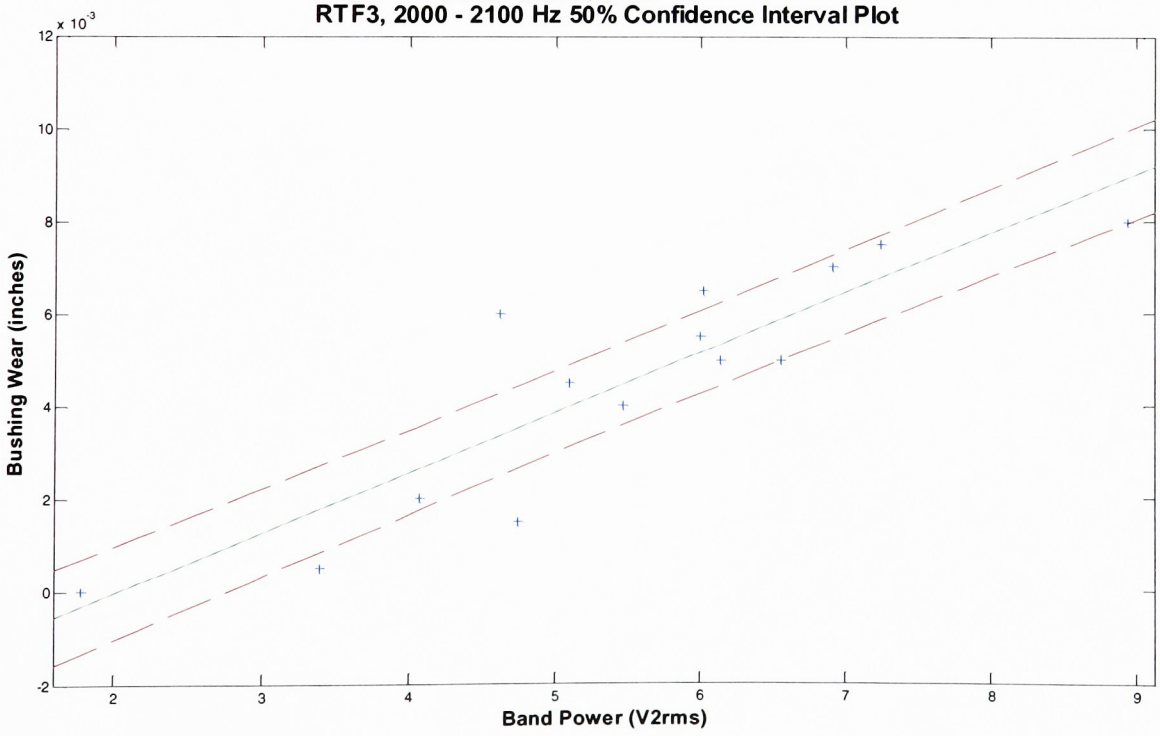
RTF3, 2000 - 2100 Hz 50% Confidence Interval Plot
x 10^-3
Bushing Wear (inches)
Band Power (V2rms)
12
10
8
6
4
2
0
-2
2
3
4
5
6
7
8
9

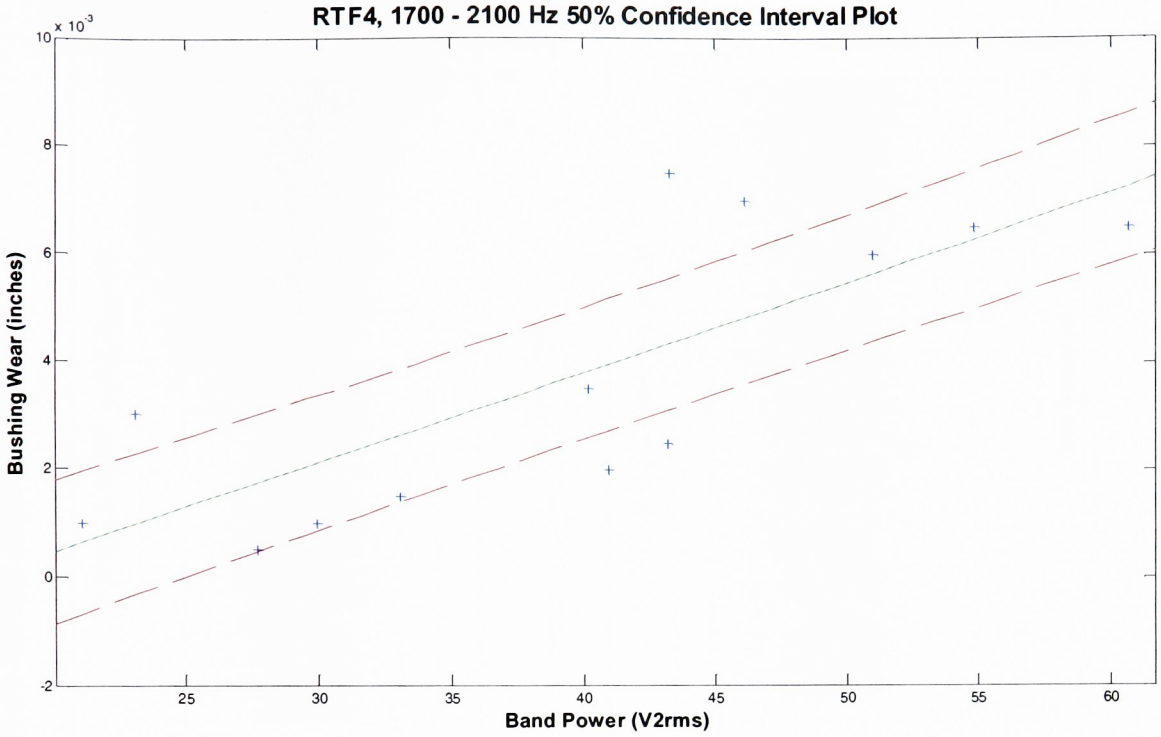
RTF4, 1700 - 2100 Hz 50% Confidence Interval Plot
x 10^-3
Bushing Wear (inches)
Band Power (V2rms)
10
8
6
4
2
0
-2
25
30
35
40
45
50
55
60

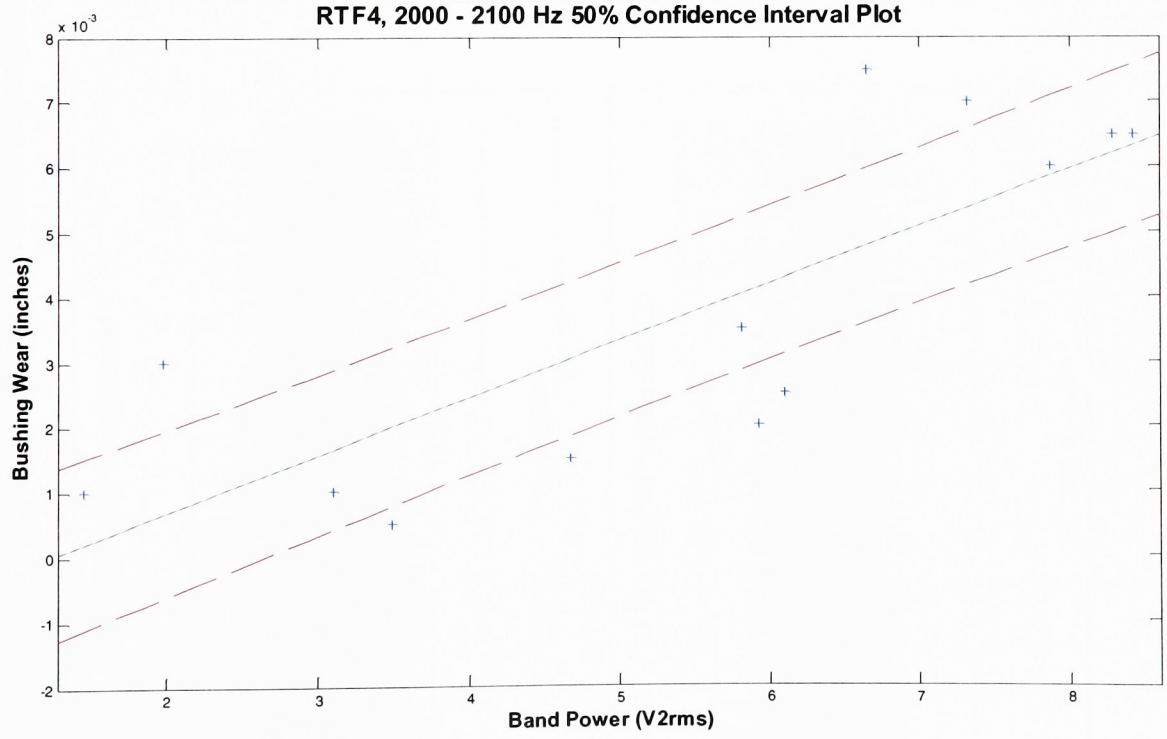
RTF4, 2000 - 2100 Hz 50% Confidence Interval Plot
x 10^-3
Bushing Wear (inches)
Band Power (V2rms)
8
7
6
5
4
3
2
1
0
-1
-2
2
3
4
5
6
7
8

Appendix N: RTF2 Representative Time-domain Plots

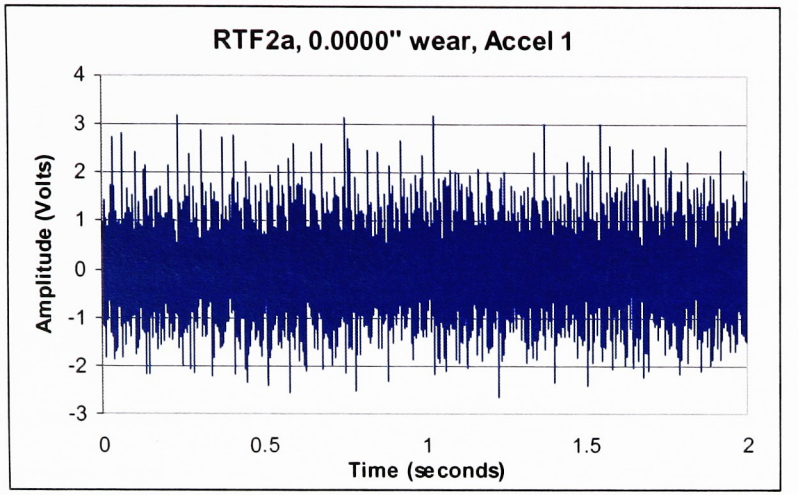

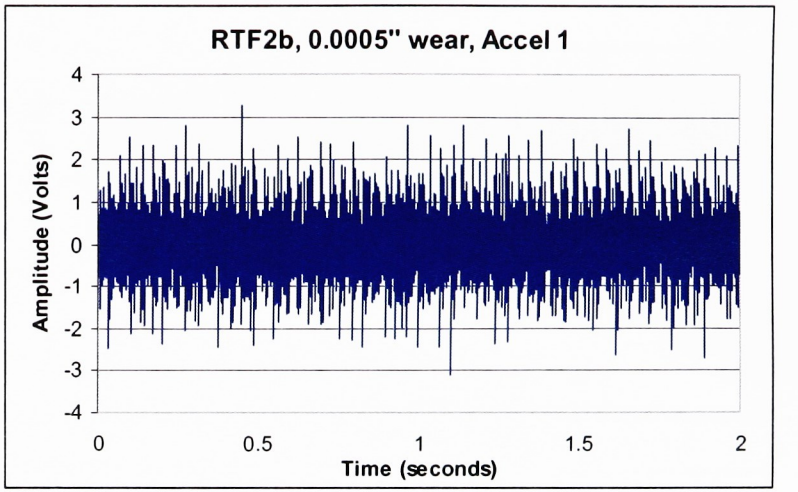

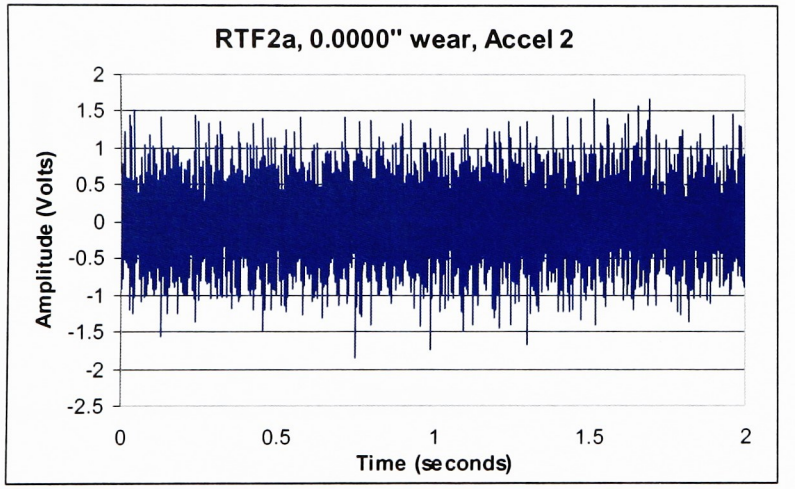

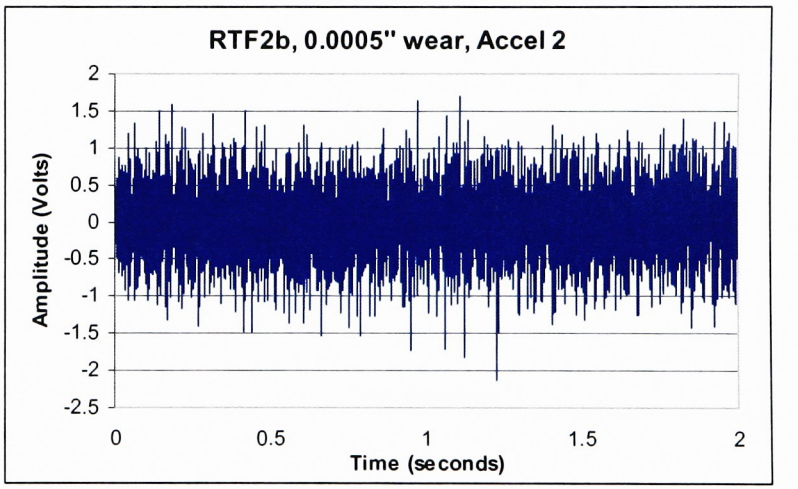

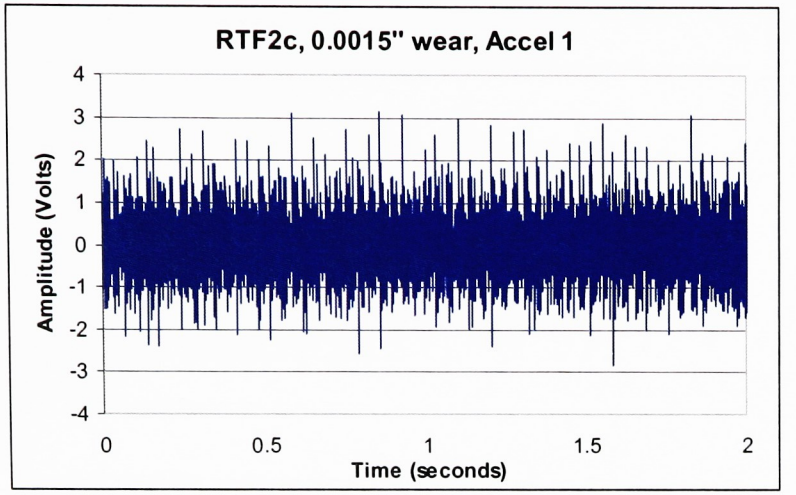
RTF2c, 0.0015" wear, Accel 1
Amplitude (Volts)
4
3
2
1
0
-1
-2
-3
-4
0
0.5
1
1.5
2
Time (seconds)

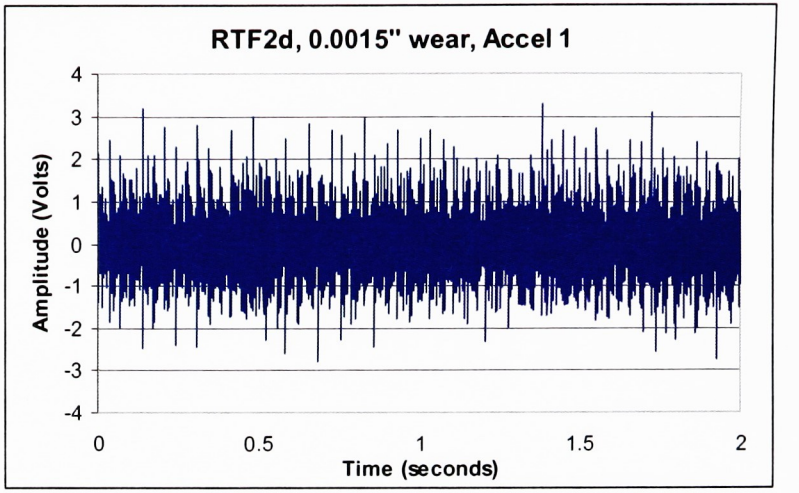
RTF2d, 0.0015" wear, Accel 1
Amplitude (Volts)
4
3
2
1
0
-1
-2
-3
-4
0
0.5
1
1.5
2
Time (seconds)

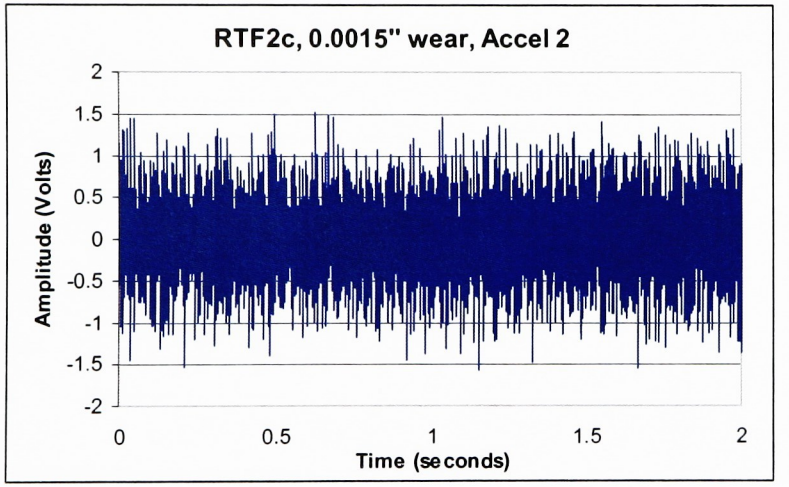
RTF2c, 0.0015" wear, Accel 2
Amplitude (Volts)
2
1.5
1
0.5
0
-0.5
-1
-1.5
-2
0
0.5
1
1.5
2
Time (seconds)

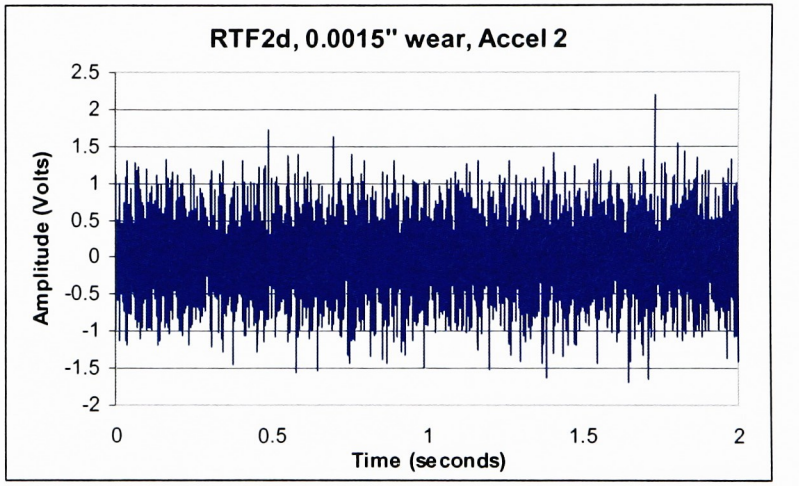
RTF2d, 0.0015" wear, Accel 2
Amplitude (Volts)
2.5
2
1.5
1
0.5
0
-0.5
-1
-1.5
-2
0
0.5
1
1.5
2
Time (seconds)

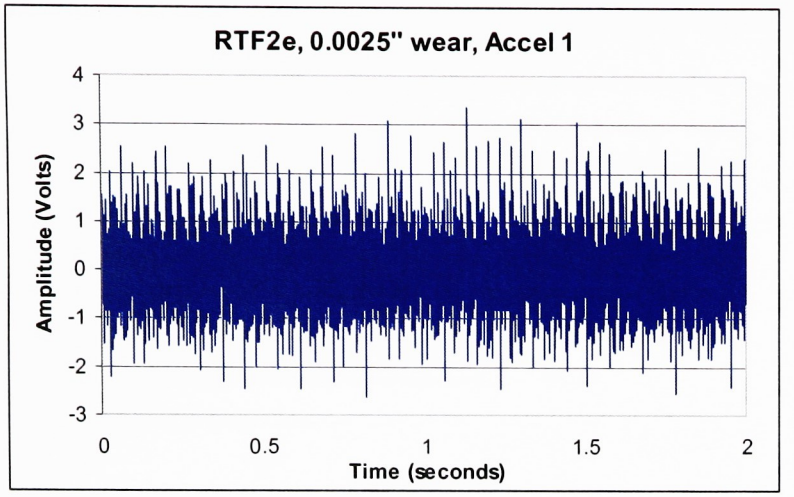
RTF2e, 0.0025" wear, Accel 1
Amplitude (Volts)
4
3
2
1
0
-1
-2
-3
0
0.5
1
1.5
2
Time (seconds)

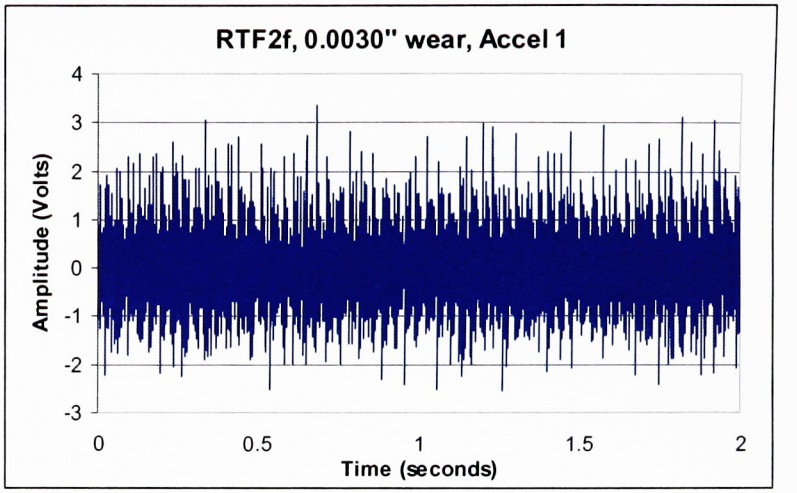
RTF2f, 0.0030" wear, Accel 1
Amplitude (Volts)
4
3
2
1
0
-1
-2
-3
0
0.5
1
1.5
2
Time (seconds)

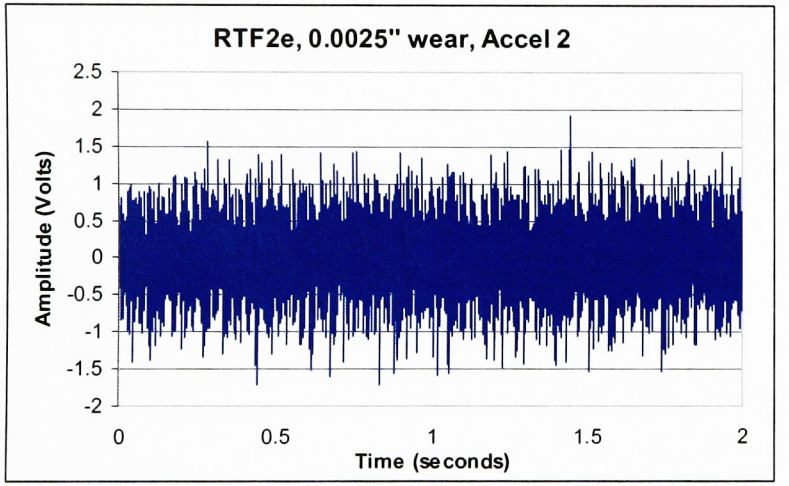
RTF2e, 0.0025" wear, Accel 2
Amplitude (Volts)
2.5
2
1.5
1
0.5
0
-0.5
-1
-1.5
-2
0
0.5
1
1.5
2
Time (seconds)

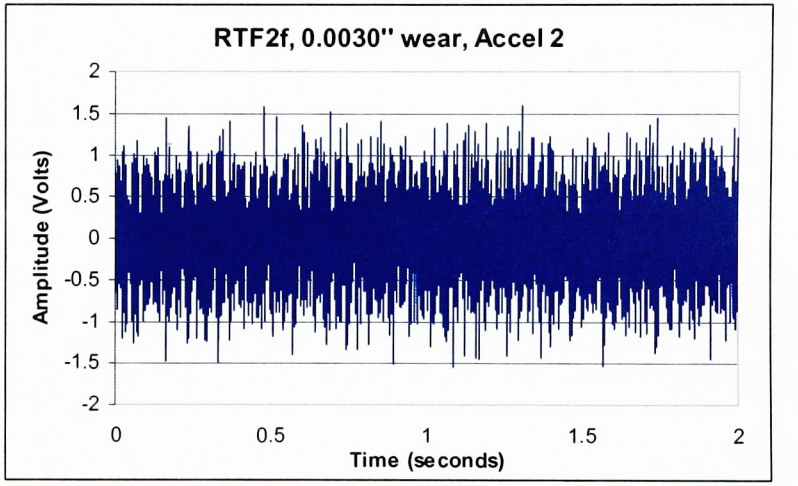
RTF2f, 0.0030" wear, Accel 2
Amplitude (Volts)
2
1.5
1
0.5
0
-0.5
-1
-1.5
-2
0
0.5
1
1.5
2
Time (seconds)

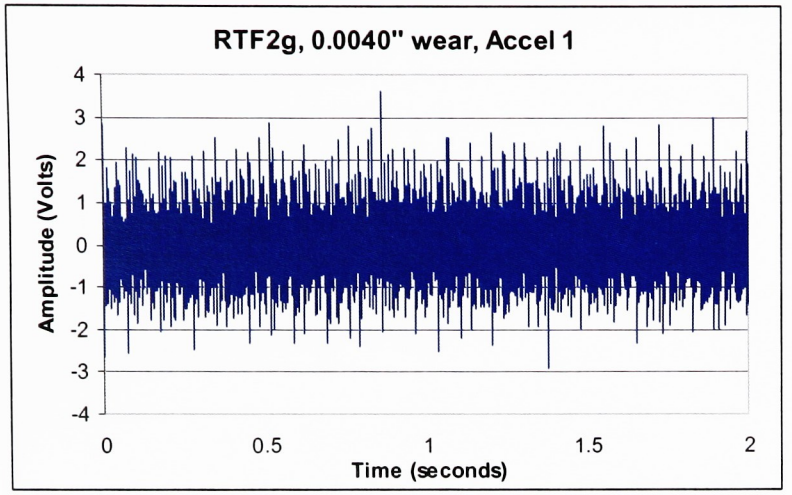
RTF2g, 0.0040" wear, Accel 1
Amplitude (Volts)
4
3
2
1
0
-1
-2
-3
-4
0
0.5
1
1.5
2
Time (seconds)

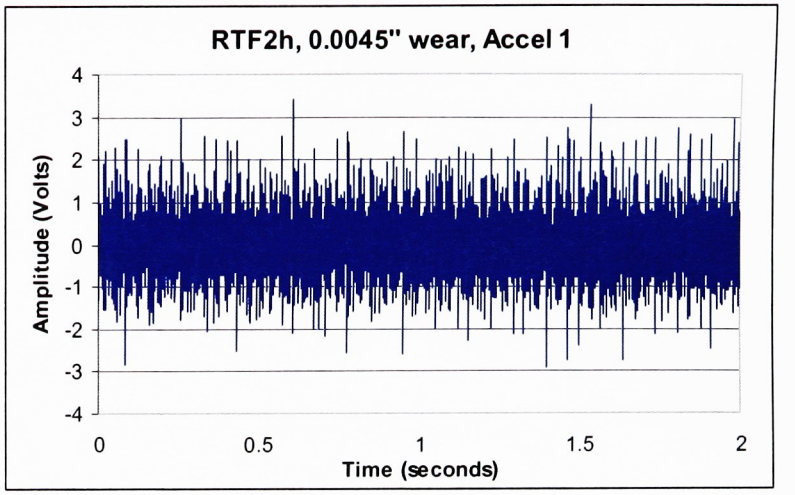
RTF2h, 0.0045" wear, Accel 1
Amplitude (Volts)
4
3
2
1
0
-1
-2
-3
-4
0
0.5
1
1.5
2
Time (seconds)

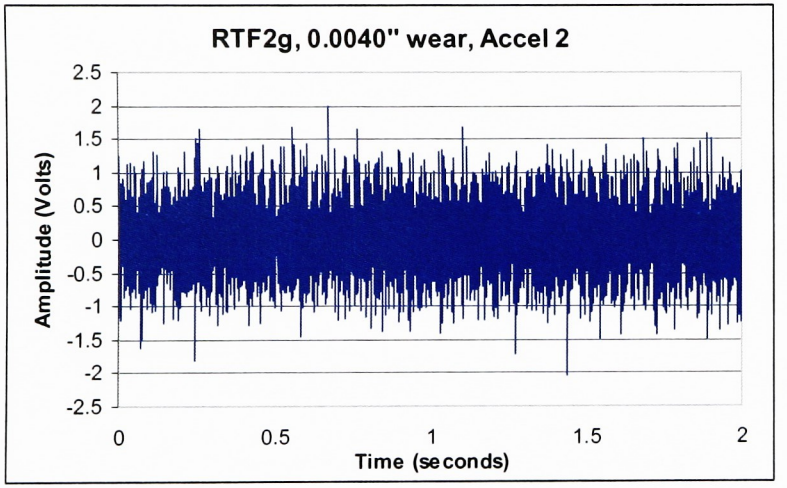
RTF2g, 0.0040" wear, Accel 2
Amplitude (Volts)
2.5
2
1.5
1
0.5
0
-0.5
-1
-1.5
-2
-2.5
0
0.5
1
1.5
2
Time (seconds)

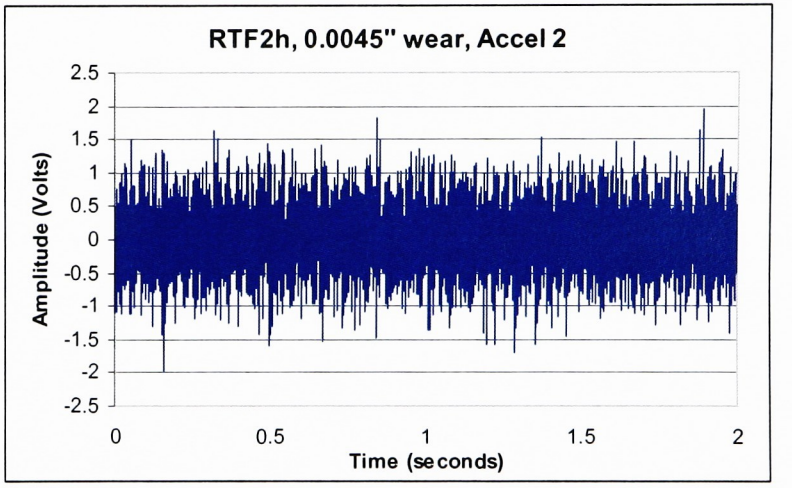
RTF2h, 0.0045" wear, Accel 2
Amplitude (Volts)
2.5
2
1.5
1
0.5
0
-0.5
-1
-1.5
-2
-2.5
0
0.5
1
1.5
2
Time (seconds)

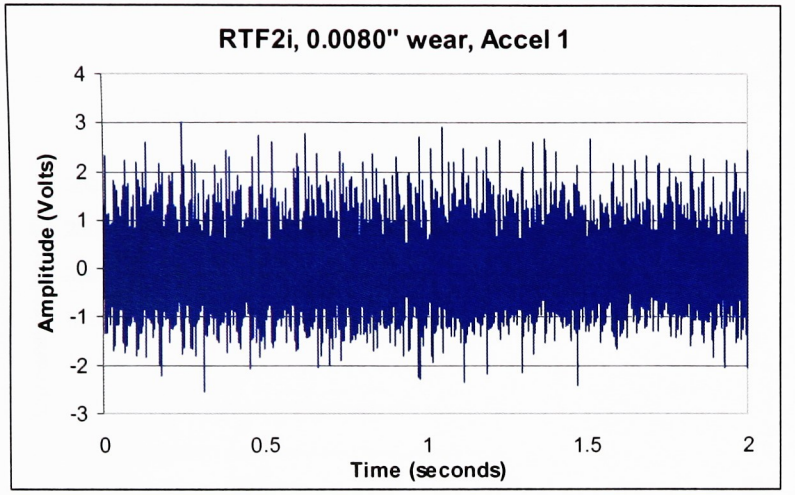
RTF2i, 0.0080" wear, Accel 1
Amplitude (Volts)
4
3
2
1
0
-1
-2
-3
0
0.5
1
1.5
2
Time (seconds)

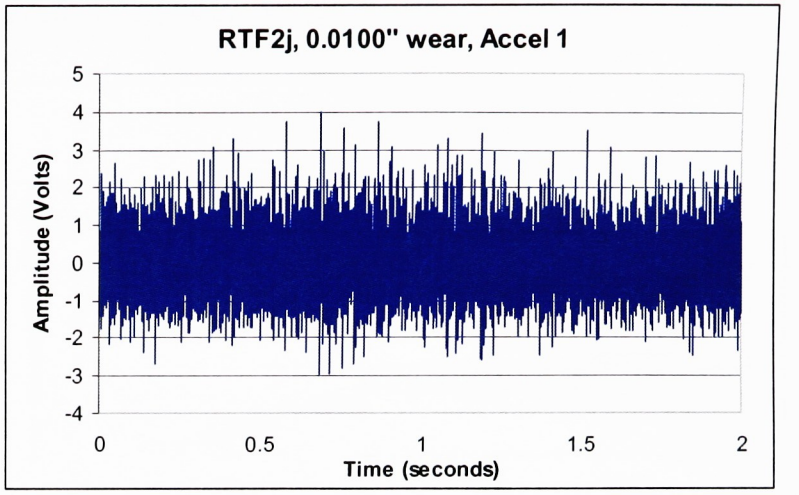
RTF2j, 0.0100" wear, Accel 1
Amplitude (Volts)
5
4
3
2
1
0
-1
-2
-3
-4
0
0.5
1
1.5
2
Time (seconds)

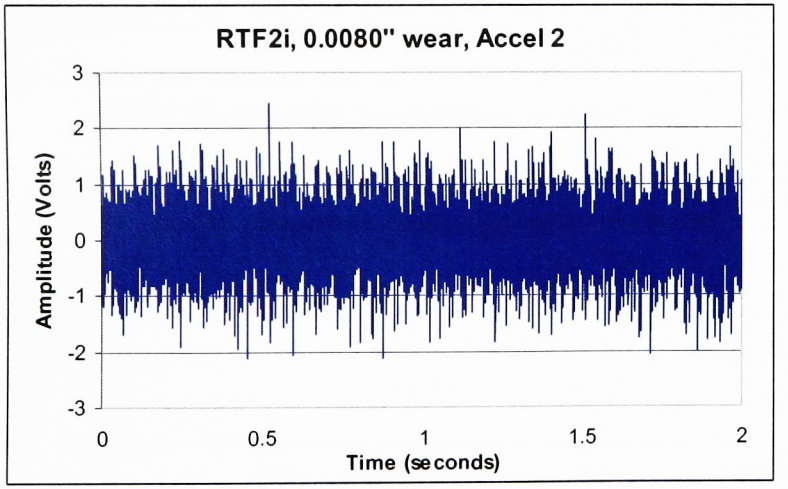
RTF2i, 0.0080" wear, Accel 2
Amplitude (Volts)
3
2
1
0
-1
-2
-3
0
0.5
1
1.5
2
Time (seconds)

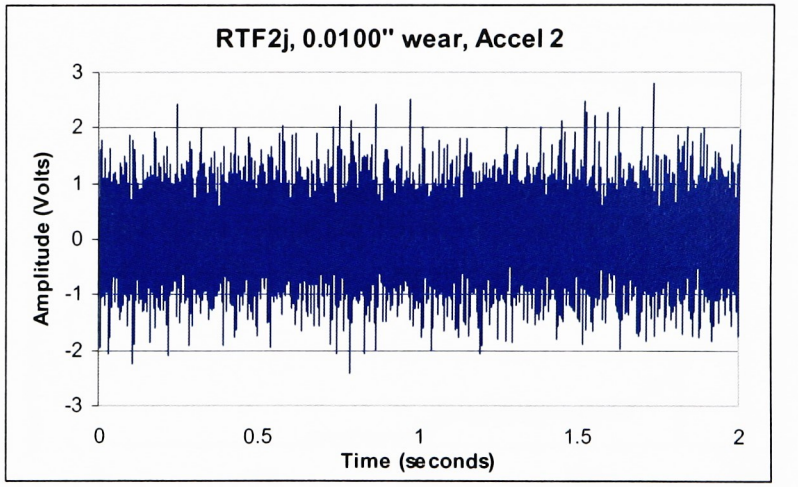
RTF2j, 0.0100" wear, Accel 2
Amplitude (Volts)
3
2
1
0
-1
-2
-3
0
0.5
1
1.5
2
Time (seconds)

Appendix O: RTF Test Temperature and Wear Plots

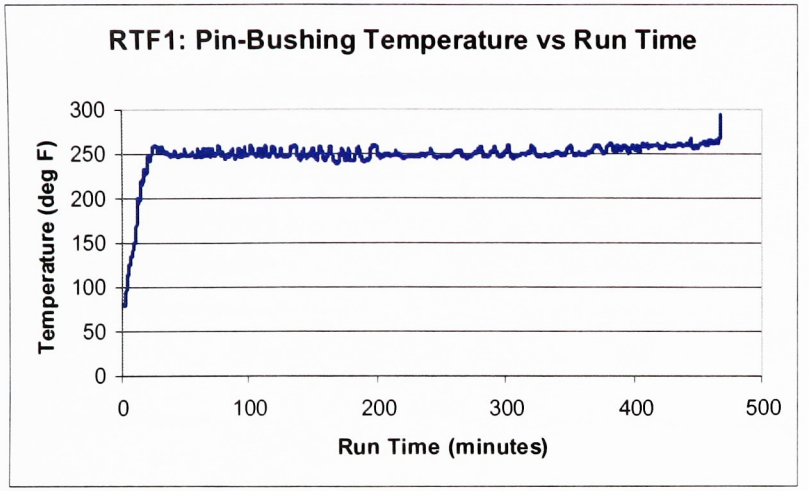

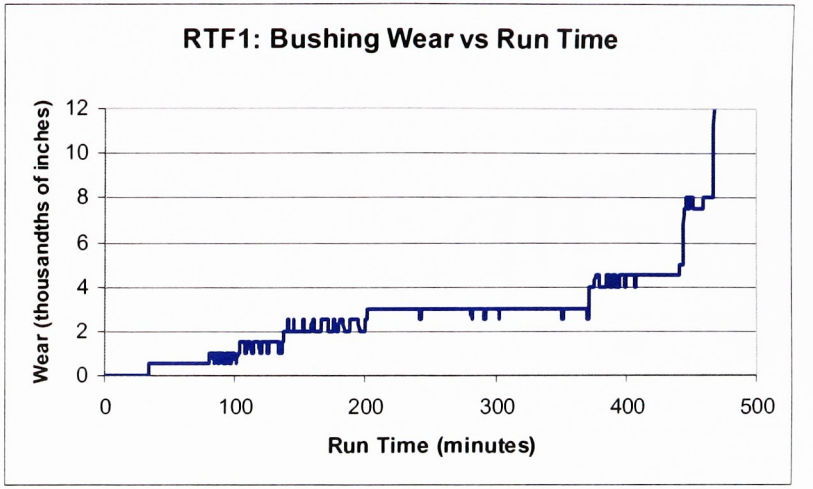

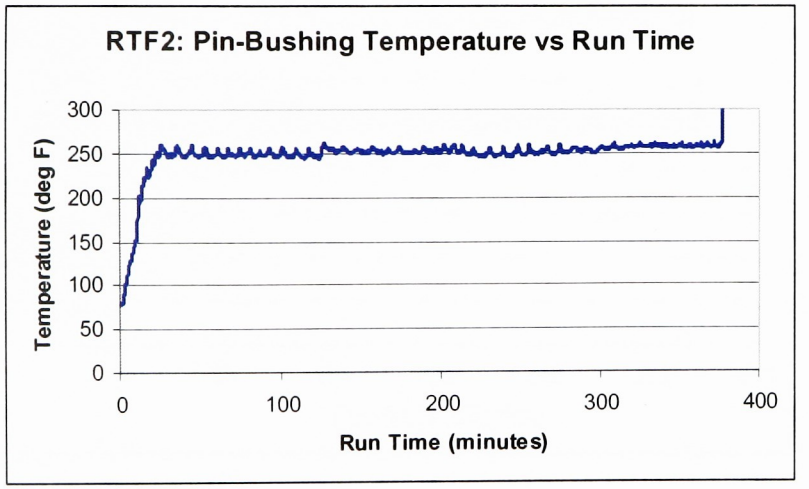

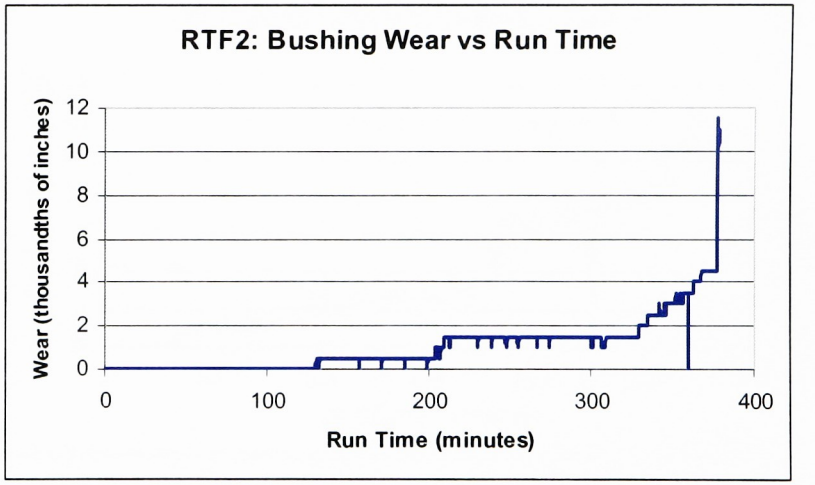

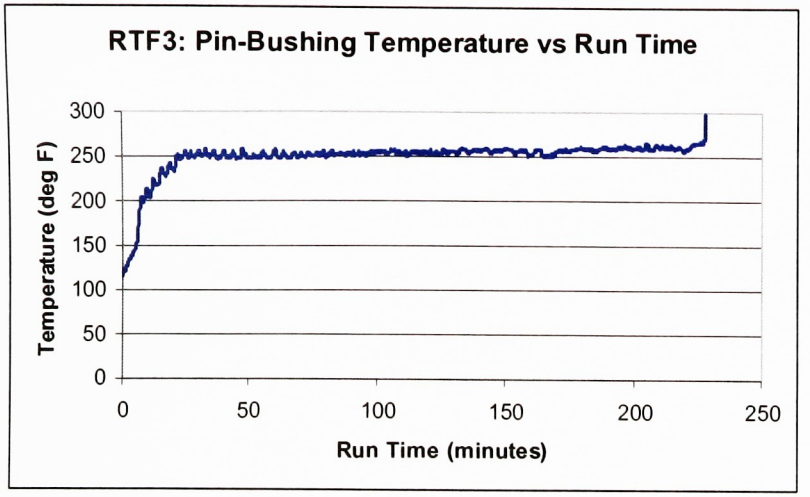
RTF3: Pin-Bushing Temperature vs Run Time
Temperature (deg F)
300
250
200
150
100
50
0
0
50
100
150
200
250
Run Time (minutes)

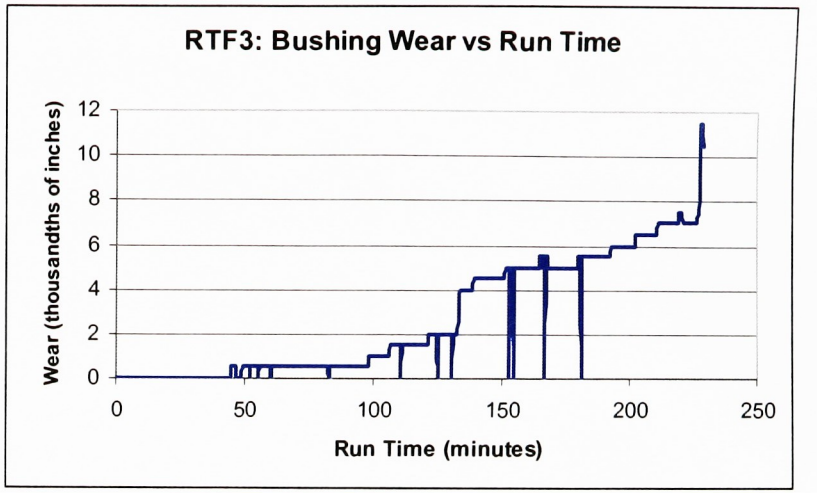
RTF3: Bushing Wear vs Run Time
Wear (thousandths of inches)
12
10
8
6
4
2
0
0
50
100
150
200
250
Run Time (minutes)

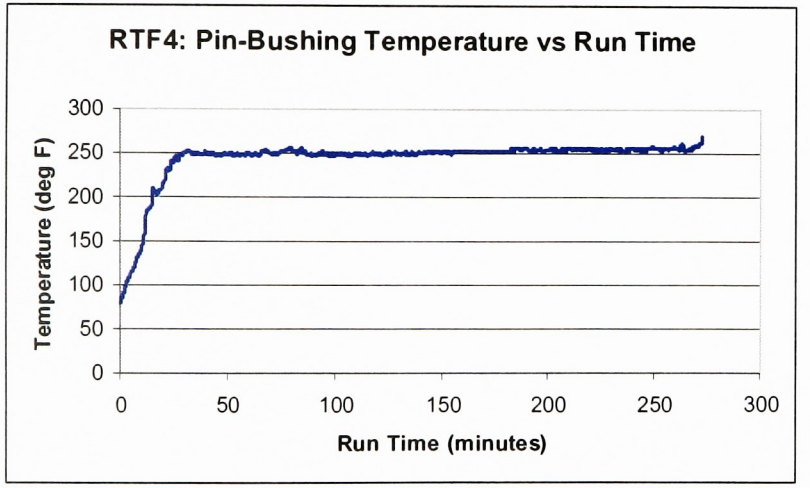
RTF4: Pin-Bushing Temperature vs Run Time
Temperature (deg F)
300
250
200
150
100
50
0
0
50
100
150
200
250
300
Run Time (minutes)

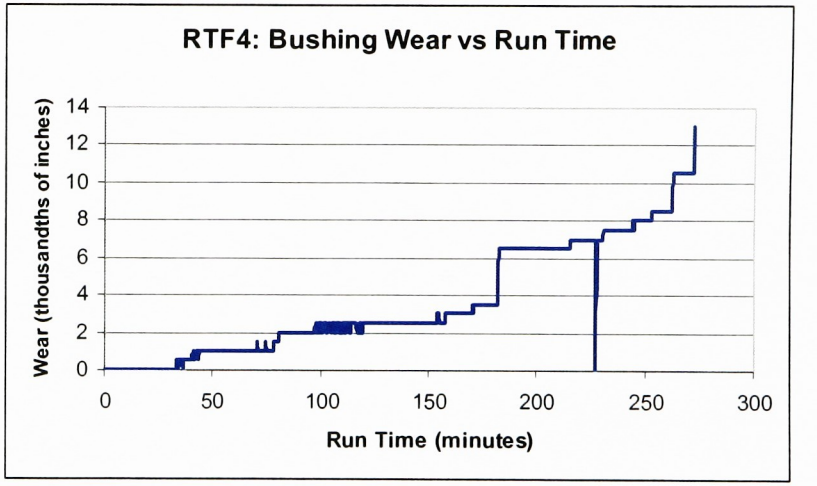
RTF4: Bushing Wear vs Run Time
Wear (thousandths of inches)
14
12
10
8
6
4
2
0
0
50
100
150
200
250
300
Run Time (minutes)